Diss. ETH No. 12669

Electron Paramagnetic Resonance Study of the Copper(II) Complexation with Carbonate Ligands in Aqueous Solution and at Calcium Carbonate Surfaces

DISSERTATION

submitted to the

SWISS FEDERAL INSTITUTE OF TECHNOLOGY ZÜRICH

for the degree of

Doctor of Natural Sciences

presented by

Paul Michel Schosseler

Dipl. Chem. ETH

born April 3, 1969

citizen of Luxembourg

accepted on the recommendation of

Prof. Dr. A. Schweiger, examiner

Prof. Dr. B. Wehrli, co-examiner

1998

Fier meng Elteren

Table of Contents

Table of Contents i

Summary v

Zusammenfassung vii

1. Introduction 1

2. Basic Concepts of CW and Pulse EPR 5

2.1 One Electron in the Magnetic Field 5

2.1.1 Electron Zeeman Interaction 5

2.1.2 Crystal-Field Splitting and Spin-Orbit Coupling 7

2.1.3 **g** Anisotropy 9

2.2 Interaction with Nuclear Spins 12

2.2.1 Hyperfine Interaction 13

2.2.2 The $S = 1/2$, $I = 1/2$ system 15

2.2.3 Weak and Strong Coupling 18

2.2.4 Matching Range and Exact Cancellation 22

2.2.5 Combination Lines in ESEEM Experiments 23

2.3 The Complete Spin Hamiltonian 25

2.3.1 Zero-Field Splitting 25

2.3.2 Nuclear Quadrupole Interaction 25

2.3.3 Summary of Energy Terms 26

2.4 EPR of Cu^{2+} Complexes 27

3. Methodology of EPR 31

3.1 CW and Pulse EPR 31

3.2 MW Pulses and Spin Dynamics 34

3.3 Relaxation Times and Linewidths 35
3.4 Pulse EPR Experiments 37
3.4.1 Two-Pulse ESEEM 37
3.4.2 Three-Pulse ESEEM 39
3.4.3 1D Four-Pulse ESEEM 40
3.4.4 HYSCORE 41
3.4.5 ENDOR 44

4. Aqueous Chemistry of Cu^{2+} and Carbonates **47**

4.1 Cu^{2+} and Carbon Dioxide 48
4.1.1 Coordination Chemistry of Cu^{2+} 48
4.1.2 Carbon Dioxide 49
4.1.3 Complexation of Cu^{2+} by Carbonate Ligands 49
4.2 The Solid Calcium Carbonates 50
4.2.1 Structural Characteristics 50
4.2.2 Crystal Growth and Dissolution 52
4.2.3 Interactions with Trace Metal Ions 54
4.3 Chemical Equilibrium Calculations 56
4.3.1 ChemEQL 56
4.3.2 Surface Complexation Model 57
4.3.3 The CO_2/H_2O system 58
4.3.4 The Cu^{2+}/H_2O system 59
4.3.5 The $Cu^{2+}/CO_2/H_2O$ system 60
4.3.6 The $CaCO_3(s)/Cu^{2+}/H_2O$ system 61

5. Copper Carbonate Complexes in Aqueous Solution. **69**

5.1 Introduction 69
5.2 Experimental Section 70
5.2.1 Sample Preparation 70
5.2.2 Glass Forming Additives 71
5.2.3 Equipment 72
5.2.4 Data Manipulation 73
5.2.5 EPR and ESEEM Simulations 74
5.3 Results 75
5.3.1 Optical Spectra 75
5.3.2 EPR Spectra 76
5.3.3 ESEEM and ENDOR of ^{13}C 79
5.3.4 1D and 2D ESEEM of Protons 84
5.4 Discussion 91

5.4.1 Optical Spectra 91
5.4.2 EPR Spectra 92
5.4.3 ESEEM and ENDOR of ^{13}C 93
5.4.4 1D and 2D ESEEM of Protons 95
5.4.5 Structure Proposals 97
5.4.6 Freezing Effects 98
5.5 Conclusions 100

6. Interactions of Cu^{2+} with Solid Calcium Carbonates **101**

6.1 Introduction 101
6.2 Experimental Section 102
6.2.1 Sample Preparation 102
6.2.2 Equipment 105
6.2.3 Data Manipulation 105
6.2.4 EPR and HYSCORE Simulations 106
6.3 Results 106
6.3.1 AAS Measurements 106
6.3.2 EPR Spectra 106
6.3.3 Two-Pulse ESEEM 113
6.3.4 HYSCORE of ^{13}C 116
6.3.5 1D Four-Pulse ESEEM of Protons 123
6.4 Discussion 123
6.4.1 AAS Measurements 123
6.4.2 Structural Assignment of the Observed Copper Species 124
6.4.3 Mechanistic Interpretation 130
6.4.4 Summary of the Experimental Results 133
6.4.5 Application to other Metal Ions 136
6.5 Conclusions 139

APPENDIX A **141**

A.1 Spin Hamiltonian 141
A.2 Density Operator Formalism 142
A.3 Calculation of CW and Pulse EPR Spectra 143

APPENDIX B **145**

B.1 Two-Pulse ESEEM Formula 145
B.2 Three-Pulse ESEEM Formula 146
B.3 Four-Pulse ESEEM Formula 146

APPENDIX C **149**

C.1 Equilibrium Constants 149

C.2 EXCEL Input Matrices for ChemEQL. 152

References **155**

Symbols and Abbreviations **163**

Acknowledgement **167**

Curriculum Vitae **169**

Summary

The interactions between trace metal ions and the widespread calcium carbonate minerals are of interest both for environmental chemists and geologists. The complexation with carbonate and bicarbonate ions in solution plays a central role in trace metal speciation in many aquatic environments. Furthermore adsorption at calcium carbonate surfaces and coprecipitation reactions influence the distribution of the ions as well as the reactivity of the minerals.

In this thesis continuous wave (CW) and pulse Electron Paramagnetic Resonance (EPR) techniques are applied to investigate the complexation of the transition metal ion Cu^{2+} with carbonate ligands in aqueous solution and at the surface of the two $CaCO_3$ modifications, vaterite and calcite. From the detailed structural and electronic information obtained for the copper-carbonate complexes general conclusions about the surface structure of $CaCO_3$ minerals and adsorption and coprecipitation reactions of other trace metal ions are derived.

The first part deals with the pH dependent complexation between Cu^{2+} and ^{13}C-labeled carbonate ligands in aqueous solution. Changes in the coordination geometry of the copper complexes are followed through the interactions of the unpaired Cu^{2+} electron with the ligand field and nuclei of ^{13}C-labeled carbonate ligands and protons from water or hydroxyl ligands in the first and second coordination spheres of the cation. The small ^{13}C hyperfine coupling observed in the pulse EPR spectra in frozen solution and at pH 5.5 is assigned to weak, monodentate coordination of carbonates to the Cu^{2+}

ion. The large ^{13}C hyperfine coupling found at pH 6.5 and 8 arises from bidentate coordination of carbonate ligands and is explained by a higher covalency of the π bonding in the four-membered ring. The carbonate complexation in the equatorial plane of the copper complex leads to an elongation of the axial water bonds. The observation of both mono- and bidentate coordination at pH 6.5 and 8 by pulse EPR in frozen solution is in contradiction to the calculated concentrations of copper-carbonate complexes at room temperature. Although equilibrium shifts during the freezing of the samples can not be excluded, the basic mechanisms of mono- and bidentate complexation observed in frozen solution are expected to apply also in aqueous solution at ambient temperature.

The investigation of the Cu^{2+} uptake by vaterite and calcite in the pH range 8.5 to 9 in the second part of the thesis gives insight on a molecular level into complexation reactions at the mineral surfaces. The structural assignment is based on the EPR parameters and ^{13}C and proton hyperfine couplings observed for the copper-carbonate complexes in solution. Atomic absorption spectroscopy (AAS) and pulse EPR results show that the adsorption of the Cu^{2+} ions on the mineral surface, nearly complete within a few minutes, is followed by rapid dehydration. The strong surface binding is due to monodentate coordination to three or four carbonate surface ions, comparable to a chelate complexation in solution. The formation of square-planar or square-pyramidal copper complexes at exposed surface sites like kinks and steps, revealed by CW EPR, can explain the inhibition of calcium carbonate crystal growth and dissolution. Upon recrystallization the Cu^{2+} ions are integrated into the calcite lattice where they exhibit a dynamic Jahn-Teller effect. The resulting local lattice distortions are expected to destabilize the $Cu_xCa_{(1-x)}CO_3(s)$ solid solution. The results support the concept of a dynamic calcium carbonate surface, covered by a thin, structured surface layer. The detailed structural information obtained for Cu^{2+} provides a better understanding of the interaction of other metal ions like Fe^{2+}, Co^{2+}, Ni^{2+} and Zn^{2+} with calcium carbonate minerals.

Zusammenfassung

Die Wechselwirkungen zwischen Spurenmetallen und Calciumcarbonatmineralien ist von großem Interesse für Umweltchemiker und Geologen. Die Komplexbildung mit Carbonat- und Bicarbonationen in Lösung bestimmt oft die Speziierung von Spurenmetallen in natürlichen Gewässern. Adsorption an Calciumcarbonatoberflächen und Fällungsreaktionen beeinflussen sowohl die Verteilung der Metallionen als auch die Reaktivität der Mineralien.

Gegenstand der vorliegenden Arbeit ist die Untersuchung der Komplexbildung des Übergangsmetallions Cu^{2+} mit Carbonatliganden in wässeriger Lösung und an den Oberflächen der beiden $CaCO_3$ Modifikationen Vaterit und Calcit mittels 'Continuous Wave' (CW) und gepulster Elektron Paramagnetischer Resonanz (EPR). Aus den geometrischen und elektronischen Strukturen der Kupfercarbonatkomplexe können allgemeine Schlußfolgerungen bezüglich der Oberflächenbeschaffenheit von $CaCO_3$ Mineralien und der Adsorptions- und Fällungsreaktionen anderer Spurenmetalle abgeleitet werden.

In einer ersten Studie wird die pH-abhängige Komplexbildung zwischen Cu^{2+} und ^{13}C markierten Carbonatliganden in Lösung untersucht. Die Wechselwirkung zwischen dem ungepaarten Elektron des Kupferions mit dem Ligandenfeld sowie ^{13}C-Kernen von markierten Carbonatliganden und Protonen von Wasser- oder Hydroxylliganden in der ersten und zweiten Koordinationssphäre des Kations geben Aufschluß über Änderungen in der Koordinationsgeometrie. Die kleine ^{13}C-Hyperfeinkopplung, welche in den Puls-EPR Spektren bei tiefer Temperatur und pH 5.5 beobachtet wird, kann einer einzähnigen

Koordination zwischen Kupferion und Carbonat zugeordnet werden. Die große ^{13}C-Hyperfeinkopplung bei pH 6.5 und 8 weist auf eine zweizähnige Carbonatkoordination hinweist und kann durch die höhere Kovalenz der π-Bindung im Viererring erklärt werden. Die Carbonatkoordination in der equatorialen Komplexebene führt zu einer Streckung der axialen Wasserbindung. Die gleichzeitige Beobachtung von ein- und zweizähniger Bindung bei den höheren pH-Werten 6.5 und 8 in gefrorener Lösung steht im Widerspruch zu der berechneten pH-abhängigen Verteilungen der Kupfercarbonatkomplexe. Obwohl Gleichgewichtsverschiebungen beim Einfrieren der Proben nicht ausgeschlossen werden können, kann man doch annehmen, dass die grundsätzlichen Bindungsmechanismen auch für ein-und zweizähnige Komplexbildung in wässeriger Lösung bei Raumtemperatur gelten.

Die Untersuchung der Kupferaufnahme durch Vaterit und Calcit im pH-Bereich 8.5 bis 9 in einer zweiten Studie gibt auf molekularer Ebene Einblick in Komplexbildungsreaktionen an den Mineraloberflächen. Die Strukturzuordnung erfolgt aufgrund der EPR Parameter und ^{13}C-und Protonenkopplungskonstanten der Kupfercarbonatkomplexe in Lösung. Atomabsorptionspektroskopie (AAS) und Puls-EPR zeigen, dass die Kupferionen nach der innerhalb weniger Minuten praktisch vollständigen Adsorption an der Mineraloberfläche rasch dehydratisiert werden. Die einzähnige Komplexbildung durch drei bis vier Oberflächencarbonationen, vergleichbar mit einer Chelatbindung in Lösung, ist verantwortlich für die starke Oberflächenbindung. Der Nachweis von quadratisch-planaren und quadratisch-pyramidalen Kupferkomplexen an Oberflächendefekten wie Treppenabsätzen oder Ecken von Treppenabsätzen mittels CW EPR erklärt die Hemmung von Calziumcarbonatkristallwachstums und -auflösung. Die bei der Umkristallisation ins Kristallgitter eingebauten Cu^{2+} Ionen zeigen einen dynamischen Jahn-Tellereffekt. Die lokalen Verzerrungen führen zu einer Destabilisierung der $Cu_xCa_{(1-x)}CO_3(s)$ Mischphase. Diese Resultate unterstützen das Konzept einer dynamischen, mit einer dünnen, strukturierten Oberflächenschicht bedeckten $CaCO_3$ Oberfläche. Die für Cu^{2+} erhaltenen Strukturinformationen vertiefen das Verständnis der Wechselwirkung anderer Metallionen wie Fe^{2+}, Co^{2+}, Ni^{2+} und Zn^{2+} mit $CaCO_3$ Mineralien.

CHAPTER 1 *Introduction*

Chemical processes at the surfaces of minerals, organic particles and biological organisms are of outmost importance in atmospheric and aquatic chemistry. The solid-water interfaces act as catalysts for redox reactions and promote photochemical reactions leading e.g. to the degradation of toxic organic substances. The dissolution and precipitation of inorganic material regulates the basic inorganic composition of natural waters. The complexation with organic and inorganic ligands in solution and at solid surfaces and the formation of surface precipitates considerably influence the distribution of trace metals in the aquatic environment [1,2].

Carbonates are among the most reactive minerals found at the earth's surface [3]. The dissolution of calcite and dolomite represents about 50% of the chemical denudation of the continents. The hydrosphere links the carbonate minerals with the atmospheric reservoir of CO_2. As a result Ca^{2+}, Mg^{2+} and HCO_3^- are the most abundant ions present in natural waters with typical concentrations in the millimolar range. In many aquatic systems trace metal speciation is controlled by carbonate and bicarbonate ions. The precipitation of carbonate minerals in lakes and oceans, on the other hand, provides important pathways of trace metal scavenging by adsorption of metal ions at the mineral surface or coprecipitation during crystal growth of calcite, aragonite and other carbonate minerals. These processes are not only important for the bio-availability of toxic metals such as

copper and cadmium. They can also be used to extract information on chemical changes in aquatic systems by the analysis of sedimentary records [4].

A better understanding of the interactions between metal ions such as Mn^{2+}, Fe^{2+}, Cu^{2+} and Cd^{2+} and carbonate ligands in aqueous solution and at carbonate mineral surfaces has therefore been the motivation for a large number of thermodynamic and spectroscopic studies (see e.g. [5-10] and references therein) and is also the goal of the present investigation. From the chemical point of view, more knowledge about the complexation in solution and the adsorption at surfaces by chemical bonding between solute and surface functional groups, requires characterization of the geometrical and electronic structures of the metal complexes.

Published complex stochiometries and stability constants for carbonate complexes are mainly based on titration and solubility experiments and often lead to contradictory interpretation of the molecular structures [5,9]. More detailed information about chemical bonding and structures is obtained from spectroscopic investigations. A convenient tool for the investigation of electronic configurations of metal complexes in solution is UV/Vis spectroscopy [11]. With IR and Raman spectroscopies, the methods most commonly adopted for the characterization of carbonate species, mono- and bidentate coordination of carbonate ligands can be distinguished [12,13]. The number of spectroscopic techniques that allow for a characterization of surface structures under environmental conditions on a molecular scale is restricted [14]. With atomic force microscopy (AFM) calcite surfaces have been imaged down to microtopographic and molecular scales [15]. A description of chemical structures and bonding at calcite surfaces can be obtained by X-ray photoelectron spectroscopy (XPS) and low energy electron diffraction (LEED) [16,17].

Although these techniques have given deep insight into calcite surface processes they do not allow for the investigation of chemical bonding at individual absorption sites. Detailed information about the geometrical and electronic structures of the metal complexes in solution and at surfaces can be obtained from electron paramagnetic resonance (EPR) [18-20]. EPR is a powerful spectroscopic tool for the investigation of chemical species with unpaired electrons like radicals or transition metal (TM) ions with partially filled *d*-orbitals. The non-destructive technique allows the in-situ study of structures and

dynamics of such species involved in numerous chemical and biochemical reactions. The applications of EPR are thus very diverse and range from chemistry and physics over material sciences and geology to biology and medicine.

In our approach we use the interactions of the electron spin of the Cu^{2+} ion with its coordinative environment to obtain structural and electronic information about the complexation of carbonate ions in solution and at the vaterite and calcite surfaces. With continuous wave (CW) and pulse EPR methods the ligand exchange reactions in the first and second coordination spheres of the metal ion are followed in solution and during the interaction with the solid carbonates. From the point of view of EPR copper complexes are well suited for this investigation since the $3d^9$ ion is subject to a Jahn-Teller distortion, so that axial and equatorial coordination sites become easily distinguishable [21]. In the aquatic environment copper is highly toxic for algae and plants even in small concentrations [1]. Mechanism like the complexation with organic material or at algae and mineral surfaces which keep the concentration of the free Cu^{2+} ion low are very important and should be well understood [22,23]. The carbonate chemistry of the metal ion, on the other hand, is rather complex and the investigation of its interaction with the highly reactive carbonate surfaces challenging [24]. It is also important to note that both the reactivity and structure of the carbonate surfaces can be influenced by adsorption and coprecipitation of metal ions. The copper ion, e.g., is known to inhibit the calcium carbonate dissolution and precipitation. Knowledge about the copper complexes at the carbonate surface is expected to give new insights into the mechanisms of inhibition.

After the general introduction given in this chapter the theory and methodology of CW and pulse EPR are explained in more detail in chapters 2 and 3. The description is given for a reader who is not familiar with magnetic resonance spectroscopies. The different topics are illustrated with examples closely related to the copper-carbonate system so that the discussion of the experimental results in chapters 5 and 6 can be followed. The fundamental quantum-mechanical concepts underlying the more phenomenological description of EPR theory in chapter 2 are summarized in Appendix A. In chapter 3 experimental aspects of CW and pulse EPR spectroscopy are presented and the different pulse EPR schemes used in this study are described. The analytical formulae of the two-, three- and four-pulse electron spin echo envelope modulation (ESEEM) experiments in

Appendix B give insight into the advantages and limitations of the different pulse sequences.

Chapter 4 summarizes the important aspects of copper and carbonate chemistry on which the interpretation of the spectroscopic data is based. The structures of the calcium carbonate minerals vaterite and calcite are discussed. Current theories about the mineral-surface reactivities are presented with a focus on the interaction with trace metal ions. The second part of chapter 4 is dedicated to the speciation calculations for copper and carbonate ions in solution and at the calcium carbonate surfaces, performed with the program ChemEQL [25] using the complexation constants tabulated in Appendix C. The calculations of the distribution of surface ion complexes is based on the surface complexation model developed by Schindler et al. [26]. The results of the speciation calculations are used for the preparation of the samples investigated in chapters 5 and 6. A comparison of the computed predictions with the experimental results helps to refine surface complexation models as shown in chapter 4.

In chapter 5 and 6, finally, experimental results are presented and discussed. In a first part the pH dependent complexation of Cu^{2+} with ^{13}C-labeled carbonate ions in aqueous solution is investigated by UV/Vis spectroscopy and CW and pulse EPR (chapter 5). The detailed information about the geometrical and electronic structures obtained for the complexes in solutions is the starting point for the study of the interaction of copper with solid calcium carbonates in chapter 6. AAS measurements show that the adsorption of Cu^{2+} to the mineral surface is complete within minutes. The fate of the Cu^{2+} ions at the surface and the integration into the lattice bulk are easily followed by CW EPR spectroscopy as the spectra are very sensitive to the symmetry changes. Ligand substitution in the first coordination sphere of the copper complexes is detected with pulse EPR techniques. From the analysis of the ^{13}C spectra of labeled carbonate ions in solution and at the calcium carbonate surface differences between solution and surface complexes are deduced. Comparison with other TM ions allows for a more general interpretation of the adsorption results and the calcium carbonate surface properties.

CHAPTER 2

Basic Concepts of CW and Pulse EPR

In this chapter the theoretical concepts underlying CW and pulse EPR are outlined and the terminology necessary for the understanding of the topics discussed in the following chapters is introduced [18-20,27]. The magnitude of the interactions between electron and nuclear spins and their environment determines whether the relevant information is obtained by CW or pulse EPR. In addition to the examples in each section the EPR of copper complexes is discussed in more detail at the end of the chapter.

2.1 One Electron in the Magnetic Field

2.1.1 Electron Zeeman Interaction

For the discussion of the principles of EPR we start with the simple case of a two-level system for a paramagnetic centre with an electron spin $S = 1/2$. In the absence of any magnetic field the magnetic moment, associated with the electron spin, is randomly oriented and the two energy levels are degenerate. The application of an external magnetic field $\boldsymbol{B}_0$ results in a splitting of the two energy levels as the electron spin $\boldsymbol{S}$ can only be oriented parallel or anti-parallel to the magnetic field vector. The quantization of the energy levels is due to the quantum-mechanical nature of the electron spin. The potential energy of this system is derived from the classical expression for the energy of a mag-

netic dipole in a magnetic field and is described by the spin Hamilton operator (Appendix A), expressed in frequency units:

$$\mathcal{H} = g_e \frac{\beta_e}{h} \boldsymbol{S} \boldsymbol{B}_0 . \tag{2.1}$$

where g_e= 2.0023, the dimensionless g-value of the free electron, β_e denotes the Bohr Magneton (J·T^{-1}) and h the Planck constant (J·s); B_0 is given in Tesla (T). The energies for the two spin states are then given by the eigenvalues of $\mathcal{H}$ in Eq. (2.1) and characterized by the spin quantum numbers $m_S = \pm 1/2$,

$$E(m_S) = g_e \frac{\beta_e}{h} B_0 m_S . \tag{2.2}$$

The splitting between the two energy states is called *electron Zeeman interaction* (EZI) and is proportional to the magnitude of B_0, as illustrated in Figure 2-1. The energy difference between the two Zeeman states is given by $\Delta E = E(m_S = +1/2) - E(m_S = -1/2) = g_e \frac{\beta_e}{h} B_0$ (in Hz).

The most simple EPR experiment one could imagine involves the application of an electromagnetic radiation field of variable frequency ν to this system. If the energy of the

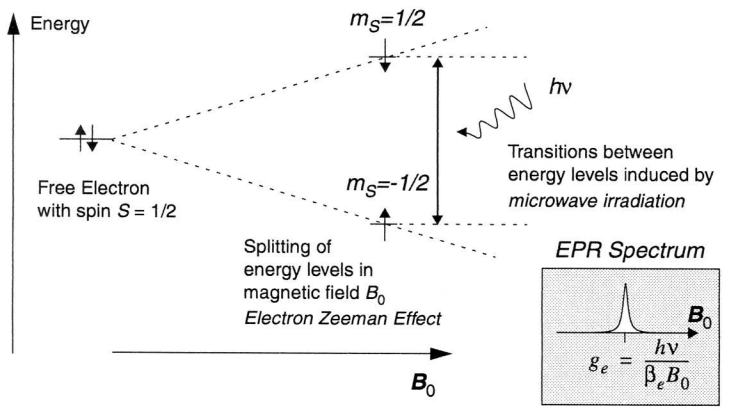

Fig. 2-1 Illustration of the Zeeman splitting for a S = 1/2 system with one unpaired electron in an external magnetic field $\boldsymbol{B}_0$. For a given irradiation frequency ν a transition between the Zeeman states occurs if the resonance condition is fulfilled (see inset).

radiation field matches the energy gap ΔE, transitions between the two spin states can be induced, i.e. the spin can be flipped from one orientation to the other. In this case the resonance condition is fulfilled:

$$\Delta E = \nu = g_e \frac{\beta_e}{h} B_0. \tag{2.3}$$

For experimental reasons, however, the microwave frequency is usually held constant in a CW EPR experiment and the magnetic field is swept linearly (cf. chapter 3). From Eq. (2.3) it follows that B_0 and g_e are inversely proportional.

2.1.2 Crystal-Field Splitting and Spin-Orbit Coupling

Although the case discussed so far is a very simple one, there are a number of paramagnetic centers that can be described by a two-level system with resonances around $g = 2$, e.g. free radicals in solution or TM ions such as Ti(III) or ^{98}Mo(V). In most cases, however, more complicated spectra are observed as additional magnetic and electric fields are exerted by the environment of the unpaired electron. In many cases further complications arise from the presence of more than one electron, e.g. for TM ions with several unpaired *d*-electrons (up to five for high-spin Mn^{2+} or Fe^{3+}) or organic molecules in triplet states. If the interactions between the different magnetic and electric moments and fields are smaller than the electron Zeeman term, they can be described by additional terms in the spin Hamiltonian in Eq. (2.1) and will lead to further splittings of the energy levels in Figure 2-1.

For TM ions like VO^{2+} or Mn^{2+} the interactions can be much larger than the electron Zeeman term, depending on the nature and the symmetry of the chemical environment of the ion. In this case the energy of the MW frequency may be to small to excite all the transitions. Furthermore only the lowest energy levels are populated with electrons if the energy splitting is much larger than kT, where k is the Boltzmann constant ($J \cdot K^{-1}$) and T the temperature (K). In this case EPR spectra can only be observed in the ground state manifold of the paramagnetic system.

For TM ions in the condensed phase the interactions responsible for the large splittings are the *crystal-field* (CF) *splitting* and the *spin-orbit coupling* (SOC). The com-

bined effect of these two interactions removes the orbital degeneracy of the energy levels for most TM ions completely, leaving a non-degenerate ground state, often with zero orbital angular momentum (quenching of the orbital angular momentum, p. 9).

The effect of an octahedral CF on a TM ion is illustrated in the first part of Figure 2-2 with the arrangement of the ligands drawn schematically in the inset. The energy splitting in the case of octahedral symmetry is given by Δ.

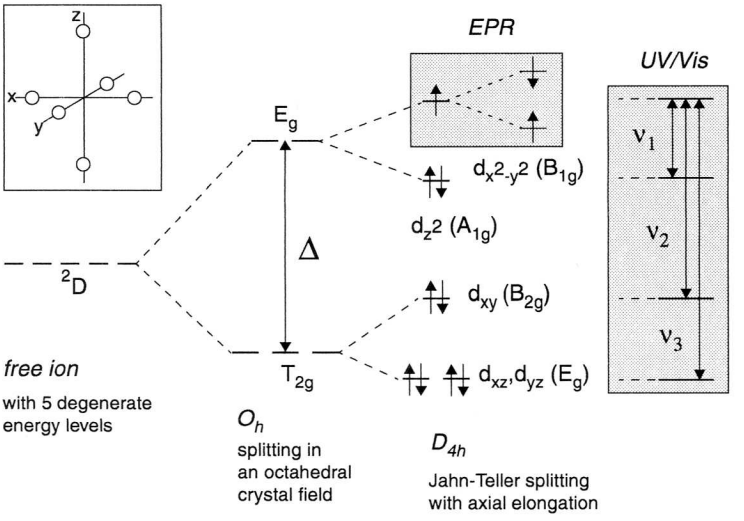

Fig. 2-2 Illustration of the effect of an octahedral CF on the energy levels of a $3d^9$ TM ion. The resulting energy splitting is Δ. The degeneracy of the orbitals is further lifted by a Jahn-Teller effect through an elongation of the axial bonds, leading to the optical transitions ν_1, ν_2 and ν_3. The geometrical arrangement of the ligands is schematically shown in the inset. The Zeeman splitting of the ground level (B_{1g}) is indicated in the small shaded box.

In the special case of the $3d^9$ ion in O_h symmetry, the degeneracy of the E_g term is not affected by the SOC and the Jahn-Teller theorem applies. The orbital degeneracy is lifted and the energy of the system lowered by a displacement of the ligands on the *z*-axis. An elongation of the coordination octahedron leads to the energy level scheme shown in Figure 2-2 with the unpaired electron in the $d_{x^2-y^2}$ orbital. The electronic transitions ν_1, ν_2 and ν_3 are indicated by arrows in the large shaded area.

The measurement of EPR spectra is limited to the Zeeman splitting imposed by an external field on the unpaired electron in the non-degenerate $d_{x^2-y^2}$ orbital (small shaded area in Figure 2-2) and one could think that the spin system can now be described by the spin Hamiltonian in Eq. (2.1) with $S = 1/2$ since the ground state is non-degenerate and has only associated spin angular momentum. The ligand field can, however, act on the electron spin through second order effects of the SOC. Since the ground state of most molecules has zero orbital angular momentum due to the quenching by chemical bonding (e.g. radicals) or large CF's (e.g. TM ions) the SOC is zero to first order and the influence of the electric CF's on the electron spin negligible. The g-factor should thus have precisely the free-electron value. Interaction between the ground state and excited states, however, admixes small amounts of orbital angular momentum to the ground state which couple to the electron spin and make the electron spin sensitive to its crystalline environment. As a result the g-factor is no longer isotropic - the splitting of the Zeeman levels depends on the symmetry of the ligand field and the orientation of the system in the external magnetic field. The effects of the anisotropy of the EZI on the EPR spectra will be discussed in the next chapter.

Generally for the description of the EPR spectra in the ground state of a paramagnetic ion, an "effective" spin Hamilton operator is introduced which strongly depends on the involved energy terms and thus on the individual ion and its environment. The influence of the environment is included in a number of parameters such as the **g** matrix or the zero-field splitting tensor **D** (for $S>1/2$). The spin operator $\boldsymbol{S}$ used in the spin Hamiltonian is an "effective" spin, reflecting the number of energy levels involved in the EPR spectrum and does not necessarily refer to the true electron spin quantum number as it is e.g. the case for the Cu^{2+} ion. However, this has no influence on the theory and no difference will be made between effective spin and true electron spin in the following.

2.1.3 g Anisotropy

When dealing with magnetic moments in a crystalline or molecular environment one has to be aware that the CW and pulse EPR spectra may either depend on the orientation of the sample in the magnetic field $\boldsymbol{B}_0$ (e.g. single crystals) or are superpositions of many different single crystal spectra with random orientation (e.g. powder samples). In solu-

tion rotational and translational motion of the molecules often averages out the anisotropic interactions. Due to short relaxation times pulse EPR measurements have to be performed at low temperatures where molecular motion is frozen. These 'frozen solutions' EPR spectra are qualitatively identical to powder spectra. Thus the concept of anisotropy is of importance and we will discuss the anisotropy of the EZI in more detail.

In the first example the only magnetic field experienced by the electron spin was the external magnetic field $\boldsymbol{B}_0$ and the spin vector $\boldsymbol{S}$ was oriented either parallel or antiparallel to $\boldsymbol{B}_0$. As shown above additional inner fields, transmitted to the electron spin by the SOC, are present in molecular systems which may be larger than the external field. These fields are related to the symmetry of the molecule, e.g. to the CF of a TM ion. The effective field $\boldsymbol{B}_{eff}$ experienced by the electron spin in a molecular or crystalline environment is a superposition of the external and internal fields. For an anisotropic system Eq. (2.1) is written

$$\mathcal{H} = g_e \frac{\beta_e}{h} \boldsymbol{B}_{eff} \boldsymbol{S} = \frac{\beta_e}{h} \boldsymbol{B}_0 \mathbf{g} \boldsymbol{S}. \tag{2.4}$$

In the second part of Eq. (2.4) the orientation dependent variation of the Zeeman splitting is expressed by a (3x3) **g** interaction matrix. The information about the symmetry of the inner fields is thus transferred to a **g** matrix and can be obtained experimentally by determining the principal values of this matrix. In general the **g** matrix will be orthorhombic and is expressed in its principal axes system (PAS) by

$$\mathbf{g} = \begin{bmatrix} g_x & & \\ & g_y & \\ & & g_z \end{bmatrix}, \tag{2.5}$$

where *(x,y,z)* is the PAS and g_x, g_y and g_z are the principal values of **g**. For $\boldsymbol{B}_0$ along one of the principal axes, the electron spin vector is quantized along $\boldsymbol{B}_0$ and the resonant field is obtained by inserting the corresponding principal value into Eq. (2.3). For an arbitrary orientation of $\boldsymbol{B}_0$ the expression for the resonant field is obtained by insertion of the following expression into the resonance condition:

$$g^2 = g_x^2 l_x^2 + g_y^2 l_y^2 + g_z^2 l_z^2, \tag{2.6}$$

where l_x, l_y and l_z are the direction cosines between $\boldsymbol{B}_0$ and the three principal axes (x,y,z).

To illustrate the effect of **g** anisotropy on the EPR spectrum we consider the special case where the CF has axial symmetry (e.g. a TM ion in octahedral coordination with a tetragonal distortion along the z axis). In this case the EZI is described by two parameters $g_\perp$ and $g_\parallel$ given by

$$g_\perp = g_x = g_y, g_\parallel = g_z. \tag{2.7}$$

Eq. (2.6) can now be rewritten with a single angle θ between the magnetic field vector $\boldsymbol{B}_0$ and the z axis.

$$g(\theta)^2 = g_\perp^2 \sin^2\theta + g_\parallel^2 \cos^2\theta. \tag{2.8}$$

In Figure 2-3 an axial **g** matrix with $g_\parallel > g_\perp$, represented by a rotational ellipsoid, and the line shape of the corresponding EPR spectrum are drawn, assuming a large number of paramagnetic systems with random orientation of their **g** ellipsoids with respect to the static magnetic field $\boldsymbol{B}_0$. This situation is typical for a powder sample. For a given

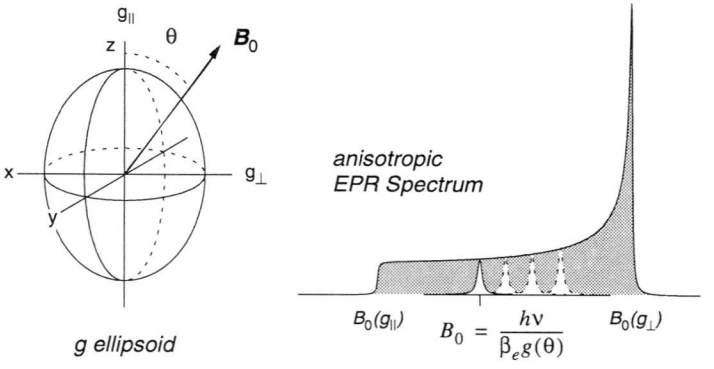

Fig. 2-3 Schematic drawings of the axial **g**-ellipsoid and the corresponding EPR spectrum. The powder line shape results from the contributions of a large number of individual spin packets with different resonance positions (some examples are shown).

magnetic field strength B_0, all spins fulfilling the resonance condition $g(\theta) = h\nu/\beta_e B_0$, i.e. all spins for which $\boldsymbol{B}_0$ makes an angle θ with the z-axis of the **g** ellipsoid, contribute to the spectrum and are considered to form a spin packet. These spin packets are schematically exemplified in the powder line shape in Figure 2-3. The extreme positions of the powder spectrum are obtained by inserting $g_\parallel$ and $g_\perp$ into the resonance condition. Note that for $g_\parallel > g_\perp$ one obtains $B_0(g_\parallel) < B_0(g_\perp)$ due to the inverse proportionality of g and B_0. The asymmetric line shape is mainly due to the fact that the number of spin packets contributing to the spectrum is much larger in the xy-plane than along the z-axis.

The case discussed above is typical for the Jahn-Teller distorted Cu^{2+} complex in octahedral symmetry. The degeneracy of the ground state in the octahedral coordination field is removed either by an elongation or a compression along the z-axis. The axial symmetry of the **g** matrix thus reflects the symmetry of the ligand field.

2.2 Interaction with Nuclear Spins

So far the interaction of the electron spin with the external magnetic field yields an EPR spectrum with one single line which may be broadened due to the **g** anisotropy. The information content of the EPR spectrum is considerably increased if nuclei with a spin quantum number $I > 0$ are found in the environment of the electron spin, as e.g. protons ($I = 1/2$) or nitrogen atoms ($I = 1$). The intrinsic spin angular momentum of these nuclei is associated with a magnetic moment. In addition to the external magnetic field $\boldsymbol{B}_0$ the electron spin will now experience the local magnetic fields built up by the nuclei close to the unpaired electron. The interaction of the electron spin with these nuclear magnetic moments is called *hyperfine interaction* (HFI).

In analogy to the electron spin the nuclear spin $\boldsymbol{I}$ is quantized in a magnetic field resulting in the nuclear Zeeman splitting of the nuclear spin states. The *nuclear Zeeman interaction* (NZI) is expressed by

$$\mathcal{H}_n = -g_n \frac{\beta_n}{h} \boldsymbol{I} \boldsymbol{B}_0 . \tag{2.9}$$

Here g_n is the dimensionless nuclear g-factor, a constant depending on the type of

nucleus, and β_n the nuclear magneton ($J \cdot T^{-1}$). For a given nuclear quantum number I a splitting into $(2I+1)$ energy levels is observed, each level being characterized by a nuclear magnetic spin quantum number $m_I = I, I-1, \ldots, -I$. The NZI is much smaller than the EZI (e.g. the ratio $g\beta_e/g_n\beta_n = 660$ for an unpaired electron with $g = 2$ and a proton with $g_n = 5.58$) and the small anisotropy is usually neglected in EPR. The local magnetic fields set up by the nuclear spins through the HFI at the electron spin depend on the orientation of the nuclear magnetic moment with respect to the external magnetic field[1]. This results in a splitting of each electron spin state into $(2I+1)$ levels.

2.2.1 Hyperfine Interaction

Two mechanisms with different physical origin can contribute to the coupling between electron and nuclear spins. The first mechanism is the *dipole-dipole interaction* between the magnetic moments of the electron and nuclear spin in analogy to the classical dipolar interaction between magnetic moments. The energy of this interaction is written as

$$\mathcal{H}_{dd} = \frac{1}{4\pi}\frac{\mu_0}{r^3 h} g\beta_e g_n \beta_n \left[\boldsymbol{SI} - \frac{3}{r^2}(\boldsymbol{Sr})(\boldsymbol{Ir}) \right], \tag{2.10}$$

where μ_0 is the permeability of the vacuum ($4\pi \cdot 10^{-7}$ $N \cdot A^{-2}$) and r the distance between the two spins (in m), considered to be located at a single point in space (point dipole approximation) and connected by the vector $\boldsymbol{r}$. The dipole-dipole interaction depends on the relative orientation of the magnetic moments and is thus anisotropic. Purely dipolar interaction is expected e.g. if the electron spin is located in a molecular orbital with a nod at the nucleus (*p*-, *d*- or *f*-orbitals).

The second mechanism becomes important if there is finite spin density of the electron spin at the nucleus. This is the case if there are contributions of *s*-orbitals to the molecular orbital. The energy term of this so-called *Fermi contact interaction* is given by

1. Note that the hyperfine fields exerted by the electron spin at the nucleus are much stronger than the nuclear hyperfine fields. They may easily exceed the NZI. In this case the nuclear spin is not quantized along the external magnetic field $\boldsymbol{B}_0$ but along an effective field set up mainly by the electron spin through the HFI. The consequences of the weak and strong hyperfine coupling are discussed in more detail for the $S = 1/2$, $I = 1/2$ system (section 2.2.2).

$$\mathcal{H}_{contact} = \left(\frac{2}{3}\right)\frac{\mu_0}{h} g\beta_e g_n \beta_n |\Psi(0)|^2 \boldsymbol{SI}. \tag{2.11}$$

Here $|\Psi(0)|^2$ is the probability density of the unpaired electron in the *s*-orbital. The Fermi contact interaction is isotropic and is encountered also in systems with their unpaired electrons in *p*-, *d*- or *f*-orbitals like π-radicals or TM ions. The spin density at the nucleus is then induced by mechanisms like configuration interactions or spin polarization [28].

In general the HFI will be anisotropic due to the dipolar interaction, except for systems where the anisotropic part is averaged out (e.g. by molecular motion in solution). Both mechanisms are then combined to form the hyperfine interaction matrix **A** and the following term is added to the spin Hamiltonian

$$\mathcal{H}_{hf} = \boldsymbol{SAI}, \tag{2.12}$$

where the hyperfine interaction matrix **A** is given by

$$\mathbf{A} = \begin{bmatrix} A_x & & \\ & A_y & \\ & & A_z \end{bmatrix} = \mathbf{1}a_{iso} + \begin{bmatrix} A_x^d & & \\ & A_y^d & \\ & & A_z^d \end{bmatrix} \tag{2.13}$$

in its PAS. The purely dipolar part is expressed by the second, traceless matrix.

In Figure 2-4 the effect of the hyperfine coupling on the energy level diagram and the EPR spectrum is illustrated for the simple case of isotropic EZI and HFI for a spin $I = 3/2$ (e.g. Cu^{2+})[2]. The coupling between the electron and nuclear spin results in a splitting of each electron spin state into 4 levels. MW irradiation causes transitions between levels with $\Delta m_S = \pm 1$ and $\Delta m_I = 0$ (only the electron spin is affected by the microwave irradiation). The four allowed transitions are shown in the energy level diagram. The resulting EPR spectrum consists of four lines centered about g_{iso} and split by a_{iso}. The

2. The NZI of the Cu^{2+} ions is much smaller than the HFI and thus neglected in the drawing. The sign of g_n (>0 in Figure 2-4) is, however, important for the order of the m_I states in the different m_S manifolds.

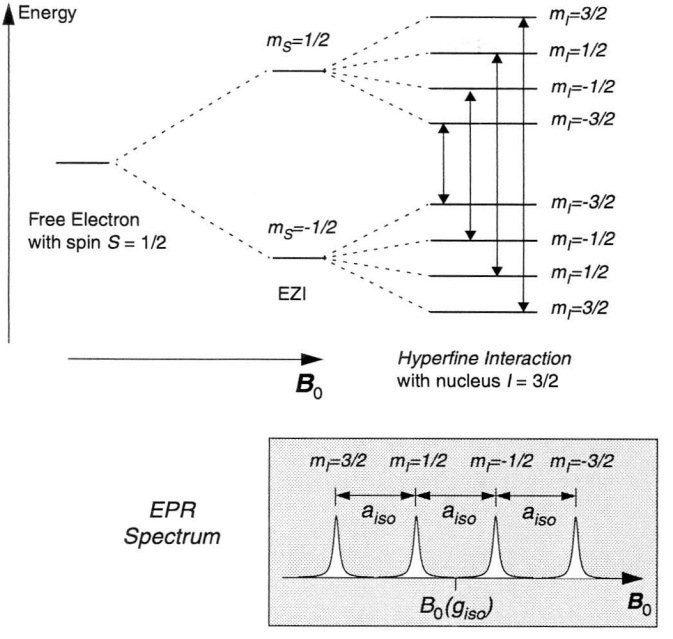

Fig. 2-4 Energy level diagram and resulting EPR spectrum for a spin system with one electron $S = 1/2$ and a nucleus $I = 3/2$ with isotropic electron Zeeman (g_{iso}) and hyperfine (a_{iso}) interactions.

transitions are labelled by their nuclear magnetic spin quantum numbers. For anisotropic hyperfine interactions powder line shapes are observed for the individual lines as discussed for the **g** anisotropy (see also section 2.4).

2.2.2 The $S = 1/2, I = 1/2$ system

For the theoretical description of pulse EPR spectra it is often not necessary to consider the complete spin Hamiltonian. For an $S = 1/2$ system the quantization axis of the electron spin is mainly determined by the EZI and the influence of the nuclear spins on this axis can be neglected (*high-field approximation*). Furthermore the coupling between the different nuclear spins, most important in NMR, can be neglected compared to the large coupling of the nuclei to the unpaired electron. It is then possible to divide the complete tensor space into subspaces which contain the interactions between the spin $S = 1/2$

and a single nuclear spin I. This subspaces can be treated separately and the complete spectrum is obtained by the combination of the results. For spin systems with $S > 1/2$ a fictitious spin $S' = 1/2$ can be assigned to the given electron transition if the energy differences between the transitions are larger than the excitation bandwidth of the mw pulses (which is mostly the case) and the same treatment can be applied for the calculation of the spectrum (see e.g. [29]).

The possibility to reduce the dimensionality of the Hamiltonian often allows experimental pulse EPR spectra of $I = 1/2$ nuclei like ^{13}C and H to be discussed in terms of a simple *$S = 1/2$, $I = 1/2$ system*. This system has the major advantage that it can be treated analytically. The analytical formulae presented in this section are also of importance for the development and understanding of pulse sequences. For the derivation of the formulae **g** anisotropy is neglected and the electron spin $\boldsymbol{S}$ is considered to be quantized along the external magnetic field $\boldsymbol{B}_0$. Combination of Eq. (2.9) and Eq. (2.12) yields a nuclear spin Hamiltonian for each m_S manifold [30]

$$\mathcal{H}_{\alpha,\beta} = -\frac{g_n\beta_n}{h}\boldsymbol{B}_0\boldsymbol{I} + \langle \boldsymbol{S}\rangle_{\alpha,\beta}\mathbf{A}\boldsymbol{I}. \tag{2.14}$$

In this notation $\langle \boldsymbol{S}\rangle_{\alpha,\beta}$ is the expectation value of spin of the α/β electron spin states, equal to $m_S = \pm 1/2$ in our simple case. The nuclear spin Hamiltonian can be expressed in the laboratory frame, where the static magnetic field vector $\boldsymbol{B}_0 = B_0[0\ 0\ 1]$ is taken along the laboratory z-axis. Furthermore it is assumed without loss of generality that the nucleus lies in the xz-plane of the coordinate system. In the resulting expression

$$\mathcal{H}_{\alpha,\beta} = \nu_I I_z + m_S(AI_z + BI_x) = \nu_I I_z \pm \frac{1}{2}(AI_z + BI_x), \tag{2.15}$$

ν_I is given by $-g_n\beta_n B_0/h$; $A = A_{zz}$ and $B = \sqrt{A_{zx}^2 + A_{zy}^2}$, the secular and pseudo-secular parts of the HFI, are functions of hyperfine matrix elements, expressed in the laboratory frame. Diagonalization of this Hamiltonian yields the following expressions for the nuclear frequencies [31]

$$\left|\begin{matrix}\nu_\alpha \\ \nu_\beta\end{matrix}\right| = \sqrt{\left(\pm\frac{A}{2}+\nu_I\right)^2+\left(\frac{B}{2}\right)^2}. \tag{2.16}$$

In first approximation, the coupling between the electron and the nuclear spin is often treated in the point dipole approach, where the electron spin density is considered to be located at a single point in space (e.g. on the central atom of a TM nucleus) without delocalization to the ligand nuclei. The hyperfine matrix **A** is then expressed in its PAS by

$$\mathbf{A} = \begin{bmatrix} A_1 = A_\perp & & \\ & A_2 = A_\perp & \\ & & A_3 = A_\parallel \end{bmatrix} = \mathbf{1}a_{iso} + \begin{bmatrix} -T & & \\ & -T & \\ & & 2T \end{bmatrix}, \tag{2.17}$$

where the second matrix in Eq. (2.17), representing the dipolar coupling, is axially symmetric with

$$T = \left(\frac{\mu_0}{4\pi}\right)\frac{g_e g_n \beta_e \beta_n}{hr^3}. \tag{2.18}$$

The dipolar coupling constant T is a function of the nuclear g_n factor and the electron-nuclear distance r. For isotropic g the largest dipolar coupling ($2T$) is found along the vector $\boldsymbol{r}$ connecting electron and nucleus. The principal values of these coupling matrices are related to the parameters A and B in Eq. (2.16) by

$$A = A_\parallel \cos^2\theta + A_\perp \cos^2\theta = a_{iso} + T(3\cos\theta^2 - 1) \text{ and} \tag{2.19}$$

$$B = (A_\parallel - A_\perp)\sin\theta\cos\theta = 3T\sin\theta\cos\theta. \tag{2.20}$$

Here θ is the angle between the principal axis of the dipolar coupling matrix ($A_\parallel$) and the magnetic field vector $\boldsymbol{B}_0$. In Figure 2-5 these parameters are shown in a schematic drawing. The frequencies ν_α and ν_β are centered about ν_I in the weak coupling limit ($\nu_I > |a_{iso}/2+T|$, see section 2.2.3). The coupling varies from $A_\parallel$ ($\theta = 0°$, $\boldsymbol{B}_0$ along the z-axis) to $A_\perp$ ($\theta = 90°$, $\boldsymbol{B}_0$ in the equatorial plane).

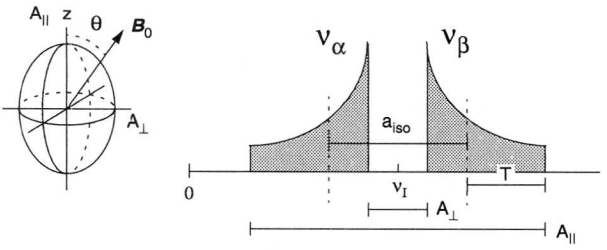

Fig. 2-5 Schematic drawing of the distribution of the basic frequency features ν_α and ν_β for an axial HFI matrix, indicated by the ellipsoid in the inset.

It has already been mentioned before that the two terms in this Hamiltonian describe the magnetic fields, set up at the nucleus by the external magnetic field $\boldsymbol{B}_0$ (first term) and by the electron through the hyperfine coupling (second term). The nuclear spin will be quantized along the resulting of these two contributions. For the interpretation of the spectra it is important to know which contribution is the dominant one. The NZI depends on the g_n-factor and is in the range of several MHz. The hyperfine coupling (e.g. up to 500 MHz for the copper atom) may thus by far exceed the NZI.

Depending on the dominant interaction one has to consider the *weak coupling* or *strong coupling* case which are discussed in the next section. Weak coupling is found e. g. for the water protons in the first coordination sphere of the copper-hexaaquo complex whereas the strong coupling situation is typical for most couplings observable in CW EPR spectra. In the third case, the so called *matching range*, the two contributions are of equal size. This situation is found for the ^{13}C nuclei of the carbonate ions coordinated in a bidentate fashion to the copper nucleus as shown in chapters 5 and 6.

2.2.3 Weak and Strong Coupling

For the discussion of the weak and strong coupling we consider again an $S = 1/2$, $I = 1/2$ system with an isotropic g_{iso}-value and isotropic coupling $a_{iso} > 0$. We assume that the high field approximation is valid so that all spins, electrons and nuclei, are quantized along the direction of the magnetic field vector $\boldsymbol{B}_0$, taken along z. The magnetic field set up by the HFI at the nucleus is therefore directed along the z-axis. The energy levels of this system are obtained by setting $B = 0$ in Eq. (2.15).

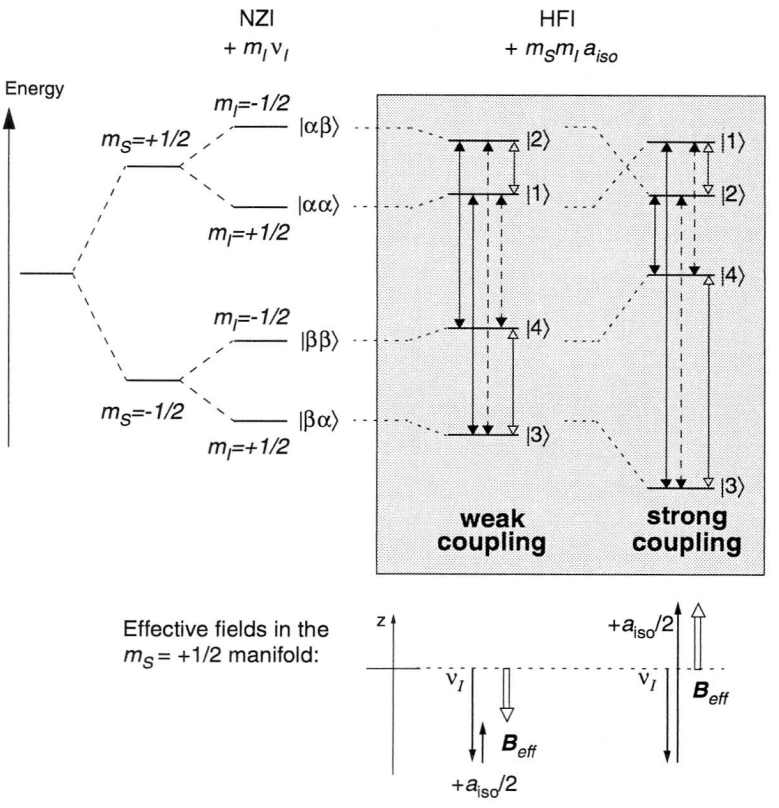

Fig. 2-6 (top) Energy level scheme for an $S = 1/2$, $I = 1/2$ system in the weak and strong coupling case together with the possible electron and nuclear spin transitions. (bottom) Schematic drawing of the effective magnetic fields set up at the nucleus by the superposition of the NZI and HFI for the $m_S = +1/2$ manifold.

In Figure 2-6 the energy level schemes are drawn for the weak and the strong coupling case. It is assumed that $\nu_I < 0$ and $a_{iso} > 0$. The electron and nuclear Zeeman levels are indexed by their magnetic quantum numbers m_S and m_I and commonly designated by $|\alpha\alpha\rangle$, $|\alpha\beta\rangle$, $|\beta\alpha\rangle$ and $|\beta\beta\rangle$, where $|\alpha\rangle$ and $|\beta\rangle$ refer to the two spin states in the external magnetic field. In general m_I is not a good quantum number for the characterization of the energy levels since the quantization axis of the nuclear spin deviates from the direction of the external magnetic field due to the HFI. For this reason a new numbering of the

levels is introduced, namely $|1\rangle$, $|2\rangle$, $|3\rangle$ and $|4\rangle$. The numbering of the levels in the weak and strong coupling case is shown in the figure.

In the *weak coupling* case ($\nu_I > a_{iso}/2$) the direction of quantization of the nuclear spin is given in first order by the external magnetic field $\boldsymbol{B}_0$. This is illustrated in the vector diagram at the bottom of Figure 2-6 for the $m_S = +1/2$ manifold. The magnetic fields put up by the NZI and the HFI are drawn along the z-axis and have opposite directions. The effective quantization vector, experienced by the nucleus and indicated by the bold arrow, is obtained by the addition of both contributions. The hyperfine field slightly decreases the energy splitting caused by the NZI.

In the *strong coupling* case ($\nu_I < a_{iso}/2$) the direction of quantization of the nuclear spin is determined by the hyperfine field $a_{iso}/2$. The NZI gives only a small contribution to the effective field. Again the fields act in opposite directions in the $m_S = +1/2$ manifold.

In the $m_S = -1/2$ the nuclear Zeeman and hyperfine fields act in the same direction for both weak and strong coupling. The splitting between the Zeeman states is thus increased as can be inferred from the energy level diagram in Figure 2-6.

We now consider the more general case where additional terms in the spin Hamiltonian cause the quantization axis to deviate from the z-axis. This is e.g. the case when the high-field approximation is no more valid and S_x and S_y have to be considered or when the coupling is anisotropic ($B <> 0$). As a result not only the magnitude of the effective field experienced by the nucleus but also the direction is changed when going from one m_S to another. This has important effects on the transition frequencies observable in the four level system as a change in the m_S spin state can now also affect the spin state of the nucleus. The transition probability of the so-called *forbidden transitions* increases. In Figure 2-6 the six possible transitions between the four levels are indicated both for the weak and strong coupling case. The allowed electron transitions, involving only a spin flip of the electron ($\Delta m_S = \pm 1$, $\Delta m_I = 0$) are indicated by full arrows, the forbidden electron transitions where both the electron and the nuclear spins flip ($\Delta m_S = \pm 1$, $\Delta m_I = \pm 1$) by dashed arrows. The hollow arrows represent the nuclear transitions which take place within the m_S manifolds. Note that in our example with isotropic coupling the forbidden transitions have zero transition probability.

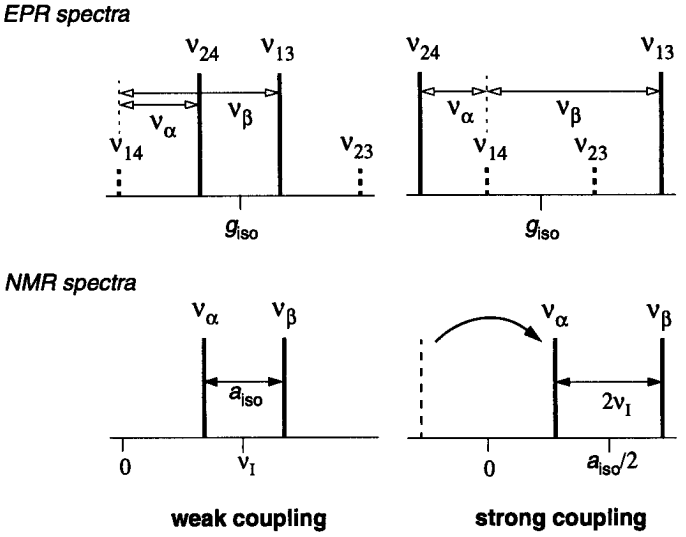

Fig. 2-7 (top) EPR stick spectra observed for the energy level schemes in Figure 2-6 for the weak and strong coupling case. The allowed and forbidden electron transitions are drawn as solid and dashed lines, respectively. The nuclear frequencies are indicated as energy differences between the electron transitions. (bottom) Corresponding NMR spectra with positive frequencies only.

The EPR and NMR spectra, obtained for the energy level schemes in Figure 2-6 are drawn schematically in Figure 2-7 for the weak and strong coupling case. In the EPR spectrum allowed (solid lines) and forbidden (dashed lines) transitions and are centered around g_{iso}. The numbering of the frequencies is taken from the energy level scheme with $\nu_{ij} = E_i - E_j$. The nuclear transition frequencies ν_α and ν_β are shown as energy differences between the allowed and forbidden transitions. They are given by the absolute values of the transition frequencies ν_{12} and ν_{34}. In the NMR spectrum in Figure 2-7 only positive frequencies are observed therefore with the consequence that ν_α and ν_β are centered around $a_{iso}/2$ and separated by $2\nu_I$ in the strong coupling case.

The intensities of the allowed and forbidden electron transitions are given by

$$I_a = \cos^2\eta = \frac{\left|\nu_I^2 - \frac{1}{4}\nu_-^2\right|}{\nu_\alpha \nu_\beta} \qquad \text{and} \qquad (2.21.a)$$

$$I_f = \sin^2\eta = \frac{\left|\nu_I^2 - \frac{1}{4}\nu_+^2\right|}{\nu_\alpha \nu_\beta}, \tag{2.21.b}$$

where $\nu_+ = \nu_{12} + \nu_{34}$ and $\nu_- = \nu_{12} - \nu_{34}$. The angle η is the half sum of the angles between the external magnetic field and the effective field vectors acting on the nucleus in the two m_S manifolds. It is obtained by the diagonalization procedure of the Hamiltonian in Eq. (2.15) and has to be chosen as $-45° < \eta \leq 45°$ for the numbering of the levels in Figure 2-6 to be correct. More detailed descriptions are found in [32] and [33]. From these formulae it can be seen that for $\eta = 0$ (all fields along z as in Figure 2-6) the intensity of the forbidden transitions is zero.

2.2.4 Matching Range and Exact Cancellation

The transition from the weak coupling to the strong coupling case is caused either by an increase of the hyperfine coupling or by a decrease of the magnetic field and thus the magnitude of the NZI. At one point a situation is reached where the hyperfine splitting is twice the nuclear Zeeman frequency in the $m_S = +1/2$ manifold ($\nu_I = a_{iso}/2$) which leads to the exact cancellation of the nuclear Zeeman field and the hyperfine field. The effective magnetic field, experienced by the nucleus, and thus also the nuclear frequency ν_α is zero at this point. In the energy level scheme in Figure 2-6 the energy levels $|1\rangle$ and $|2\rangle$ come very close (they are not allowed to cross). In this situation the angle η becomes 45° and allowed and forbidden transitions have equal intensity.

We consider again the $S = 1/2$, $I = 1/2$ system with the anisotropic HFI discussed in section 2.2.2 as the cancellation effects are of importance for the nuclear frequency (NMR) spectra of disordered systems. The NMR spectrum for such a system in the weak coupling case was already shown in Figure 2-5. In the strong coupling case the situation is analogous to the one shown in the bottom of Figure 2-7. The broad ν_α powder line is mirrored about the origin so that the line shape is inverted. The *matching range* for the $S = 1/2$, $I = 1/2$ system defined in section 2.2.2 is given by the following conditions [34,35]

$$\left|\frac{a_{iso}}{2} + T\right| < \nu_I < \left|\frac{(a_{iso} - T)}{2}\right|. \tag{2.22}$$

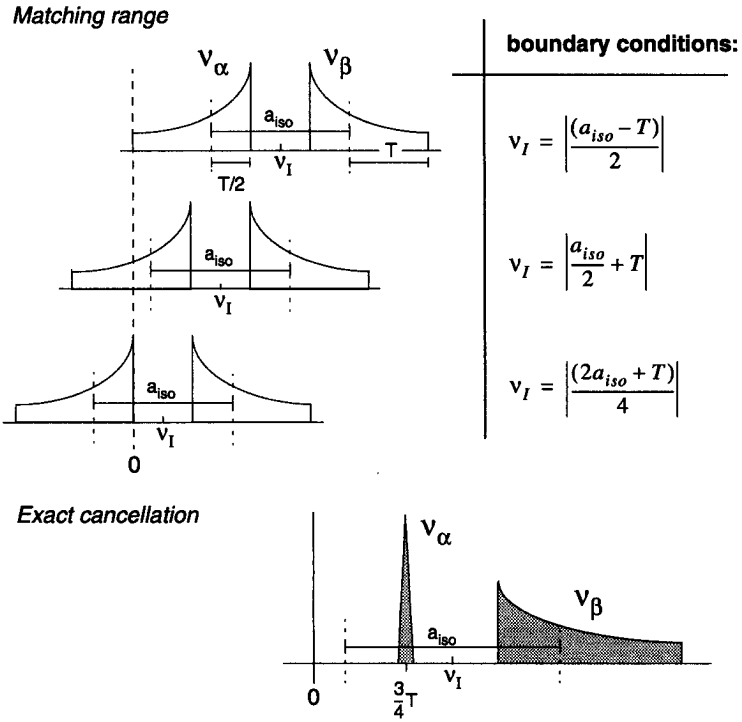

Fig. 2-8 Schematic illustration of the matching range with the boundary conditions given as functions of a_{iso} and T, both assumed to be positive. At exact cancellation the ν_α line narrows to an isotropic peak.

These boundary conditions are illustrated schematically in Figure 2-8. For $\nu_I = |(2a_{iso}+T)/4|$ the *exact cancellation* condition is reached. At this point a line shape singularity is induced for the ν_α manifold, independent of the angle θ and an isotropic line is observed at the frequency $\frac{3}{4}T$.

2.2.5 Combination Lines in ESEEM Experiments

So far we have only discussed the basic frequencies ν_α and ν_β observed in the $S = 1/2$, $I = 1/2$ system. In two-pulse and four-pulse ESEEM experiments also combination lines ν_+ or ν_- are observed. In disordered systems the basic frequencies are broad and show rapidly decaying signals which may be completely hidden in the spectrometer deadtime of typically 100 ns. The *sum combination peak* ν_+ shows a much

narrower frequency distribution and useful information can be extracted from its shape [36-38].

This is illustrated in Figure 2-9 for the $S = 1/2$, $I = 1/2$ system with axial HFI. In the two-dimensional plot the basic frequencies ν_α and ν_β as well as the sum peak ν_+ are drawn as a function of θ, using Eq. (2.16) and defining ν_+ as $(\nu_\alpha + \nu_\beta)$. Projection of the two-dimensional plot on the frequency axis with scaling of the frequency intensities by $\sin\theta$ to account for the powder line shape yields the frequency distribution shown at the top of Figure 2-9. The sum peak clearly shows a much narrower frequency distribution with two singularities. For $\theta = 0°/90°$ the sum peak frequency ν_+ equals $2\nu_I$. The departure from this value for intermediate θ values is solely governed by the anisotropic part of the hyperfine interaction. At the frequency position given by

$$(\nu_\alpha + \nu_\beta)_{max} \cong 2\nu_I + \frac{9}{16}\frac{T^2}{\nu_I} \tag{2.23}$$

a turning point is observed which yields another singularity in the lineshape of the sum peak. The maximum shift $\Delta_{max} = \frac{9}{16}\frac{T^2}{\nu_I}$ from the twice the nuclear Zeeman fre-

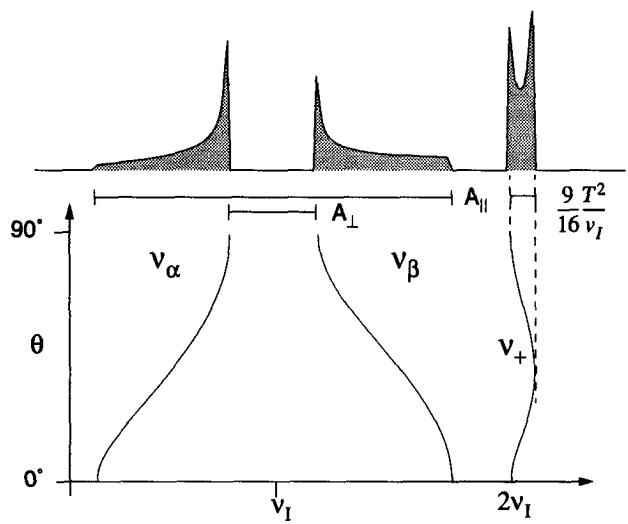

Fig. 2-9 Illustration of the θ dependence of the basic frequencies ν_α and ν_β and the sum combination peak ν_+ (bottom). The projection of the orientations weighted with $\sin\theta$ on the frequency axis yields the line shapes shown in the upper part.

quency is observed at a θ value of approximately 45°. While the narrow peaks for θ close to 0°/90° vanish in the ESEEM experiments due to the modulation depth factor k the narrow peak at the turning point remains, giving a slowly decaying time signal which survives the spectrometer deadtime. From the position of this peak with respect to the double nuclear Zeeman frequency $2\nu_I$ the dipolar coupling constant T can be calculated.

2.3 The Complete Spin Hamiltonian

2.3.1 Zero-Field Splitting

So far we have discussed the case for one electron spin in magnetic fields of different origins. For systems with more than one electron spin ($S > 1/2$) an additional energy term, reflecting the strong dipole-dipole interactions between the electrons, has to be included in the spin Hamiltonian[3]. Examples for such systems are TM ions with up to five unpaired d-electrons (e.g. high-spin Mn^{2+}) or spin triplets in organic molecules. The zero-field splitting term, which is active also in absence of the external magnetic field, is written as

$$\mathcal{H}_{zfs} = \boldsymbol{S}\mathbf{D}\boldsymbol{S}, \tag{2.24}$$

where **D** is the traceless zero-field interaction or fine structure tensor. The zero-field interaction can be much larger than the EZI, depending on the symmetry of the ligand field and the coupling of the electron spins.

2.3.2 Nuclear Quadrupole Interaction

The last term in the spin Hamiltonian that will be considered here is found for nuclei with a nuclear spin quantum number $I > 1/2$. The physical origin of this term is the interaction of the electric quadrupole moment of these nuclei with the electric field gradient. This field gradient arises from uneven distributions of electric charges around the nucleus. The NQI is given by

3. The **D** tensor may also contain second-order correction terms from the spin-orbital coupling.

$$\mathcal{H}_{nqi} = \boldsymbol{IQI}, \tag{2.25}$$

where **Q** is the traceless nuclear quadrupole tensor. The NQI can be formally treated in the same way as the ZFS. It's impact on the EPR spectrum is, however, much smaller and the term can often be neglected.

As for this thesis, systems with $S > 1/2$, $I > 1/2$ are of minor importance, we will not extent the discussion of these terms any further.

2.3.3 Summary of Energy Terms

The energy terms introduced in the preceding sections and describing the interactions of the electron and nuclear spins among themselves and with their environment can be added to form the complete spin Hamiltonian:

$$\mathcal{H}_{sp} = \frac{\beta_e}{h}\boldsymbol{B}_0\mathbf{g}\boldsymbol{S} + \boldsymbol{SDS} + \boldsymbol{SAI} - g_n\frac{\beta_n}{h}\boldsymbol{IB}_0 + \boldsymbol{IQI}. \tag{2.26}$$

Depending on the electron and nuclear spin quantum numbers of the interacting ions and their relative magnitudes terms can be neglected (e.g. the zero-field splitting for $S = 1/2$). If the electron is coupled to more than one nuclear spin, the Hamiltonian can be extended by adding the appropriate terms. Knowledge of the complete spin Hamiltonian including the magnitude of the interactions and the relative orientations of PAS's of the interaction matrices allows for the calculation of the CW and pulse EPR spectra. The appropriate mathematical tools are presented in Appendix A. The procedure is illustrated in the next chapter for Cu^{2+}.

2.4 EPR of Cu^{2+} Complexes

The spin Hamiltonian for a spin system consisting of a Cu^{2+} ion (S = 1/2, I = 3/2) with weakly coupled nuclei from ligands in the first and second coordination spheres (e. g. ^{13}C nuclei and protons) can be written as follows:

$$\mathcal{H}_{sp} = \frac{\beta_e}{h}\boldsymbol{B}_0\mathbf{g}\boldsymbol{S} + \boldsymbol{S}\mathbf{A}^{Cu}\boldsymbol{I} + \mathcal{H}_N. \tag{2.27}$$

The electron Zeeman interaction is much larger than the hyperfine coupling to the copper nucleus, expressed by $\mathbf{A}^{Cu}$. The copper quadrupole interaction is neglected. The $\mathbf{g}$ and $\mathbf{A}^{Cu}$ matrices are assumed to be coaxial and axially symmetric and no distinction is made between the two copper isotopes. These simplifying assumptions are often justified in experimental work. The third term $\mathcal{H}_N$ describes the ^{13}C and proton interactions which are small compared to the first and second term. The CW EPR spectrum is then obtained by neglecting the last term and treating the copper hyperfine interaction e.g. by second order perturbation theory (Appendix A). The EPR spectrum is described by the principal values $g_{\|}$, $g_{\perp}$, $A_{\|}$, $A_{\perp}$ of the $\mathbf{g}$ and $\mathbf{A}^{Cu}$ matrices.

A typical powder EPR spectrum for an axially elongated copper complex as discussed in section 2.1.2 is shown in Figure 2-10a. The parameters chosen for the simulation of the spectrum are those for a copper-hexaquo complex with $g_{\|} > g_{\perp}$ and $A_{\|} > A_{\perp}$. Due to the amplitude modulation CW EPR spectra are usually recorded as first derivatives. In Figure 2-10b the corresponding absorption spectrum is shown. The spectrum is a superposition of four axial powder line shapes which can be assigned to the different m_I states. The 2D plot shows the contributions of the different m_I states as a function of the angle θ (defined in Figure 2-3 as the angle between the z-axis and the external magnetic field vector $\boldsymbol{B}_0$). In experimental spectra the splitting in the $g_{\perp}$ region is often not resolved due to large linewidths whereas the $g_{\|}$ and $A_{\|}$ values can usually be determined without difficulties.

The interactions of the electron spin with the weakly coupled I = 1/2 nuclei, described by $\mathcal{H}_N$ are usually not resolved in the CW EPR spectra and can only be investigated by applying pulse EPR. Due to the limited bandwidth of the MW pulses only a

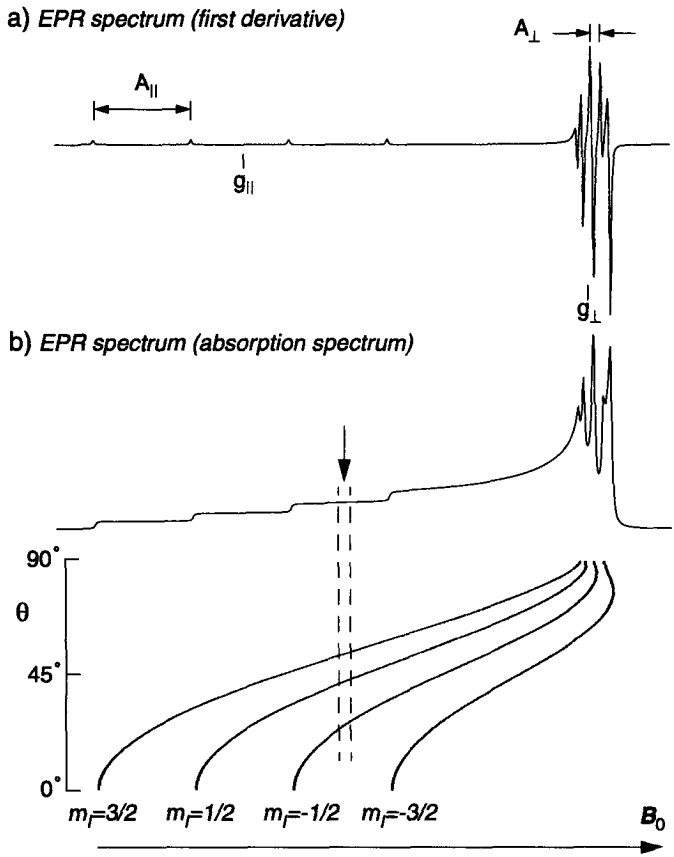

Fig. 2-10 (a) CW EPR spectrum for an axially elongated copper complex (first derivative); (b) same spectrum drawn as absorption spectrum with a 2D plot showing the different m_I transitions as a function of the angle θ.

small part of the EPR spectrum calculated from the Hamiltonian in Eq. (2.27) is excited. The dashed lines in Figure 2-10b indicate the excitation bandwidth (~50 MHz) for a pulse EPR experiment performed at the B_0 position indicated by the arrow. At a given B_0 position spin packets from different m_I states with different θ values can thus contribute to the spectrum. The pulse EPR spectra of the ^{13}C nuclei and protons can be calculated by treating the spin Hamiltonian as described in section 2.2.2 for the $S = 1/2$, $I = 1/2$ system. More accurate results are obtained by including the **g** anisotropy in the computation

[39,40]. Diagonalization of the EZI while neglecting the second term in Eq. (2.27) as the copper hyperfine interaction has no direct influence on the nuclear frequencies leads to the two nuclear Hamiltonians

$$\mathcal{H}_{\alpha,\beta} = \sum_i \left(-\frac{g_n \beta_n}{h} \boldsymbol{B}_0 \boldsymbol{I}_i + \langle S \rangle_{\alpha,\beta} \mathbf{A}_i' \boldsymbol{I}_i \right) \tag{2.28}$$

where the hyperfine interaction matrix $\mathbf{A}_i'$ is now expressed in the PAS of the EZI. Diagonalization of these Hamiltonians yields the nuclear frequencies as functions of the magnitudes and relative orientations of the magnetic field and the $\mathbf{g}$ and $\mathbf{A}_i'$ matrices [41]. Explicit expressions for the nuclear frequencies ν_α and ν_β for $I = 1/2$ nuclei including the $\mathbf{g}$ anisotropy are given in [42].

CHAPTER 3 *Methodology of EPR*

In the preceding chapter we have introduced the theoretical framework used for the interpretation of both CW and pulse EPR spectra. In this chapter we focus on the experimental aspects of CW and pulse EPR and introduce the different pulse EPR schemes used in this work.

3.1 CW and Pulse EPR

EPR spectra can be recorded in different frequency regions, the most important being S-band (2-4 GHz), X-band (8-10 GHz), Q-band (~35 GHz) and W-band (~90 GHz). The magnetic field strengths necessary to obtain the appropriate Zeeman splitting can be deduced from the resonance condition (Eq. (2.3)). Most of the applications in this thesis have been done at X-band frequencies, which corresponds to a magnetic field of approximately 320 mT at $g = 2$.

A typical X-band CW EPR spectrum of copper was already shown in Figure 2-9. CW EPR spectra are recorded by putting a sample into a MW irradiation field of constant frequency ν and sweeping the external magnetic field $\boldsymbol{B}_0$ until the resonance condition is fulfilled. In the experimental set-up the MW field is build up in a resonator (typically a rectangular cavity), into which the sample tube is introduced. The MW irradiation is pro-

vided by a klystron and transferred to the cavity through waveguides. The resonator is critically coupled which means that the incident power is completely absorbed by the resonator. Additional absorption by the sample during resonance leads to a detuning of the resonator and the reflection of MW power. The recording of this reflected MW power as a function of the magnetic field yields the CW EPR spectrum. Amplitude modulation of the magnetic field with a frequency of typically 100 kHz increases the signal-to-noise (S/N) ratio considerably and is responsible for the derivative shape of the spectra. The excitation bandwidth of the MW irradiation is very small (approximately 2 MHz) and the MW power is at maximum 200 mW. A more detailed treatment of the experimental aspects is found e.g. in [43].

In pulse EPR the spectrum is recorded by exciting a large frequency range simultaneously with a single high-power MW pulse of given frequency ν at a constant magnetic field $\boldsymbol{B}_0$. The relation between pulse length and excitation bandwidth is shown in Figure 3-1. The excitation profile of the pulse is obtained in the limits of the linear response the-

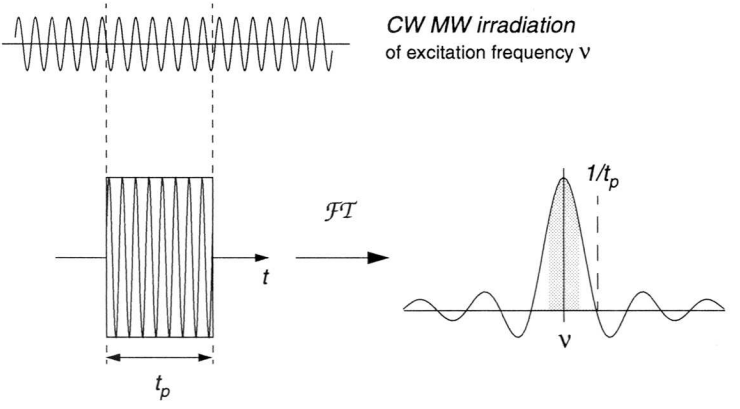

Fig. 3-1 The length of the MW pulse, obtained by amplifying a segment of the CW irradiation, determines the excitation bandwidth of the pulse. Homogeneous excitation is expected in the shaded area of width $1/t_p$.

ory by Fourier Transformation of the pulse shape[1]. This corresponds to a *sinc* function ($\frac{\sin x}{x}$) for a rectangular pulse where the first zero crossings of the sinc function away from the central frequency are given by $1/t_p$. Uniform excitation is considered to be given approximately in the shaded area delimited by $\nu \quad 1/2t_p$. An excitation bandwidth of 100 MHz is thus obtained for a 10 ns pulse, which corresponds to 3 mT at $g = 2$ as illustrated in Figure 2-9. Reduction of the pulse length leads to broader excitation range. Due to technical limitations it is, however, in most cases impossible to excite the whole spectrum by a single EPR pulse, which is a severe limitations as compared to CW EPR. The length of the pulse thus determines the selectivity of the excitation. The bandwidth of the resonator containing the sample is much larger than the one of the CW EPR cavity to allow for a rapid dissipation of the high power brought into the resonator by the MW pulse. Immediately after the MW pulse the sensitive detector must be protected from the high MW power in the resonator and signal recording is not possible. This so-called *deadtime* of the spectrometer depends on the bandwidth of the resonator and is in the range of 100 ns. By increasing the bandwidth of the resonator the dead time can be reduced. The large bandwidth of the pulse EPR resonator is however also responsible for the lower sensitivity as compared to CW EPR.

Most EPR applications still make use of continuous wave methods as the recording and interpretation of pulse EPR spectra requires sophisticated technical equipment and a more advanced theoretical background. A significant advantage of CW EPR with respect to the pulse methods is the higher sensitivity. A further limitation of pulse EPR are also the low measuring temperatures imposed by the short relaxation of the transverse magnetization involved in pulse experiments, especially for TM ions. CW EPR spectra on the other hand can be recorded at RT for a large number of spin systems, including radicals and TM ions. The additional information about weakly coupled nuclei and relaxation properties of the spin system that can be obtained by manipulating the spins with sequences of MW pulses explains however the efforts put into the development of new pulse methods (see e.g. [44,45]). The enhancement of forbidden transitions [46] or the establishing of correlations via 2D spectroscopy (see below) are examples for such

1. Under the excitation of MW pulses the electron spin systems shows a strongly non-linear behavior. The assumption of a linear response is only valid for weak excitation by soft pulses with nominal flip angles < 90°.

manipulations. Nevertheless CW and pulse EPR are complementary and only the application of both gives a reliable picture of the spin system. In this work pulse EPR is applied because of the high structural resolution in disordered systems, allowing for the determination of small coupling constants.

3.2 MW Pulses and Spin Dynamics

In this section we first introduce the concepts of *macroscopic magnetization* and *rotating frame* to describe the effects of MW pulses on a given spin system.

-The macroscopic magnetization $\boldsymbol{M}$ of a sample is obtained by adding up the contribution of all magnetic moments in a given sample volume. The precession of the magnetic moments about the external magnetic field $\boldsymbol{B}_0$ (taken along the z-axis) being out-of-phase in the absence of an external perturbation, the magnetic xy components are randomly distributed and a net magnetization (M_z) is observed only along $\boldsymbol{B}_0$ in the Boltzmann equilibrium.

- In the rotating frame the axes system rotates with the frequency ν_{MW} of the MW excitation about the z-axis. In this frame the excitation becomes time-independent and the resonances frequency for the electron spins is given by the offset $\Omega = \nu - \nu_{MW}$ of the true resonance frequency ν, obtained from the resonance condition in Eq. (2.3), from the excitation frequency ν_{MW}. The large static field $\boldsymbol{B}_0$ thus appears to be considerably reduced or even zero for the on-resonant case ($\nu = \nu_{MW}$).

It is the interaction of $\boldsymbol{M}$ with the applied electromagnetic fields and the detector which gives observable pulse EPR spectra. In Figure 3-2 the most simple pulse experiment, a single $\pi/2$ pulse, and the behavior of the magnetization under this pulse in the rotating frame are illustrated. The application of a MW pulse of frequency ν_{MW} leads to a magnetic field component $\boldsymbol{B}_1 \perp \boldsymbol{B}_0$ and the electron spins precess about the resultant of the static and the perturbing magnetic field during the pulse. Under the influence of a strong MW $\pi/2$ pulse applied along y the magnetization $\boldsymbol{M}$ is rotated to the x-axis[2]. This

2. The flip angle of a MW pulse (e.g. 90 ° for a $\pi/2$ pulse) depends on its length t_p and amplitude, the strength on the amplitude. The axis about which the magnetization vector is rotated is given by the phase of the pulse.

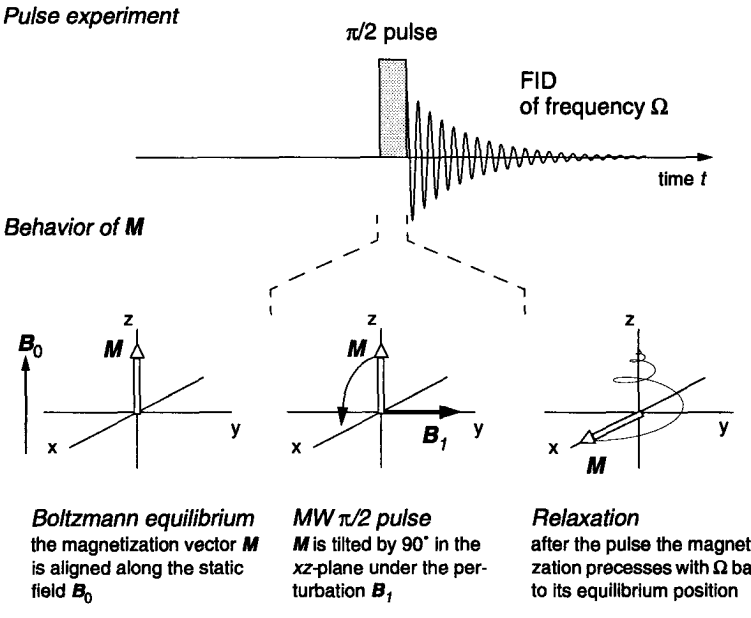

Fig. 3-2 Illustration of the simplest pulse experiment with a single MW $\pi/2$ pulse (top) and the behavior of the magnetization vector $\boldsymbol{M}$ in the rotating frame (bottom).

is shown for the on-resonant case in Figure 3-2, where the z-component of the resulting field is zero. After the MW pulse is switched off the magnetization vector moves back to its equilibrium position along z, thereby precessing with the offset frequency Ω . This behavior is called *relaxation* and will be discussed in the next paragraph. The precession leads to oscillating components M_x and M_y of the magnetization vector in the xy-plane which can be recorded as *free induction decay* (FID) after the MW pulse.

3.3 Relaxation Times and Linewidths

In this chapter we discuss the effects which bring the magnetization vector back to its equilibrium position. For this purpose we switch back to the microscopic view and consider again the single magnetic moments contributing to the overall magnetization. In an $S = 1/2$ system the spins can be oriented parallel or anti-parallel to the external magnetic field and a perturbation (e.g. pulse) induces transitions between the two energy lev-

els. The M_z magnetization in equilibrium is the result of a small surplus of spins parallel to their quantization axis. Changing the M_z magnetization involves reorientation of the microscopic magnetic moments. Transversal magnetization M_x and M_y on the other hand is given by an in-phase precession of the magnetic moments about the external field, induced e.g. by a MW pulse.

Upon relaxation the Boltzmann M_z magnetization is restored and the transversal magnetic components M_x and M_y vanish. These changes in magnetization are associated with the spin-lattice or longitudinal relaxation time T_1 and the spin-spin relaxation time T_2, respectively. The *spin-lattice relaxation* relates to the characteristic lifetime of the spin state and is determined by the dissipation of energy via the thermal vibration of the lattice. T_1 is related through the Heisenberg uncertainty principle, written in terms of energy and time ($\Delta w \Delta t \geq h/2\pi$), to the *linewidth* of an individual spin packet. A small T_1, taken as a measure for Δt, leads to a smearing out of the energy levels (large Δw) and thus a broad resonance line. Large T_1 values are usually found for systems with isolated electronic ground states, well separated from the lowest excited states. The *spin-spin relaxation* is concerned with the mutual spin flips caused by dipolar and exchange interactions between the assembly of spin in the sample. T_2 is usually much shorter than T_1 and thus the dominant contribution to the linewidth. The two contributions are often summarized by relating the resultant linewidth of a single spin packet to a relaxation time T_2' given by

$$\frac{1}{T_2'} = \frac{1}{T_2} + \frac{1}{2T_1}. \tag{3.1}$$

T_2' is the relaxation time which is of importance in connection with the transverse magnetization generated and observed in pulse EPR experiments. T_2' is temperature dependent and determines the *homogeneous linewidth* of a single spin packet. For transition metal complexes T_2' values in the range of several μs are common at liquid helium temperatures. Among the various effects influencing T_2' we only mention high spin concentrations or clustering of paramagnetic molecules which may lead to a considerable shortening of the relaxation time.

3.4 Pulse EPR Experiments

The importance of spin echo experiments in pulse EPR is explained by the broad lines encountered in solid-state EPR which make the recording of FID's often impossible. Due to the short relaxation times of transition metal ions pulse EPR experiments have to be recorded at liquid helium temperatures in most cases and anisotropic interactions like the **g** matrix or $\boldsymbol{B}_0$ inhomogeneities lead to an *inhomogeneous* broadening of the EPR line. As illustrated in Figure 2-3 an inhomogeneously broadened line is obtained by the contribution of many spin packets, subject to slightly differing static magnetic fields. Unlike the homogeneous linewidth, the inhomogeneous linewidth is not related to any relaxation time.

3.4.1 Two-Pulse ESEEM

An important effect of the inhomogeneous broadening is, however, the rapid decay of the FID, obtained after the excitation of an EPR line by a $\pi/2$ pulse. All spin packets contributing the magnetization vector have now slightly different precession frequencies Ω. The dephasing of the magnetic moments under the action of the magnetic field distribution leads to a rapid vanishing of the transversal magnetization, which often occurs already during the spectrometer deadtime. In the most simple spin echo experiment, the two-pulse ESEEM experiment, the dephasing of the magnetic moments is reversed by a second pulse of double length. Applied after a time interval τ this pulse flips the magnetic moments by 180° in the *xy*-plane. As the order of the spins, precessing with different velocities, is also reversed the in-phase magnetization is restored at time τ after the second pulse, leading to an observable spin echo (primary echo). This is illustrated in Figure 3-3 where the pulse sequence of the experiment is shown together with the behavior of the magnetization vectors. Both pulses are applied along *-x*. The spectrometer deadtime (~ 100 ns) is indicated as striped area after the first pulse. The pulse lengths are typically in the range of several tenths of ns while τ is incremented from ~ 100 ns to several µs, in steps of 10 or 20 ns.

Echo envelope modulation. The FID itself does not contain much information for a system with large inhomogeneous broadening. The importance of this ESEEM methods stems from the fact that due to the coupling of the electron spins to nearby nuclei the

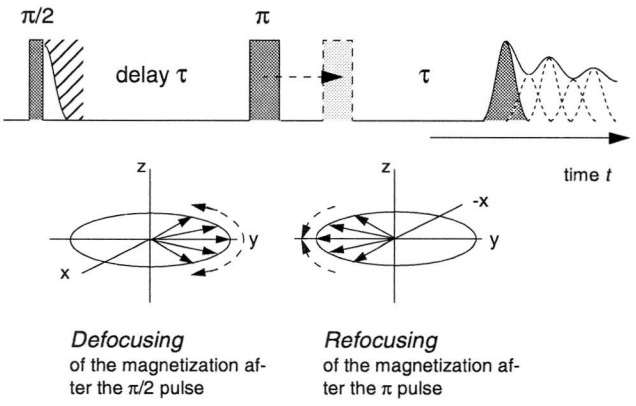

Fig. 3-3 Illustration of the two-pulse ESEEM sequence (top) and behavior of the individual spin packets during the evolution time τ (bottom). The dephasing leading to the decay of the FID within the spectrometer deadtime (indicated by the striped area after the first pulse along) during the first time period is reversed by the π pulse. At the time 2τ after the first pulse a spin echo is observed. Incrementation of the time τ yields the echo envelope modulation due to the coupling to the nuclear spins.

amplitude of the electron spin echo depends on the time interval τ between the two pulses. If the echo intensity is recorded as a function of τ a modulation pattern results. For an $S = 1/2$, $I = 1/2$ system it contains the nuclear frequencies ν_α and ν_β as well as combination lines ν_+ (sum combination frequency) and ν_- (difference combination frequency). The basic theory of this modulation effect was given by Rowan et al. [39]. In Appendix B the two-pulse ESEEM modulation formula is given for a $S = 1/2$, $I = 1/2$ system. The echo envelope decay is characterized by the phase-memory time T_M, identical to the relaxation time T_2' in the absence of effects like spectral diffusion which lead to a faster decay. For N nuclei coupled to an unpaired electron the overall echo envelope modulation pattern is given by the product of the N individual modulation patterns [30]

$$E^{mod}(\tau) = \prod_{i=1}^{N} E_i^{mod}(\tau). \tag{3.2}$$

This property of the modulation pattern can be used to eliminate unwanted modulations by division of time traces (cf. chapter 5).

For anisotropic systems with broad basic frequencies ν_α and ν_β the decay of the modulation can be much faster than the decay of the envelope itself. The truncation of the modulation pattern by the spectrometer deadtime (the first points of the echo envelope can not be recorded as the spin echo then refocuses in the deadtime of the second pulse) leads to severe distortions of the spectra. In these cases analysis of the narrow sum peak may be of advantage.

3.4.2 Three-Pulse ESEEM

The three-pulse ESEEM experiment was first introduced by Mims [30]. Although it is not extensively used in the application section we want to discuss it here in detail as other important pulse sequences like Mims ENDOR and HYSCORE are based on this experiment. The three-pulse sequence is shown in Figure 3-4. It consists of three $\pi/2$ pulses separated by the fixed delay time τ (typically several hundreds of ns) and the variable time t_1. The first two pulses create electron polarization along the z-axis ($-M_z$ for the on-resonant spin packets) as well as nuclear coherence. The nuclear coherence is allowed to evolve during the evolution period t_1. The third MW pulse converts the electron polarization and nuclear coherence to observable electron coherence which manifests itself as an stimulated electron spin echo at the time τ after the last pulse. The amplitude of this echo depends on the evolution time t_1. Recording of the echo amplitude as a function of t_1 while keeping τ constant yields a modulation pattern similar to the two-pulse ESEEM modulation. In Appendix B the analytical formula of the three pulse ESEEM modulation is given for an $S = 1/2$, $I = 1/2$ system.

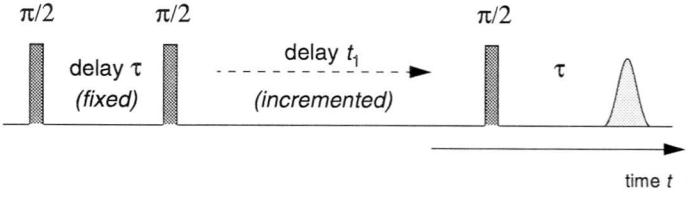

Fig. 3-4 Three-pulse ESEEM sequence with three $\pi/2$ pulses separated by the time intervals τ (fixed) and t_1 (incremented). The stimulated echo is observed at time τ after the third MW pulse.

The main differences between the two formulae are the absence of combination lines in the three-pulse ESEEM, the shallower modulation depth (k/2 vs. k/8) and the occurrence of *blind spots* due to the amplitude factors $[1-\cos(2\pi\nu_\alpha\tau)]$ and $[1-\cos(2\pi\nu_\beta\tau)]$ for the frequencies ν_β and ν_α, respectively. For $\tau = \frac{n}{\nu_{\alpha/\beta}}$ with $n = 0$, 1, 2,... these factors become zero and the corresponding basic frequencies do not contribute to the modulation. Furthermore, as the magnetization is stored as electron polarization during the evolution time t_1, the echo envelope decays with T_1 as compared to the T_M decay in the two-pulse experiment. The stimulated echo can therefor in general be observed for much longer times than the primary echo (t_1 intervals of several tenths of μs).

The choice of the time intervals in the three-pulse ESEEM experiment is also limited by the spectrometer deadtime. The shortest value for the variables τ and $(\tau+t_1)$ is given by the deadtime after the third $\pi/2$ pulse. The modulation pattern can in principle be recorded from $t_1 = 0$ on. This requires however extensive phase cycling to get rid of the artifacts[3] produced by undesired two-pulse spin echoes due to the non-ideality of the $\pi/2$ pulses [47].

3.4.3 1D Four-Pulse ESEEM

As we have seen in the preceding chapter, both two- and three- pulse ESEEM are affected by the spectrometer deadtime and the first points of the modulation pattern can therefore not be recorded. Considerable information may be lost especially in the case of broad lines with rapidly decaying time signals. It has already been demonstrated in chapter 2 that the sum peak obtained in two-pulse ESEEM is a narrow line, also for anisotropic systems. In this section an experiment based on the three-pulse ESEEM sequence is described, which yields narrow combination lines and has furthermore the benefit of an T_1 decay of the echo envelope. This is the one-dimensional version of the four-pulse ESEEM experiment. The two-dimensional version (HYSCORE) is described in the next

3. As an example for such an artifact consider the two-pulse echo generated by the second and third pulse at the time t_1 after the third pulse. Upon increasing t_1 this primary echo will overlap the stimulated echo if t_1 equals τ and gives a peak in the modulation pattern. This artifact can be eliminated by subtracting two time traces with the phases 0 and π for the first $\pi/2$ pulse. The phase of the stimulated echo is inverted by these procedure while the primary echo is not affected and the primary echo will be eliminated by the subtraction.

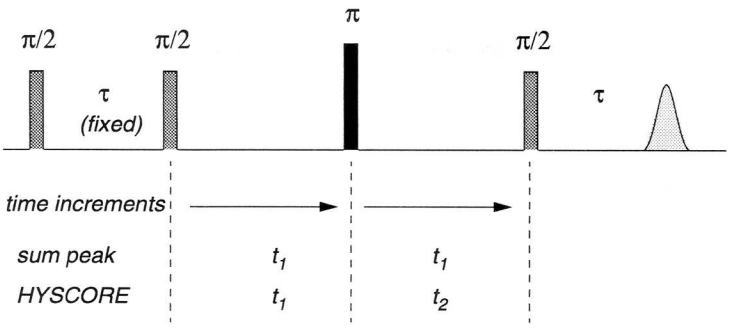

Fig. 3-5 Four-pulse ESEEM sequence with the time increments for the one-dimensional sum peak experiment and the two-dimensional HYSCORE.

section.

The pulse sequence of the four-pulse ESEEM is shown in Figure 3-5. The three-pulse sequence is extended by inserting a strong π pulse between the second and the third π/2 pulse. The nuclear coherence created by the first two pulses and evolving during the first time period t_1 is transferred between the two m_S states of the electron by this pulse. The local magnetic fields experienced by the nuclei thus change and the inhomogeneous HFI is refocused during the second evolution period after the π pulse. At time $2t_1$ a *nuclear coherence transfer echo* is formed which is detected as an amplitude modulation of the stimulated electron spin echo formed at time τ after the third π/2 pulse [48].

The analytical formula for the four-pulse experiment was derived by Gemperle et al. [47] and is given in its corrected form [37] in Appendix B. The sum peak modulation ($\nu_\alpha + \nu_\beta)t_1$ is obtained from the contribution E_{IIIa} by setting $t_1 = t_2$. The amplitude factor $C_c(\tau)$ leads to the same blind-spot behavior as in the three-pulse experiment.

3.4.4 HYSCORE

The two-dimensional version of the four-pulse ESEEM experiment was first introduced by Höfer et al. [49]. HYSCORE stands for *hyperfine sublevel correlation spectroscopy*, reflecting the transfer of nuclear coherence by the π pulse between the m_S manifolds. In the HYSCORE experiment the two time intervals t_1 and t_2 are incremented independently (see Figure 3-5). Fourier Transformation of the two time-domains yields a

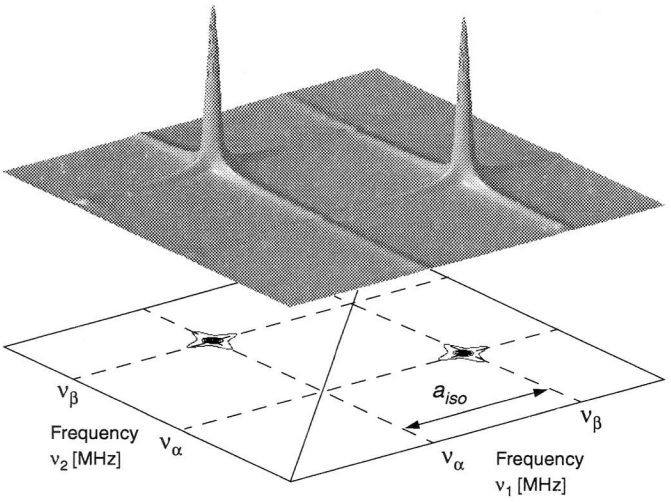

Fig. 3-6 Simulated HYSCORE spectra for a weakly coupled, isotropic $S = 1/2$, $I = 1/2$ system, showing the cross-peaks between the nuclear frequencies ν_α and ν_β. The exact location of the peaks and the coupling can be determined from the projection onto the (ν_1,ν_2)-plane.

two-dimensional spectrum with the frequency axes ν_1 and ν_2.

In Figure 3-6 HYSCORE spectra for a weakly coupled $S = 1/2$, $I = 1/2$ system are shown.The evolution of the nuclear coherence in the two time intervals t_1 and t_2 with different frequencies ν_α and ν_β (cf. term E_{IIIa} in Appendix B) yields cross-peaks at the frequencies (ν_α, ν_β) and (ν_β, ν_α) in the 2D spectrum. This peaks are placed symmetrically about the diagonal $(\nu_1 = \nu_2)$, indicated by a solid line in Figure 3-6. If the transfer between the two m_S manifolds is not complete (π pulse not strong enough) additional peaks (ν_α, ν_α) and (ν_β, ν_β) will be observed on the diagonal. The 1D ESEEM spectrum is obtained by projection of the 2D spectrum on ν_1 or ν_2.

HYSCORE has a few major advantages as compared to the other ESEEM methods: the expansion into a second dimension simplifies the interpretation of complicated spectra considerably as cross-peaks can only be observed between frequencies of the same nucleus. Furthermore HYSCORE is particularly useful for the investigation of anisotropically broadened ESEEM lines due to the refocusing action of the π pulse. As the nuclear frequencies are observed as coherence transfer echoes the ESEEM lines are free

from dead-time distortions. Weak and strong coupling is easily distinguished due to the positive and negative phase factors in the relevant terms E_{IIIa} and E_{IIIb}, respectively. For strong coupling, peaks will be observed in the $(\nu_1, -\nu_2)$ quadrant, well separated from the weak coupling features in the (ν_1, ν_2) quadrant [48,50].

In *disordered* systems the broad ESEEM lines will appear as correlation ridges. From the positions and shapes of these ridges information can be extracted about magnitude and orthorhombicity of the coupling [42,51-53]. In Figure 3-7 a typical HYSCORE spectrum for a weakly coupled $S = 1/2$, $I = 1/2$ system with isotropic g and axial HFI is shown. The dipolar coupling leads to a curvature of the ridges away from the anti-diagonal ($\nu_1 = 2\nu_I - \nu_2$). The maximum shift $\Delta\nu_{max}$ from the anti-diagonal, observed for $\theta \sim 45°$, is related to the dipolar coupling constant T by [42]

$$\Delta\nu_{max} = \sqrt{2}\left(\frac{9}{16}\frac{T^2}{\nu_I}\right) = \sqrt{2}\Delta_{max}\,. \tag{3.3}$$

The isotropic coupling can be estimated from the separation of the ridges as indicated in the figure. The end points of the ridges which correspond to the canonical orientations $\theta = 0, 90°$ are found on the anti-diagonal. Due to their weak intensity they are however often difficult to observe.

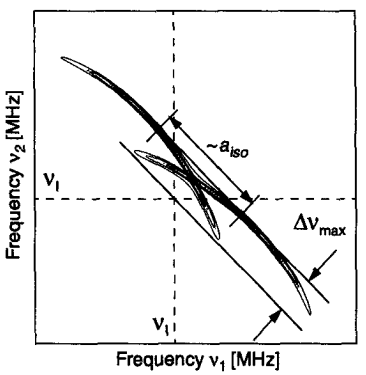

Fig. 3-7 HYSCORE spectrum for a weakly coupled, disordered $S = 1/2$, $I = 1/2$ system with anisotropic, axial HFI. The dashed lines indicate the nuclear Zeeman frequencies on the two frequency axes.

3.4.5 ENDOR

In the ESEEM experiments discussed so far the applied MW pulses act on the electron spins whereas the nuclear spins are excited indirectly via the anisotropic HFI. No ESEEM effect is thus observed for isotropic systems or paramagnetic species in solution where the anisotropy is averaged out by molecular motion.

The ENDOR (Electron Nuclear Double Resonance) techniques use both MW and radio-frequency (RF) pulses for the manipulation of electron and nuclear spins, respectively [54]. Many ENDOR experiments are based on the two pulse sequences introduced by Mims [55] and Davies [56], shown in Figure 3-8. In both schemes, the electron spin echo amplitude is measured as a function of the variable RF frequency. All time intervals are fixed. The RF pulse induces spin flips of the nuclei if it covers the frequency range of the nuclear transition. (cf. hollow arrows in the two m_S manifolds in Figure 2-6). Nuclear transitions lead to changes in the electron polarization which are observed via the electron spin echo. As the excitation range of the RF pulse is small (< 1 MHz) the whole NMR spectrum has to be recorded by sweeping the RF frequency through the spectrum.

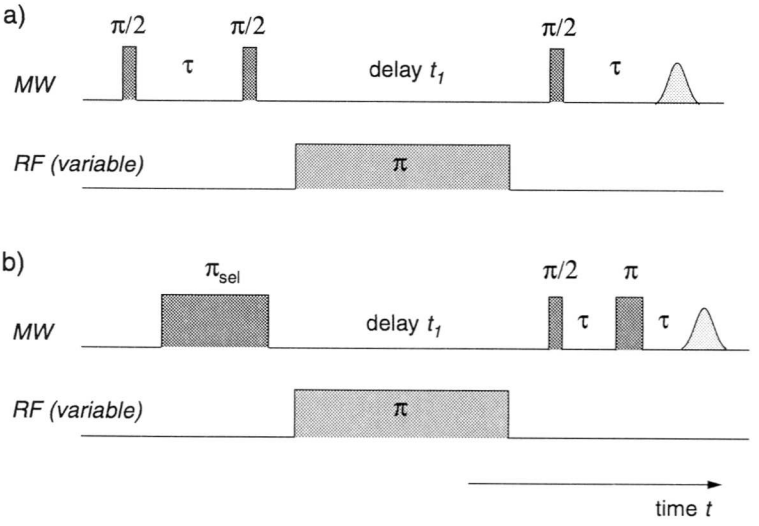

Fig. 3-8 Illustration of the Mims (a) and Davies (b) ENDOR pulse sequences. All time delays are fixed. The electron spin echo amplitude is recorded as a function of the variable RF frequency.

Recently methods have emerged to increase the effective bandwidth of the RF pulses (e.g. [57]).

Only Mims ENDOR spectra are presented in this thesis. The method is based on the three-pulse experiment and is subject to a similar blind-spot behavior than the ESEEM experiment. Blind spots occur in the spectrum if the following relation is fulfilled between the HFI a of a nucleus and the time delay τ:

$$\tau = \frac{n}{a}, \qquad \text{with } n = 0, 1, 2,... \tag{3.4}$$

This blind-spot behavior can be partially eliminated by addition of several spectra, recorded with different τ values.

Finally it should be noted that the effective flip angle of the RF pulse for a given nucleus depends on the nuclear g_n-factor. This can be a considerable drawback for the investigation of nuclei like ^{13}C as much stronger RF fields or longer pulses are needed to observe an ENDOR effect. Strength and length of the RF pulses are subject to technical and practical limitations (e.g. T_1 relaxation time). If the coupling is large enough (e.g. strongly coupled nitrogen nuclei) this effect is partially counterbalanced by the *hyperfine enhancement* which originates from a modulation of the internal magnetic field, produced by the electron at the nucleus, with the RF frequency [54]. The addition of external RF and internal fields leads to an increase of the ENDOR effect.

CHAPTER 4 *Aqueous Chemistry of Cu^{2+} and Carbonates*

In the first part of this chapter the chemical protagonists of this thesis are introduced. The coordination chemistry of copper is reviewed as well as the aqueous chemistry of carbon dioxide and the geochemistry of solid calcium carbonates. Furthermore the interaction between trace metal ions and calcium carbonate minerals is discussed again with focus on Cu^{2+}. This compilation is the basis for the discussion of the experimental results in chapters 5 and 6.

In the second part chemical equilibria or speciation calculations for the various systems under investigation are presented. The expected distributions of complexes in solution and at the surface, calculated from the thermodynamic stability constants, are used as starting points for the preparation of samples for the experimental studies. The predictions of the speciation calculations are compared to the spectroscopic results in chapters 5 and 6 and discrepancies are discussed.

4.1 Cu^{2+} and Carbon Dioxide

4.1.1 Coordination Chemistry of Cu^{2+}

The Cu^{2+} configuration is the most stable valence state of copper in water and the coordination chemistry of Cu^{2+} shows a great diversity. The most frequently observed coordination group consists of four coplanar ligands with one or two distant axial ligands completing a distorted tetragonal pyramid or distorted octahedron [24]. The six water molecules in the first coordination sphere of the copper-hexaaquo complex $Cu(H_2O)_6^{2+}$ show a (4+2) coordination, the axial bonds being about 12% longer than the equatorial, indicating a stronger bonding of the equatorial ligands. Typical distances for the equatorial and axial Cu-O bonds are 2.0 Å and 2.2 Å, respectively.

The reason for the distortion of the coordination sphere is the stabilization of the electronic $3d^9$ configuration through the Jahn-Teller effect [21]. Elongation of the axial bonds leads to a lowering of the energy of the metal d-orbitals pointing along the z-axis (d_{z2}, d_{xz} and d_{yz}) as shown in the energy level scheme in Figure 2-4 on page 15.

For symmetrical complexes with identical ligands there may be several stable configurations producing the same lowering in overall energy. In this case a rapid interconversion between the different distortion axes can occur resulting in a *dynamic* Jahn-Teller effect. This is the case for the $Cu(H_2O)_6^{2+}$ complex in solution. External factors such as phase transitions or H-bonding in the second coordination sphere may result in the stabilization of one configuration and induce a static distortion of the complex. Such complexes with measurable bond-length differences are subject to a *static* Jahn-Teller effect.

For chelating ligands the coordination geometry is fixed by the ligand geometry which limits the possibilities for stabilization of the complex by distortion. This point is clearly illustrated by the formation constants of copper-ethylenediamine (en) complexes $[Cu(en)_x(H_2O)_{6-2x}]^{2+}$ [21]. K_1 and K_2 for $x = 1,2$ are much higher than K_3 since in the first two cases the coordination takes place in the equatorial plane, thus allowing for a distortion through displacement of the axial water molecules. Formation of the $x = 3$ complexes requires coordination of two (en) molecules both at equatorial and axial positions making a Jahn-Teller distortion difficult.

In solution copper has a pronounced tendency to form dimeric and polymeric complexes in the presence of bridging ligands such as OH^-, carbonate or carboxylic acids. The dimeric salts as well as the solution complexes of the later compounds have been widely investigated because of their interesting magnetic behavior (e.g. [58]).

4.1.2 Carbon Dioxide

Although the atmospheric reservoir of carbon dioxide (CO_2) is rather small, the gas is of primary importance in a number of geochemical and biochemical processes such as sedimentation and photosynthesis [1,3]. A major part of CO_2 is buried in the hydrosphere in large deposits of calcium carbonate ($CaCO_3$), mainly calcite. Such deposits are produced through sedimentation in freshwater and marine environments with high biological productivity.

Dissolution of CO_2 in water leads to the formation of the diprotic carbonic acid (H_2CO_3). Carbonic acid can undergo dissociation to form bicarbonate (HCO_3^-) and carbonate (CO_3^{2-}) ions. The constants that govern these equilibria are tabulated in Appendix C and the pH dependent distribution of the three species is illustrated in chapter 4.3. The acidity constant given for carbonic acid is the so called composite acidity constant for the species $H_2CO_3^* = CO_2(aq) + H_2CO_3$. This formulation takes into account that at 25 °C only about 0.3% of the dissolved CO_2 is present as carbonic acid, able to undergo dissociation.

Extensive work has been done on the coordination behavior of carbonate ligands [12,13]. The occurrence of mono- and bidentate coordination has been confirmed by IR spectroscopy through investigation of the C-O chromophores and by X-Ray structure determination. Detailed studies of cobalt-carbonate complexes [59] have given insight into complexation mechanisms such as ring closure and substitution effects.

4.1.3 Complexation of Cu^{2+} by Carbonate Ligands

The complexation between Cu^{2+} and carbonate ligands is known to show a large diversity in the liquid and solid phase. For a number of copper-carbonate complexes like $CuHCO_3^+$, $CuCO_3^0$ or $Cu(CO_3)_2^{2-}$, complexation constants have been determined and tabulated [13,60]. At high pH values mixed hydroxocarbonates are expected to form and

precipitate from solution. The most important solid copper-carbonate compounds are the minerals malachite ($Cu_2CO_3(OH)_2$) and azurite ($Cu_3(OH)_2(CO_3)_2$) [61]. The salt $CuCO_3$ is not stable at ambient temperature under atmospheric conditions. These compounds as well as oxysalts like $Na_2Cu(CO_3)_2 \cdot 3\ H_2O$ and $Na_2Cu(CO_3)_2$ provide examples for the different coordination structures with carbonate ions. The carbonate ion can act as monodentate or bidentate ligand, bridging metal atoms to form finite complexes, chains, layers or 3D framework structures [24].

4.2 The Solid Calcium Carbonates

4.2.1 Structural Characteristics

Carbonate rocks represent about one-sixth of the global sedimentary mass. Of the rock-forming carbonates, calcite $CaCO_3$ and dolomite $CaMg(CO_3)_2$ account for more than 90% and are mostly of maritime origin. In nature three polymorphs of calcium carbonate are found: calcite, aragonite and vaterite. Calcite is the most abundant polymorph as it is the thermodynamic stable phase at ordinary conditions. Aragonite is stabilized by high pressures and is precipitated in presence of Mg^{2+} (e.g. in seawater). It is also found in the skeletal parts of certain organisms. Vaterite has only marginal importance e.g. as repair tissue of fractured cells of certain organisms. It frequently occurs however as a product of artificial precipitation. Some authors speculated that the mineral may well be a more common component of lake precipitates as supersaturation with respect to calcium carbonate is a frequent occurrence in natural waters [62,63]. In aqueous solutions vaterite undergoes recrystallization to calcite within 24 hours.

In the following we only discuss the structures of calcite and vaterite, the relevant calcium carbonates in this work [64,65]. The rhombohedral calcite structure can be visualized as alternating planes of CO_3^{2-} and Ca^{2+} ions, perpendicular to the *c*-axis. Two of the carbonate planes are depicted in Figure 4-1. The CO_3 group is the fundamental unit of all carbonates with a mean <(OCO) angle of 120° and a mean C-O distance of 1.28 Å. The Ca^{2+} ion in calcite is 6-coordinated, forming a slightly distorted octahedron (cf. Figure 4-1) with a Ca^{2+}-O distance of 2.38 Å. A variety of divalent cations such as Mg^{2+}, Mn^{2+}, Fe^{2+}, Cd^{2+}, Zn^{2+} or Co^{2+} are known to form calcite-type carbonates with struc-

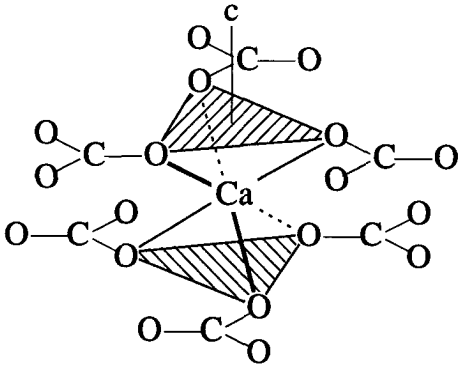

Fig. 4-1 Schematic drawing of the coordination sphere of a calcium ion in calcite with two carbonate planes indicated by the shaded area perpendicular to the *c*-axis.

tural variations due to the differences in ionic radii of the metals.

The hexagonal structure of vaterite is more complicated and less well established. Unlike in calcite the carbonate ions are oriented parallel to the *c* axis. The Ca^{2+} ions are surrounded in a first coordination sphere by 6 oxygens in an octahedral fashion with a Ca^{2+}-O distance of 2.59 Å. In a second coordination sphere the Ca^{2+} ions are either surrounded by 6 oxygens at 3.05 Å forming an intermediate between an elongated octahedron and a trigonal prism or by 6 oxygens at 3.55 Å forming an almost regular octahedron. This leaves two sets of Ca^{2+} ions with a molar ratio of 2:1, respectively. The vaterite structure is loosely packed which explains the higher solubility (K_{so} = 7.9) as compared to calcite (K_{so} = 8.48) and the lower density 2.54 g/cm^3 (vs. 2.71 g/cm^3 for calcite) [3].

The morphologies for the two polymorphs are also quite different as can be seen in Figure 4-2. Calcite often forms large rhombohedral crystals whereas the spherulitic vaterite particles are aggregates of a large number of small crystallites < 50 nm [63]. The crystal morphologies are responsible for the differences in specific surface areas which are typically a few m^2/g for calcite compared to up to 30 m^2/g for vaterite [66,67].

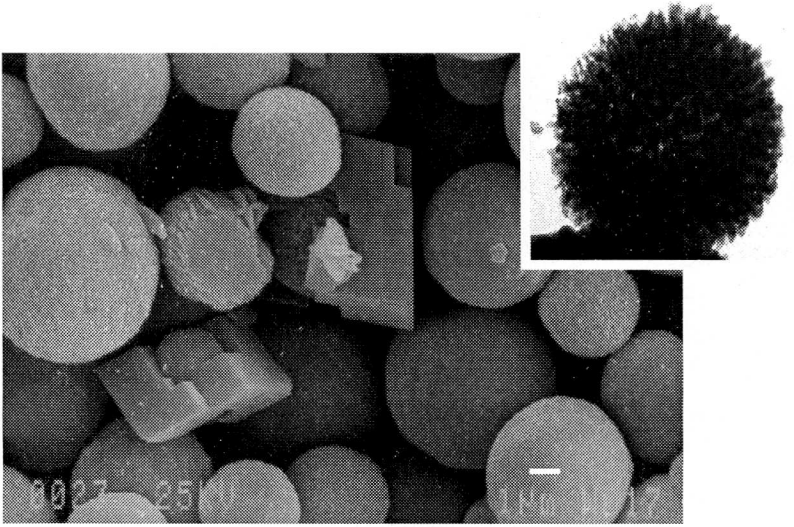

Fig. 4-2 SEM image of a vaterite sample prepared by precipitation from a supersaturated solution. The vaterite spherulites are aggregates of small crystals of variable shapes. This is more clearly shown in the TEM image (inset). Some particles are intergrown with calcite crystals of rhombohedral shape. The white scale bar at the bottom of the SEM image corresponds to 1 μm. (Foto Prof. Giovanoli, Univ. Bern)

4.2.2 Crystal Growth and Dissolution

Carbonate minerals are among the most reactive minerals at the earth surface. Due to their abundance they often control composition and chemical properties of natural waters. The dissolution and precipitation kinetics of calcite have been the subject of numerous investigations (see e.g. [68-70] and references therein). Three different reaction mechanisms have been identified:

$$CaCO_3(s) + H^+ \underset{k_{-1}}{\overset{k_1}{\rightleftharpoons}} Ca^{2+} + HCO_3^- \tag{4.1}$$

$$CaCO_3(s) + H_2CO_3^* \underset{k_{-2}}{\overset{k_2}{\rightleftharpoons}} Ca^{2+} + 2\,HCO_3^- \tag{4.2}$$

$$CaCO_3(s) \underset{k_{-3}}{\overset{k_3}{\rightleftharpoons}} Ca^{2+} + CO_3^{2-} \tag{4.3}$$

The dissolution at high degrees of undersaturation is described in terms of the fol-

lowing rate law with contributions from the three forward reactions

$$R_f = k_1 a_{H^+} + k_2 a_{H_2CO_3^*} + k_3, \tag{4.4}$$

where R_f is the dissolution rate far from equilibrium [mol·m^{-2}·s^{-1}], k_i are first order rate constants and a_i activities of the dissolved species. The first term in Eq. (4.4) is effective at low pH (< 5), the second term at high pCO_2 (> 0.1 atm) and high pH (> 6) and the third term at low pCO_2 (< 0.1 atm) and high pH (> 7). Close to saturation or at supersaturation calcite is precipitated from solution and the overall backward reaction rate is described in terms of the individual reaction steps

$$R_b = k_{-1} a_{Ca^{2+}} a_{HCO_3^-} + k_{-2} a_{Ca^{2+}} a^2_{HCO_3^-} + k_{-3} a_{Ca^{2+}} a_{CO_3^{2-}} \tag{4.5}$$

where k_{-i} are second and third order rate constants. Inskeep et al. [69] have speculated that the last reaction in Eq. (4.5) involves the formation of a surface activated complex by Ca^{2+}, CO_3^{2-} and $CaCO_3$(s) with an activation energy due to the dehydration of the ions. The same idea was forwarded by Brown et al. [71] who explained the precipitation of calcite in terms of the surface reaction/molecule integration mechanism of Chiang et al. [72].

More insight into the mechanisms of calcite dissolution and precipitation is given by the detailed kinetic expressions of Arakaki et al. [73] who combined the surface complexation model of Van Cappellen et al. [6] (section 4.3.2) with the mechanistic models presented above. In this approach the macroscopically observed reaction rates are linked to the distribution and reactivity of chemical species at the calcite surface. The existence of hydration sites >CO_3H and >CaOH at the calcite surface, formed by the reaction with H_2O and CO_2 both in air and in water was shown experimentally with surface-sensitive spectroscopic techniques by Stipp et al. [16]. Arakaki et al. [73] also stress the importance of dissolved $CaCO_3^0$ species as 'precipitation agents'.

The dissolution and precipitation kinetics of vaterite as well as the transformation into calcite have been investigated by Kralj et al. [63,74,75]. These authors noticed a great similarity between their results an the dissolution and growth kinetics of calcite, the main difference following directly from the different solubilities.

The kinetic studies mentioned so far do not take into account the microtopography of the carbonate surface. Close to saturation precipitation and dissolution of material occurs at activated surface sites such as steps and kinks [2]. At higher supersaturation additional growth nuclei may form directly on the surface which are then starting points for new crystal layers. This processes have been visualized with AFM [15,76] and other spectroscopic techniques [77]. The AFM pictures have also revealed the highly dynamic nature of the calcite surface. Some authors [15,16] have concluded that the calcite-water interface is ordered and crystalline and that no evidence is found for a disordered or amorphous hydrated surface layer, a few monolayers in depth, as postulated by Davis et al. [78].

4.2.3 Interactions with Trace Metal Ions

So far we have only considered the reactivity of pure calcium carbonate. In the presence of impurities this reactivity can be considerably altered. Here we limit the discussion to the effects of trace metal ions.

The interaction of trace metal ions such as Cd^{2+}, Mn^{2+}, Zn^{2+}, Co^{2+} and Ni^{2+} with calcium carbonate has been the subject of a large number of investigations (see e.g. [7,79-81]). Most metal ions show a rather high affinity for the carbonate surface and often uptake of the metal ion is observed upon precipitation or recrystallization of calcium carbonate. This so called coprecipitation reaction proceeds in most cases via rapid initial adsorption, followed by surface precipitation and formation of a $MeCO_3(s)$-$CaCO_3(s)$ solid-solution. Depending on the molar ratio Ca^{2+}:Me^{2+} the precipitation of a separate $MeCO_3(s)$ phase on the calcium carbonate may occur.

It is unclear whether adsorption occurs via exchange with Ca^{2+} in exposed (structural) lattice sites or by complexation to carbonate groups at the solid-water interface. Following the concept of McBride [8], Zachara et al. [81] determined equilibrium constants of the surface-exchange reaction:

$$Ca(surface) + Me^{2+}(aq) = Me(surface) + Ca^{2+}(aq). \quad (4.6)$$

Strong adsorption is observed for metal ions with ionic radii smaller than Ca^{2+} that

form a solid carbonate with calcite structure (e.g. Cd^{2+}, Mn^{2+}, Zn^{2+} - see above). Metal ions with higher hydration energies like Zn^{2+}, Co^{2+} and Ni^{2+} are more easily desorbed than Cd^{2+} and Mn^{2+} which show limited sorption reversibility [81].

The application of high-resolution, surface-sensitive spectroscopic and microscopic techniques has also provided atomic-scale structural information about sorption and coprecipitation processes of trace metals on calcium carbonate minerals. Pingitore et al. [82] used X-ray absorption spectroscopies (XAS) to demonstrate the substitution of Ca^{2+} by Sr^{2+} at lattice structural sites. Based on XPS, LEED and Auger electron spectroscopy (AES) data Stipp et al. [17] concluded that solid-state diffusion is an important mechanism for the uptake of Cd^{2+} by calcite. In their XPS study of the Co^{2+} sorption at the calcite-water interface Xu et al. [83] observed rapid incorporation of the Co^{2+} ions by the dynamic calcite surface; they excluded, however, solid-state diffusion as relevant metal uptake mechanism. The synchrotron X-ray standing wave (XSW) and X-ray reflectivity analysis of Sturchio et al. [84] revealed that a large fraction of adsorbed Pb^{2+} ions occurs primarily in the surface atomic layer of calcite where they replace the Ca^{2+} ions. Paquette et al. [77] and Reeder [85] showed however that for the interaction of trace metals with calcite surfaces not only the properties of the metals but also the geometry of the active sites on the calcite surface are of importance which leads e.g. to compositional differences for crystal sectors grown from crystallographically nonequivalent faces.

Several authors have investigated the interaction of Cu^{2+} with calcium carbonates. Franklin et al. [10] found that the sorption reaction is complete within minutes. Papadopoulos et al. [86] explained the adsorption of Cu^{2+} on calcite in terms of surface-solid solution $Cu_xCa_{1-x}CO_3$, in accordance with the results of Franklin et al. [10]. Compton et al. [80] found a high affinity of Cu^{2+} for the calcite surface and also a strong inhibition of the calcite dissolution by Cu^{2+} ions. Strong inhibition of the calcite precipitation and dissolution is also observed for the metal ions Fe^{2+} and Zn^{2+}, weaker inhibition for Mg^{2+} [87]. Nassrallah-Aboukaïs et al. [66,67], finally, have investigated the transformation of vaterite to calcite by EPR through the interaction of Cu^{2+} with the carbonates. They concluded that Cu^{2+} ions are incorporated as clusters in the calcite bulk at low concentrations. At high Cu^{2+} concentrations they found inhibition of the vaterite dissolution and observed mixtures of vaterite, calcite, aragonite and malachite.

4.3 Chemical Equilibrium Calculations

4.3.1 ChemEQL

The speciation of Cu^{2+} with hydroxyl and carbonate ions in aqueous solution and at the calcium carbonate surface was calculated using the chemical speciation program ChemEQL [25]. The stability constants of the complexes used in the calculations were taken from the literature [13,60]. In the following a short description of the program and of the setup of the EXCEL input matrix is given.

For the computation the chemical equations are expressed as formation of species from a minimum number of components, e.g. Cu^{2+}, CO_3^{2-} and H^+ for the copper-carbonate complexes in solution. The formalism and the equilibrium constants are documented in Appendix C.1. The mass action expressions are then written according to these equations and the species expressed as products of the involved components and the corresponding K values. This is illustrated in Eq. (4.7) for the $CuHCO_3^+$ complex.

$$[CuHCO_3^+] = [Cu^{2+}]^{\mathbf{1}} \cdot [CO_3^{2-}]^{\mathbf{1}} \cdot [H^+]^{\mathbf{1}} \cdot K_{11} \tag{4.7}$$

A matrix is set up with the stoichiometric coefficients (bold exponents in Eq. (4.7)) where the species form the lines and the components the columns. The formation constants are added in an additional column. The total or free concentrations of the components are added at the end of the columns. The matrix is finally written in an EXCEL sheet. All matrices used for the speciation calculations presented below are given in Appendix C.2.

From these input data the concentration of the species are calculated iteratively following the Newton-Raphson method. The species concentrations obtained from a first guess of component concentrations are compared to the total concentrations of the components. From the errors of the material balance equation an improved guess for the concentration of the components is derived which is then used for a refined computation of the species concentrations. This procedure is repeated until the iteration criteria are fulfilled. For more details see e.g. [88].

4.3.2 Surface Complexation Model

In the surface complexation model [6,26] adsorption or, more precisely, chemisorption is described as chemical bonding between dissolved species and lattice-bound ions exposed at the mineral surface. In the case of $CaCO_3$ these surface ions are written as $>Ca^+$ and $>CO_3^-$. Compared to the lattice ions, the exposed surface ions have free coordination sites. In the presence of water primary hydrated species $>CaOH^0$ and $>CO_3H^0$ are formed by adsorption and dissociation of water. Spectroscopic evidence has been given for the formation of hydrated sites on the carbonate surface in water [16]. These sites can undergo protonation and deprotonation reactions. Furthermore coordination of anionic and cationic solution species can take place at the corresponding surface sites. The chemical equilibria for the surface species are listed in Appendix C.1/TableC3.

The intrinsic stability constants K_{int} for surface complexes can not be determined experimentally and the values given in Appendix C.1 are rough estimates taken from [6], obtained by comparison with the solution equilibria and fitting to surface charge data. These values are independent of surface coverage and surface charge. In practice, surface equilibria have therefore to be described with conditional formation constants K_c, which account for the non-ideal behavior of the surface species due to the coulombic interaction with an average surface potential. Intrinsic and conditional formation constants are related through

$$K_c = K_{int} \cdot e^{\frac{-zF\Psi}{RT}} \tag{4.8}$$

where z is formally equal to the charge of the surface complex, Ψ is the surface potential (V), and F is Faraday's constant (96'485 C/mol).

For the definition of the surface potential Ψ the simplest electric double layer (EDL) model, the so-called constant capacitance model, is used [1]

$$\Psi = \frac{\rho}{\kappa} \tag{4.9}$$

where ρ is the surface charge (C/m^2). The EDL capacitance κ (F/m^2) depends on the

ionic strength I and a constant α, related to the dielectric properties of the EDL:

$$\kappa = \frac{\sqrt{I}}{\alpha} \tag{4.10}$$

For the computation of the surface equilibria with ChemEQL the primary surface species and the electrostatic term, formally treated as a concentration, are added as components to the stochiometric matrix (cf. Appendix C). Concentrations of surface species are calculated from a number of experimental parameters which are added at the end of the matrix. These parameters are the specific surface area (in m^2/g), the number of active surface sites (in mol/g), and the concentration of the solid (in g/l). Ionic strength and capacitance finally allow for the calculation of the surface potential.

4.3.3 The CO_2/H_2O system

For the presentation of the results obtained with ChemEQL we start out with a simple example: the CO_2/H_2O system. In Figure 4-3 the pH dependent carbonate equilibria for a closed system (no exchange with the atmospheric CO_2) with a total carbonate concentration $c_T = 0.05$ M are illustrated. In this representation which will be used throughout the chapter the activities of the different species are drawn on a logarithmic scale

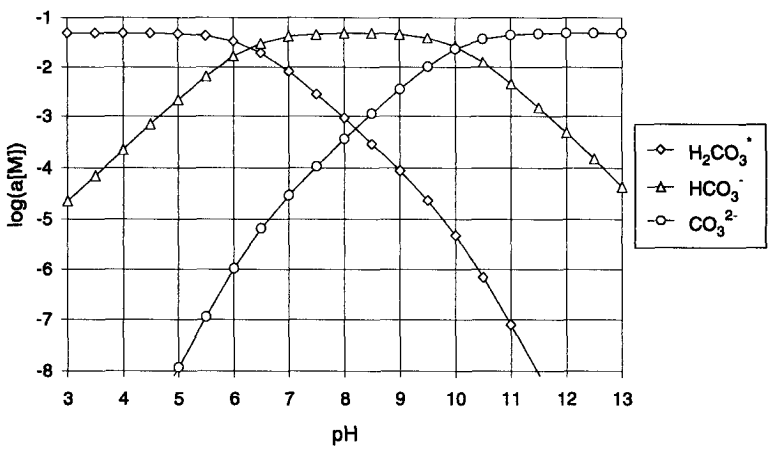

Fig. 4-3 pH dependent carbonate equilibria in H_2O in a closed system with a total carbonate concentration $c_T = 0.05$ M.

against the pH.

With increasing pH the carbonic acid $H_2CO_3^*$, defined here as the sum of $CO_2(aq)$ with H_2CO_3, is deprotonated. Equal activities for the species $H_2CO_3^*/HCO_3^-$ and HCO_3^-/CO_3^{2-} are found at pH ≡ 6.3 (~pK_1) and 10.1 (~pK_2), respectively. The linear or quadratic depedence of the species activities on the proton activity is reflected in the slopes of the curves between the pK values.

4.3.4 The Cu^{2+}/H_2O system

In the absence of other ligands and neglecting the possible formation of a solid phase the hydrated Cu^{2+} ion is the dominant species in water at pH < 7. This is shown in Figure 4-4 for a total copper concentration $Cu_T = 5 \cdot 10^{-4}$ M. At pH > 9 the coordinated water molecules are stepwise deprotonated leading to the formation of the hydroxo species $Cu(OH)_2^0$, $Cu(OH)_3^-$, etc. In the pH range 7 to 9 the appearance of the $Cu_2(OH)_2^{2+}$ complex illustrates the pronounced tendency of Cu^{2+} to form clusters in the presence of bridging ligands. The dimeric complexes are less dominant at lower Cu^{2+} concentrations (see also [89]).

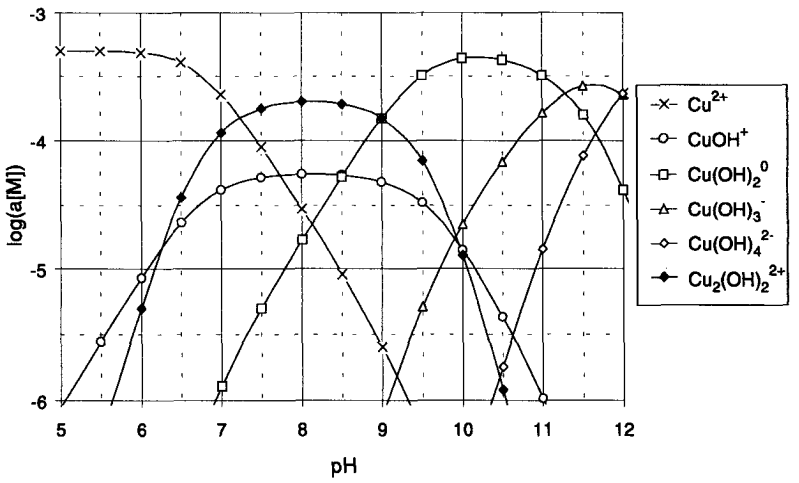

Fig. 4-4 Copper-hydroxo species in the Cu^{2+}/H_2O system as a function of pH for a total copper concentration $Cu_T = 5 \cdot 10^{-4}$ M.

4.3.5 The $Cu^{2+}/CO_2/H_2O$ system

In Figure 4-5 the copper speciation in the presence of carbonate ligands in a closed, aqueous system is shown. The total copper concentration Cu_T is again $5 \cdot 10^{-4}$ M and the total carbonate concentration 0.05 M. An ionic strength I = 1 M is assumed to account for the effect of the glass forming agent (cf chapter 5) which considerably influences the activities of the charged species.

The dominant species in this system are the hydrated $Cu(H_2O)_6^{2+}$ ion at pH < 5.7 and the bidentate carbonate complexes $CuCO_3^0$ and $Cu(CO_3)_2^{2-}$ at pH > 5.7. Hydroxo species are not relevant in the considered pH range. However, the system is unstable with respect to the mixed hydroxocarbonate malachite $Cu_2CO_3(OH)_2$(s) (and the oxide tenorite CuO(s) at higher pH) due to considerable supersaturation. The solubility of malachite as a function of pH is obtained by rewriting equation *16* of Appendix C.1:

$$\log[Cu^{2+}] = -2.9 - pH - \frac{1}{2}\log[CO_3^{2-}] \qquad (4.11)$$

This function is drawn as a diffuse line in Figure 4-5. Malachite is expected to pre-

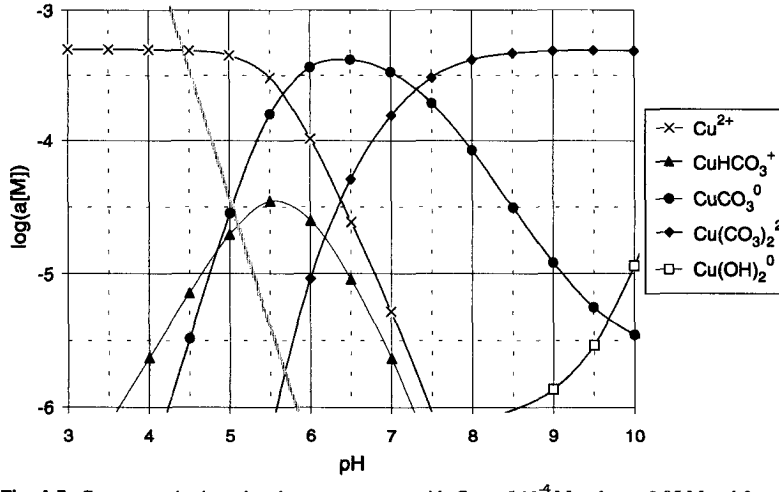

Fig. 4-5 Copper species in a closed aqueous system with $Cu_T = 5 \cdot 10^{-4}$ M and c_T = 0.05 M and for a ionic strength I = 1 M. The diffuse line indicates the solubility of malachite as a function of pH according to Eq. (4.11).

cipitate at pH > 4.5. Experimentally one finds, however, that the copper-carbonate complexes are stable for several hours at high carbonate concentrations indicating a kinetic inhibition of the malachite precipitation.

Samples for the EPR measurements were prepared at pH 5.5, 6.5 and 8. A maximum concentration of the assumed monodentate $CuHCO_3^+$ complex is expected at pH 5.5 with $Cu(H_2O)_6^{2+}$ and $CuCO_3^0$ as dominant species, however. At pH 6.5 $CuCO_3^0$ and at pH 8 $Cu(CO_3)_2^{2-}$ should dominate. Copper-hydroxo species amount only to about 2% at pH 8. The distribution of the complexes in % of the total copper concentration Cu_T is given in Table 4-1.

Table 4-1 Concentration of copper-carbonate complexes in solution at different pH (given in % of total copper concentration $Cu_T = 5 \cdot 10^{-4}$ M) as calculated with ChemEQL [25] for an ionic strength I = 1 M at 25 °C.

	$Cu(H_2O)_6^{2+}$	$CuHCO_3^+$	$CuCO_3^0$	$Cu(CO_3)_2^{2-}$
pH 5.5	60	7	33	~0
pH 6.5	5	2	83	10
pH 8	~0	~0	17	81

4.3.6 The $CaCO_3(s)/Cu^{2+}/H_2O$ system

In this chapter two situations for the $CaCO_3(s)/Cu^{2+}/H_2O$ system are presented in analogy to the experimental studies in chapter 6. In the first case the carbonates vaterite (^{13}C-labeled) and calcite are mixed with pure water and the total carbonate concentration in solution is given by the pH dependent dissolution of the solid phase ($c_T^0 = 0$ M). In the second case the solid carbonate is added to a solution with a given total (^{13}C-labeled) carbonate concentration $c_T^0 = 0.05$ M. In a third part of the chapter a surface complexation constant for copper is derived which renders a better agreement between the calculations and the experimental results.

For the computation of the surface complex concentrations the differences in ionic strength resulting from the different carbonate concentrations have to be considered. The ionic strength is not fixed experimentally by addition of an inert salt to avoid the problems with background signals discussed in chapter 5 for the glass forming agents. In both

cases the ionic strengths are estimated from the concentrations of the solution species in the pH range 8 to 10 and an average value is taken for the surface speciation calculation. The small amounts of counter-ions K^+ and NO_3^- from base and acid added to the solution to adjust pH are neglected. For the $^{13}c_T^0 = 0.05$ M system one equivalent of K^+ ions from the base used to prepare the carbonate solution is included in the ionic strength estimation, however. Samples for the EPR measurements were prepared at pH 8.5 and 9 since high pH values are typical for natural waters in contact with carbonate minerals [1].

Calculations for $c_T^0 = 0$ M:

The parameters used for the calculations were either determined experimentally or taken from the literature: surface area: 30 m^2/g [64]; density of surface sites: $2.5 \cdot 10^{-4}$ mol/g. This value is calculated from the density of Ca^{2+} lattice sites exposed on a (10$\bar{1}$4) cleavage plane of calcite (5 sites/nm^2, [6]); concentration of solid: 26 g/l; capacitance: 9 F/m^2. The capacitance is calculated according to Eq. (4.10) with an ionic strength value $I = 0.003$ M and $\alpha = 0.006$ $m^2(M)^{1/2}/F$. The same α value was used by Van Cappellen et al. [6] for rodochrosite and calcite to obtain the high capacitance typical for the solid carbonate-aqueous solution interface.

In Figure 4-6 the pH dependent activities of the calcium and carbonate solution species (a) as well as the different copper complexes for a closed system with $Cu_T = 5 \cdot 10^{-5}$ M (b) are shown. The same *x*- and *y*-scales are used in all representations to allow for a better comparison. The activity of the $CaCO_3^0$ complex is constant as it is given through direct equilibrium with the solid phase vaterite. At lower pH the carbonate is protonated and the activities of the Ca^{2+} and HCO_3^- ions increase in solution. The dominant copper species are the $CuCO_3^0$ complex up to pH 9. With decreasing carbonate concentration at higher pH hydroxides (represented here by $Cu(OH)_2^0$) become the dominant species.

At the vaterite surface the dominant species are $>CaOH_2^+$ and $>CO_3^-$. The complexes formed by the calcium and carbonate surface ions are shown in Figure 4-7 (a) and (b), respectively. The charges of these complexes are, however, counterbalanced by high concentrations of $>CaCO_3^-$ and $>CO_3Ca^+$ complexes as the low capacitance does not allow for the build-up of a large surface potential. The concentration of these species exceeds the solution concentrations of Ca^{2+} and CO_3^{2-} ions. From Figures 4-6 and 4-7 and it can be seen that the copper surface complexes are of minor importance.

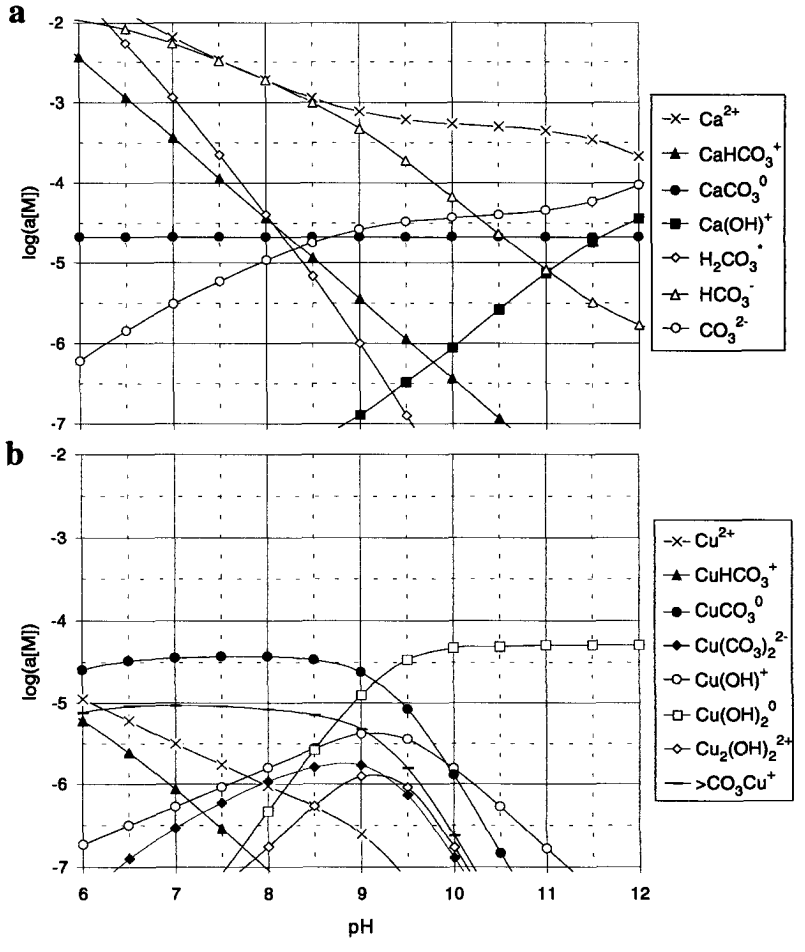

Fig. 4-6 Solution species for the closed $CaCO_3(s)/Cu^{2+}/H_2O$ system with $Cu_T = 5 \cdot 10^{-5}$ M and $c_T^0 = 0$ M. (a) Calcium and carbonate species given by pH dependent dissolution of the solid vaterite phase; (b) copper species in solution and at the vaterite surface.

The pH dependent distribution of solution and surface complexes was also calculated for the calcite experiment in chapter 6 with the following parameters: surface area: 1 m^2/g; density of surface sites: $8.3 \cdot 10^{-6}$ mol/g; concentration of solid: 45 g/l; total copper and carbonate concentrations $Cu_T = 1.4 \cdot 10^{-6}$ M and $c_T^0 = 0$ M, respectively. Capacitance and ionic strength are the same as in the vaterite experiment. The results of the

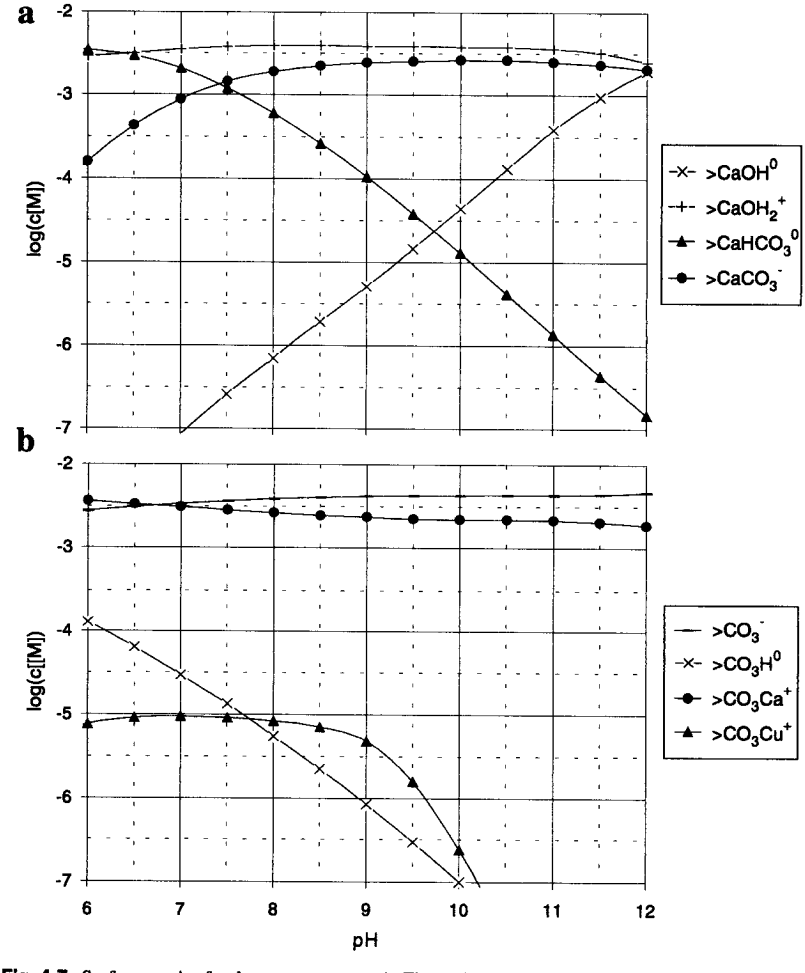

Fig. 4-7 Surface species for the same system as in Figure 4-6. (a) complexes formed by the calcium surface ions; (b) complexes formed by the carbonate surface ions including the copper complex.

calculations are very similar to those shown in Figures 4-6 and 4-7 except for the smaller concentrations of the surface and copper species and are, therefore, not given explicitely.

Calculations for $c_T^0 = 0.05$ M:

The parameters used for the calculations of the surface speciation with a total carbonate concentration $c_T^0 = 0.05$ M are the same as above except for the ionic strength $I = 0.05$ M resulting in a capacitance $\kappa = 37$ F/m^2. The activities of the carbonate ions in solution are now analogous to those shown in Figure 4-3. As a result the free Ca^{2+} concentration, determined by the solubility product of vaterite, is reduced. The distribution of the copper species is similar to the one in Figure 4-5 with a major contribution of the $Cu(CO_3)_2^{2-}$ complex at pH 9. The situation for the calcium and carbonate surface complexes is illustrated in Figure 4-8. Due to the high carbonate concentration the $>CaCO_3^-$ complex dominates at pH > 8 (Figure 4-8a) while the $>CO_3Ca^+$ concentration is considerably reduced. The large capacitance allows for higher potentials at the vaterite surface. The concentration of copper surface complexes is again small. In the pH range 7 to 9 it is further diminished by the strong copper-carbonate complexation in solution. This situation is analogous to the one found by Zachara et al. for the interaction between Co^{2+} and calcite [81]. These authors explained the unexpected decrease of adsorbed Co^{2+} at pH >9 by the formation of $Co(CO_3)_2^{2-}$ species in solution.

Calculations with a modified surface complexation constant for Cu^{2+}:

The surface complexation constant for Cu^{2+} is derived from the corresponding equilibrium in solution, in analogy to the treatment of Van Cappellen et al. [6]. The two equations are given below:

$$H_2CO_3 + Cu^{2+} = \mathbf{CuHCO_3^+} + H^+ \tag{4.12}$$

$$>CO_3H^0 + Cu^{2+} = \mathbf{>CO_3Cu^+} + H^+ \tag{4.13}$$

The formation constant of the $CuHCO_3^+$ species in Eq. (4.12) is given by

$$K_{CuHCO_3^+} = \frac{[\boldsymbol{CuHCO_3^+}][H^+]}{[H_2CO_3][Cu^{2+}]} = \frac{[\boldsymbol{CuHCO_3^+}]}{[HCO_3^-][Cu^{2+}]} \cdot \frac{[HCO_3^-][H^+]}{[H_2CO_3]}$$

$$= 10^{1.8} \cdot 10^{-3.8} = 10^{-2} \tag{4.14}$$

The constant is calculated with the pK value of the true carbonic acid H_2CO_3 (Van Cappellen et al. compared the acidity constant of the $>CO_3H^0$ sites to the microscopic

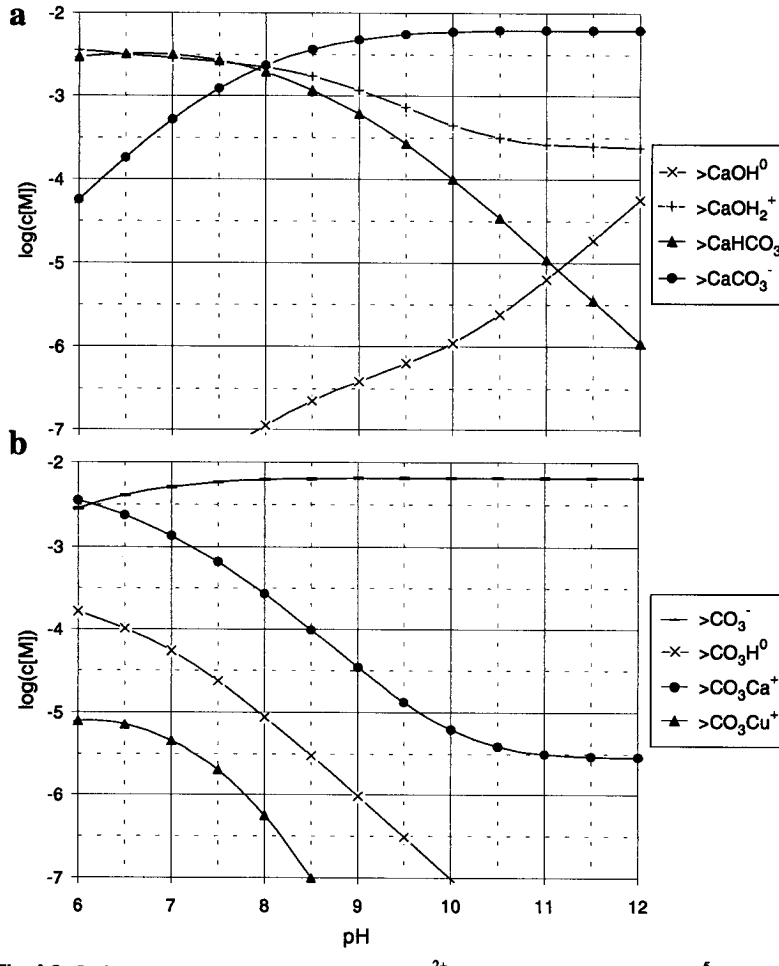

Fig. 4-8 Surface species for the closed $CaCO_3(s)/Cu^{2+}/H_2O$ system with $Cu_T = 5 \cdot 10^{-5}$ M and $c_T^0 = 0.05$ M. (a) Complexes formed by the calcium surface ions; (b) complexes formed by the carbonate surface ions including the copper complex.

constant of carbonic acid, $\log(K_{H_2CO_3}/2) = -4.1$).

If we take $K = 10^{-2}$ from Eq. (4.14) as a starting point for the equilibrium constant of Eq. (4.13) we find that the copper surface complexes are of minor importance in the distribution of the copper species. This is in contradiction to the experimental results which show strong surface bonding in the pH range 8.5 to 9, independent of the total carbonate

concentration. The EPR results indicate that the Cu^{2+} ions are bound to 3 or 4 carbonate groups at the vaterite/calcite surface.

The complexation of a Cu^{2+} ion with n identical ligands L^- can be described by the overall complexation reaction

$$Cu^{2+} + n\,L^- = Cu(L)_n^{2-n} \qquad \text{with } K_{tot} = \frac{[Cu(L)_n^{2-n}]}{[Cu^{2+}][L^-]^n} \tag{4.15}$$

The overall complexation constant K_{tot} is the product of the equilibrium constants β_n of the individual complexation steps. The first step for the monodentate bicarbonate ligand corresponds to reaction *12* in Appendix C and thus $\log(\beta_1) = 1.8$. Generally the binding strength decreases with higher values of n, e.g. due to sterical constraints, which is reflected in lower β_n values. If we assume a decrease of 20% for β_n from the n to the $(n+1)$ complexation step, in analogy to the situation observed for copper-amino complexes [90], we end up with $K_{tot} = 5.3$ for four bicarbonate ligands. The corresponding surface complexation constant derived from Eq. (4.14) is then $\log(K_{>CO_3Cu^+}) = 1.5$[1].

Figure 4-9 shows the distribution of the copper-carbonate surface complexes and the major copper solution species, calculated with the overall complexation constant $\log(K_{>CO_3Cu^+}) = 1.5$, for the vaterite system with $c_T^0 = 0.05$ M (to be compared with Figure 4-8). With this equilibrium constant the copper surface complexes now appear as the dominant species in the pH range 8 to 9. At higher pH the surface complex is rivaled by the carbonate solution complex $Cu(CO_3)_2^{2-}$ as found for Co^{2+} by Zachara et al. [81]. For the $c_T^0 = 0$ M system this carbonate species is not observed due to the low CO_3^{2-} activity in solution and the surface complex is rivaled by the hydroxo-complex $Cu(OH)_2^0$ at pH 9.5.

Although the speciation calculations are now in better agreement with the experimental results it is important to note that a carbonate layer at the calcium carbonate surface should also affect the surface complexation constants of the Ca^{2+} and CO_3^{2-} ions.

1. In this derivation the n carbonate ligands are considered to be statistically independent which is not the case for surface ions or carbonate ligands in a surface layer. The surface complexation constant given above is thus a lower limit as it does not include possible chelate effects.

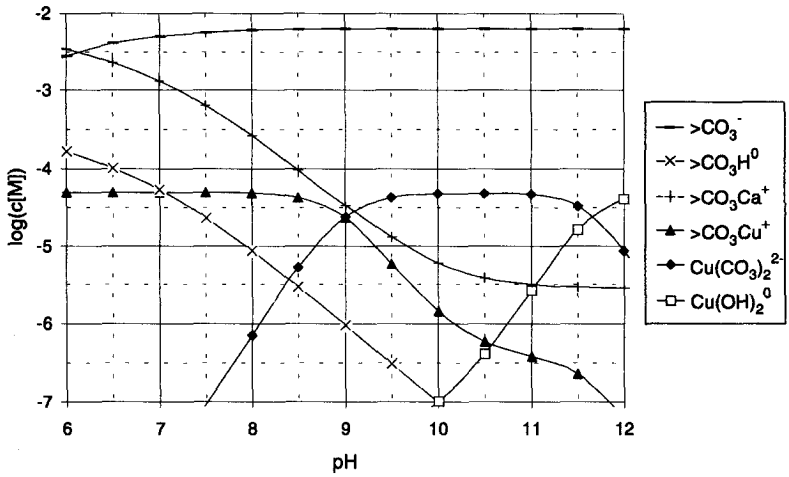

Fig. 4-9 Carbonate surface complexes for the closed $CaCO_3(s)/Cu^{2+}/H_2O$ system with $Cu_T = 5 \cdot 10^{-5}$ M and $c_T^0 = 0.05$ M, including the major copper solution species.

The reduced fractional sorption observed for all metal ions by Zachara et al. [81] at pH < 8 is not found for Cu^{2+} in our calculations. As the sorption of the foreign metal ions to calcite is governed by Eq. (4.6) the data of Zachara et al. can only be reproduced by assuming a stronger surface complexation for Ca^{2+} than in our model. With our limited sorption data it is not possible to reevaluate all the complexation constants of the Van Cappellen model. Spectroscopic evidence presented in chapter 6 indicates that for the description of the metal ion coordination to the calcite surface complexation constants should be used which take into account the complexation to several carbonate surface ligands.

CHAPTER 5

Copper Carbonate Complexes in Aqueous Solution.

5.1 Introduction

In this chapter the results of the first part of this study, the investigation of the complexation of Cu^{2+} with ^{13}C-labeled carbonate ions in aqueous solution at different pH, are presented (cf. [91]). The electronic and geometric structures of the complexes are deduced from the interactions between the unpaired electron of the Cu^{2+} ion and the magnetic moments of ^{13}C and proton nuclei in the first coordination sphere of the metal ion. The pH dependent substitution of water molecules by carbonate ligands can thus be followed. The interpretation is based on the hyperfine couplings of the axial and equatorial water protons in the $Cu(H_2O)_6^{2+}$ complex as determined in a single crystal CW ENDOR study [92]. The results are compared to the concentrations of mono- and bidentate copper-carbonate complexes in solution at different pH obtained from the speciation calculations in section 4.3.5. The experience and the results gathered in this study allows for a straightforward interpretation of the EPR spectra obtained for the surface complexes in chapter 6.

The ^{13}C interactions were determined with two-pulse ESEEM and ENDOR techniques. Two-pulse ESEEM proved particularly useful for the investigation of a large ^{13}C coupling in the matching range whereas ENDOR allowed the observation of smaller

interactions with broad basic frequencies. The proton signals of the equatorial and axial water molecules were observed with 1D and 2D four-pulse ESEEM techniques, where the contributions are well separated due to the differences in the magnitude of the couplings.

5.2 Experimental Section

5.2.1 Sample Preparation

For the preparation of the ^{13}C-labeled carbonate solution, $Ba^{13}CO_3$ (Sigma, 98% enriched) was suspended in water in a closed glass vessel connected through a teflon tube to a second vessel filled with N_2-saturated distilled water. $Ba^{13}CO_3$ was slowly dissolved by adding concentrated HCl and $^{13}CO_2$ degasing from the solution was trapped in the second vessel by addition of KOH. The $^{13}CO_2$ gas not trapped in this procedure was collected in a balloon following the second vessel and bubbled through the aqueous phase until the pH remained constant. The carbonate concentration was determined by titration with KOH and back-titration with $BaCO_3$. Approximately 70% of $^{13}CO_2$ were recovered with this procedure.

An aliquot of 10 ml of the ^{13}C-labeled carbonate solution with a total carbonate concentration of $c_T = 0.06 \pm 0.01$ M was transferred to a closed glass vessel equipped with a pH electrode. $NaNO_3$ was added to obtain an ionic strength of 1.5 M. The pH of the solution was adjusted to 6.5 with 1 M HNO_3 and 0.5 ml of a 10^{-2} M $Cu(NO_3)_2$ solution was added, resulting in a total Cu^{2+} concentration $Cu_T = 5 \cdot 10^{-4}$ M. After five minutes of stirring, the pH was lowered to 5.5. Degasing of CO_2 resulted in the build-up of pressure in the vessel. With a gas volume of ~1 ml in the closed vessel a loss of approximately 13% of carbonate from the solution was estimated at pH 5.5. This loss was smaller than the titration error of the total carbonate concentration and therefore considered to be negligible. Furthermore the degassed CO_2 partially redissolved in the solution at higher pH. A sample was taken after five minutes of stirring and the pH was raised to 6.5 and 8 with 1 M KOH. After each pH adjustment the solution was stirred for five minutes and another sample was taken. At pH 8 precipitation of blue-green material was observed after several hours as the solution was highly supersaturated with respect to malachite

($Cu_2CO_3(OH)_2$). The samples, which did not show any visible precipitation, were immediately transferred to EPR sample tubes and frozen in liquid N_2. The copper-hexaaquo sample was prepared by adjusting the ionic strength of a $5 \cdot 10^{-4}$ M $Cu(NO_3)_2$ solution to 1.5 M with $NaNO_3$.

Two series of samples with and without ^{13}C-labeled CO_2 were prepared under identical conditions to eliminate the strong sodium and nitrogen signals from $NaNO_3$ that occur in the pulse EPR spectra in the same frequency range as the ^{13}C signals (see below). The addition of $NaNO_3$ to the sample solution is required to promote glass formation upon freezing although it makes the pulse EPR measurements more tedious and influences the complexation equilibria (lower *K*-values).

5.2.2 Glass Forming Additives

The maximum density at 4 °C and the high melting and boiling temperatures of water are due to the tetrahedral structure and the dipolar character of the H_2O molecule allowing for strong inter-molecular hydrogen bonding. As a result the crystalline structure of ice is not completely broken upon melting and large clusters (up to 130 molecules) with pseudo-crystalline structure are present also in liquid water [24].

The cluster formation can lead to an aggregation of solutes into separate phases. This is especially true for the Cu^{2+} with its pronounced tendency to form bridged complexes with OH^- or polydentate ligands. Upon freezing this effect is greatly enhanced due to the difficulty to include foreign ions in the ice structure. The temperature dependence of the relaxation time T_2' requires temperatures below 20 K for structural investigation of the copper carbonate complexes by pulse EPR. The concentration of paramagnetic copper ions in separate phases upon freezing on the other hand leads to strong electron-electron dipolar interactions and thus fast dipolar relaxation, making pulse EPR experiments impossible.

It is well known that the formation of large crystalline solvent phases can be prevented by the addition of a glass forming agent to the sample such as alcohols or inert salts [93]. The lowering of the diffusion rate due to the higher viscosity of the additive or the lower melting points of the resulting eutectic mixtures lead to an inhibition or slow down of ice crystal nucleation and growth. As a result homogeneous disordered phases

of non-crystalline glass are formed upon freezing.

However one has to be aware that glass forming agents like ethanol or the polydentate glycerol can coordinate to transition metal ions. They severely disturb the formation of weak complexes with ligands like the monodentate carbonate ion. The choice of a suitable glass forming agent was a major problem in this study. Alcohols and other organic solvents either inhibited the weak bicarbonate complexation, decreased the solubility of CO_2 or lead to the precipitation of solid carbonate phases. The best results were obtained with inert salts. After an evaluation of different possibilities a $NaNO_3$ concentration of 1.5 M was used. The problems caused by the magnetic moment of the Na and ^{14}N nuclei were already mentioned.

5.2.3 Equipment

The UV/Vis spectra were measured at room temperature with a Perkin Elmer Lambda 6 spectrophotometer between 200 and 900 nm with a scan speed of 300 nm/min. In addition to the copper-carbonate samples, reference spectra of pure water, of 1.5 M $NaNO_3$ solution and 0.1 M $KHCO_3$ solution were recorded to allow for base-line correction of the copper-carbonate spectra and to exclude interference of the copper spectra with the CO_3^{2-} and NO_3^- chromophores (< 350 nm). At pH 5.5 base-line distortions were observed due to bubbling of CO_2.

Cw EPR spectra were recorded on a Bruker ESP 300 spectrometer equipped with a liquid nitrogen cryostat. Solution spectra at room temperature spectra were measured at a microwave (MW) frequency of 9.776 GHz using a flat cell. Frozen solution spectra were measured at 130 K and 9.483 GHz with a MW power of 5 mW, a modulation amplitude of 0.5 mT and a modulation frequency of 100 kHz. The magnetic field and the MW frequency were measured with a Bruker NMR Gaussmeter ER 035M and a HP 5248M electronic frequency counter, respectively. The accuracy was checked with a N,N-diphenylpicrylhydrazyl (DPPH) reference.

Two-pulse ESEEM and ENDOR experiments were carried out with a home-built X-band pulse EPR spectrometer [94]. The four-pulse ESEEM traces were recorded on a BRUKER ESP 380E spectrometer and a home-built S-band pulse EPR spectrometer [33]. All measurements were carried out at 14 K using cooling equipments from Oxford

and Cryogenics, at a repetition rate of 1 kHz.

The two-pulse ESEEM time traces were recorded using the pulse sequence $\pi/2$–τ–π–τ–echo, with pulse lengths of 20 and 40 ns for the $\pi/2$ and π pulse, respectively. The echo intensity was measured as a function of the inter-pulse delay τ, incremented in steps of 10 ns. The spectrometer dead time was 150 ns. For the ENDOR experiments the stimulated electron spin echo sequence $\pi/2$–τ–$\pi/2$–t_1–$\pi/2$–τ–echo was used, with nonselective MW $\pi/2$ pulses and a selective radio frequency (RF) pulse of variable frequency ν_{RF} applied during the time interval t_1 (Mims-ENDOR). The lengths of the MW and RF pulses were 20 ns and 30 μs, respectively, the RF increment was set to $\Delta\nu_{RF}$ = 50 kHz and τ was varied between 200 and 800 ns to avoid signal distortions due to blind spots.

X-band four-pulse ESEEM experiments were recorded with the pulse sequence $\pi/2$–τ–$\pi/2$–t_1–π–t_2–$\pi/2$–τ–echo, with pulse lengths 24 and 16 ns for the $\pi/2$ and the π pulse, respectively. In the 1D combination-peak experiments the echo intensity was measured as a function of time $t_1 = t_2$, incremented from 48 ns to 4480 ns in steps of 8 ns. To avoid blind spots 30 spectra recorded with τ values from 96 to 576 ns (16 ns steps) were added after data processing. In the 2D HYSCORE experiments the echo intensity was measured as a function of times t_1 and t_2, incremented independently from 48 ns to 4096 ns in steps of 16 ns. The two-dimensional spectra represent the sum of 16 experiments recorded with τ values from 96 to 352 ns (16 ns steps). Four-step phase cycles were employed in all experiments to eliminate unwanted echo contributions [47].

S-band HYSCORE experiments were recorded with pulse lengths 20 and 8 ns for the $\pi/2$ and the π pulse, respectively. The spectrum shown in the experimental section is the sum of four spectra measured with τ values of 385, 445, 505 and 565 ns. The time intervals t_1 and t_2 were incremented independently from 200 ns to 3400 ns in steps of 40 ns. Four-step phase cycles were employed in all experiments to eliminate unwanted echo contributions.

5.2.4 Data Manipulation

Data processing was done with BRUKER software (WINEPR) and MATLAB 4.2c (The MathWorks, Inc.). The time traces of the ESEEM data were baseline corrected in one or two dimensions with a fifth-degree polynomial function and apodized with a

Hamming window. Zero-filling was performed prior to Fourier transformation. All frequency domain results represent absolute-value spectra.

The modulations in the two-pulse ESEEM patterns of the sodium and nitrogen nuclei from the inert salt $NaNO_3$ were eliminated by making use of Eq. (3.2). The nuclear g_n factors of ^{13}C and ^{23}Na are 1.405 and 1.478, respectively, and both matrix and combination lines of these two nuclei are in the same frequency range. ^{14}N matrix lines (g_n = 0.404) occur at lower frequencies and are less disturbing. ESEEM spectra representing only the contributions of ^{13}C nuclei were obtained by dividing the time traces of the ^{12}C (natural isotope ratio) and the 98% ^{13}C-labeled carbonate samples. This procedure eliminates the modulations of ^{23}Na, ^{14}N and ^{1}H which are identical for the two samples.

In the ENDOR experiments the sodium signal is eliminated by subtracting the ^{12}C from the 98% ^{13}C-labeled carbonate spectra. The intensity of the proton signals was used to scale the spectra. Both procedures are illustrated in Figure 5-5 on page 79.

5.2.5 EPR and ESEEM Simulations

The g- and A^{Cu}-values obtained from the experimental CW EPR spectra at 130 K were refined by simulations performed with the program COMPAR [95]. With COMPAR, strain effects can be considered by using different linewidths for the four m_I^{Cu}-transitions. For the simulations the **g** and $\mathbf{A}^{Cu}$ matrices were assumed to be axially symmetric with coinciding principal axes.

Two-pulse ESEEM spectra were simulated with the program MAGRES [96]. In these simulations electron Zeeman and hyperfine interactions were considered to include the contributions of the four m_I^{Cu}-states to the ESEEM spectra. An excitation bandwidth of 50 MHz was assumed for the MW pulses. Time traces were computed and a dead time of 150 ns was introduced prior to the processing of the data with MATLAB 4.2c. A homogeneous linewidth of 0.3 MHz was used to account for relaxation effects.

5.3 Results

5.3.1 Optical Spectra

The UV/Vis spectra of the $Cu(H_2O)_6^{2+}$ and the copper-carbonate samples at pH 5.5, 6.5 and 8 are shown in Figure 5-1. The spectra consist of weak, broad bands with λ_{max} values of 810, 780, 760 and 750 nm, respectively. At higher pH the intensity and the width of the bands increase, indicating that a superposition of at least two bands is observed. In agreement with the literature [97] we have assigned these bands to the forbidden *d-d* transitions $d_{x^2-y^2}$ (B_{1g}) $\leftrightarrow$ d_{xy} (B_{2g}) and $d_{x^2-y^2}$ (B_{1g}) $\leftrightarrow$ d_{xz}, d_{yz} (E_g), labeled in the following by ν_2 and ν_3 (cf. Figure 2-2 on page 8). The bands are not resolved due to vibrational and rotational motion of the complexes. For the copper-hexaaquo complex the unpaired electron is located in the $d_{x^2-y^2}$ orbital [92], and we assume the same electronic configuration for the copper-carbonate complexes since the optical and CW EPR spectra (see below) are very similar. The estimated values for ν_2 and ν_3 are given in Table 5-1.

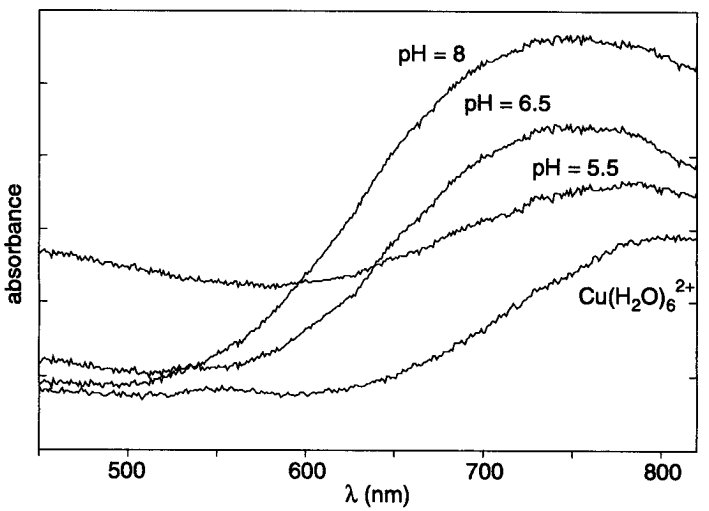

Fig. 5-1 Optical absorption spectra of the copper-hexaaquo and the copper-carbonate samples in aqueous solution at different pH and at RT.

Table 5-1 Electronic transition energies estimated from the optical spectra.

	ν_2 ($cm^{-1} \pm 100$)	ν_3 ($cm^{-1} \pm 100$)
Cu-hexaaquo	12200	13500
Cu-carbonate pH 5.5	12700	14300
Cu-carbonate pH 6.5/8	13300	15400

5.3.2 EPR Spectra

The solution EPR spectrum of $Cu(H_2O)_6^{2+}$ measured at room temperature consists of one broad line centered at $g = 2.19$ (Figure 5-2). For the copper-carbonate samples four transitions are resolved and the centre of the spectrum is shifted to higher fields with g-values of 2.16, 2.16 and 2.15 for pH 5.5, 6.5 and 8, respectively. The splitting of the four lines is approximately 5 mT for all carbonate complexes. The linewidth decreases slightly with increasing pH, leading to a higher resolution.

The frozen solution CW EPR spectra of the same samples measured at 130 K are shown in Figure 5-3. The principal values of the $\mathbf{g}$ and $\mathbf{A}^{Cu}$ matrices obtained from the simulations of these spectra are given in Table 5-2. These values are typical for axially-distorted octahedral complexes with six oxygen ligands [98], the parallel direction being

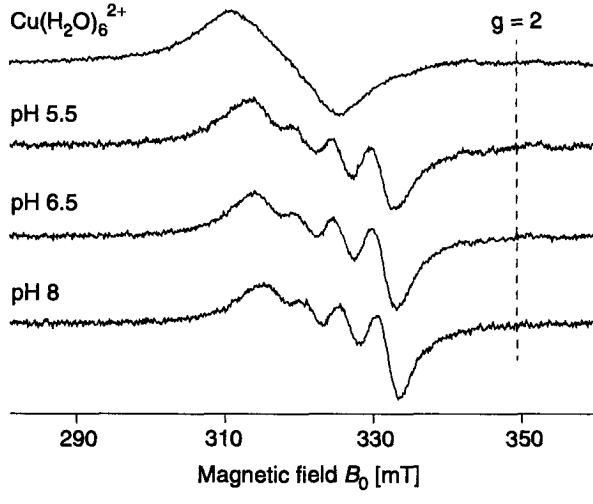

Fig. 5-2 Room temperature CW EPR spectra of the copper-hexaquo and the copper-carbonate samples in aqueous solution at the different pH. The dashed line marks the $g = 2$ position.

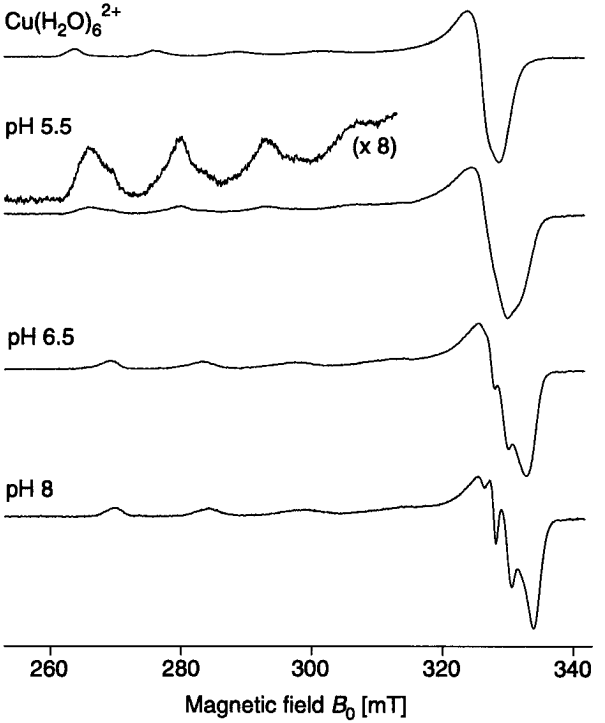

Fig. 5-3 CW EPR spectra of the copper-hexaquo and the copper-carbonate samples in frozen aqueous solution (130 K). The inset for the pH 5.5 spectrum shows an enlarged view of the $g_{\|}$ region to illustrate the presence of several species at this pH.

defined by the distortion axis.The fits obtained for the pH 8 spectrum with axial **g** and $\mathbf{A}^{Cu}$ matrices are quite poor as can be seen from the simulation shown in Figure 5-4. A small orthorhombicity for these matrices can therefore not be excluded. With increasing

Table 5-2 EPR parameters of copper complexes measured at 130 K.

	$g_{\|}$ ($\pm$ 0.001)	$g_{\perp}$ ($\pm$ 0.001)	$\lvert A_{\|}^{Cu}\rvert$ (MHz $\pm$ 10)	$\lvert A_{\perp}^{Cu}\rvert$ (MHz $\pm$ 10)
Cu-hexaaquo	2.403	2.076	425	25
Cu-carbonate pH 5.5	2.370	2.068	445	35
Cu-carbonate pH 6.5	2.336	2.059	470	40
Cu-carbonate pH 8	2.328	2.056	480	50

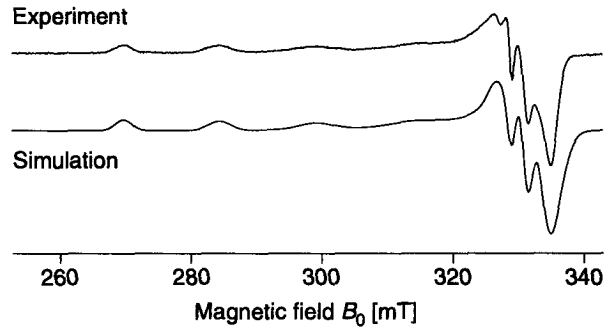

Fig. 5-4 Comparison between experiment and simulation for the copper-carbonate samples at pH 8. The simulation was performed with the parameters given in Table 5-2.

pH, a decrease of the g-values and an increase of the hyperfine couplings is observed, leading to the development of an $A_{\perp}^{Cu}$ hyperfine pattern in the $g_{\perp}$ region. At pH 5.5 minor species contribute to the spectrum which can be identified as hexaaquo and pH 6.5 species by comparing the EPR spectra. This is shown in the enlarged inset in Figure 5-3. Strain effects, arising from the presence of complexes with slightly varying geometries are observed for all spectra. These geometrical strains lead to a distribution of g- and A^{Cu}- values which cancel differently in the four m_I^{Cu}-states and are responsible for the increasing linewidth at higher fields. The strain effects are more pronounced for the copper carbonates than for the hexaaquo complex.

From the g- and A^{Cu}-values given in Table 5-2 and the optical transition frequencies out of Table 5-1 parameters α^2, β_1^2 and β^2 can be calculated using the expressions of Kivelson et al. [98] and Maki et al. [99]. These parameters are measures for the covalency of the σ, π-in plane and the π-out of plane bonds between the Cu^{2+} ion and a set of four oxygen ligands in the equatorial plane, respectively. Values close to 0.5 correspond to complete covalent bonding whereas values close to 1 indicate complete ionic bonding. The calculation has only been done for the pH 8 sample, assuming a complex with two carbonate ligands bound in a bidentate fashion in the xy-plane with axially coordinated water giving only weak perturbations along the z-axis. In this case the ligand orbitals of the four directly coordinated carbonate oxygen atoms can all be considered to be equivalent and sp^2 hybridized. They can form σ and π bonds with the $3d$, $4s$ and $4p$ orbitals of the metal ion.The values obtained for the different parameters are: $\alpha^2 = 0.84$, $\beta_1^2 = 0.84$

and $\beta^2 = 0.66$. Numerical values used for the calculations like the SOC constant for the free Cu^{2+} ion λ_0 are taken from [98].

5.3.3 ESEEM and ENDOR of ^{13}C

All ^{13}C spectra presented in this section were subjected to the procedure described in section 5.2 to eliminate the sodium, nitrogen and proton contributions. The procedure is illustrated in Figure 5-5 for the pH 5.5 case. After division of the two ESEEM time

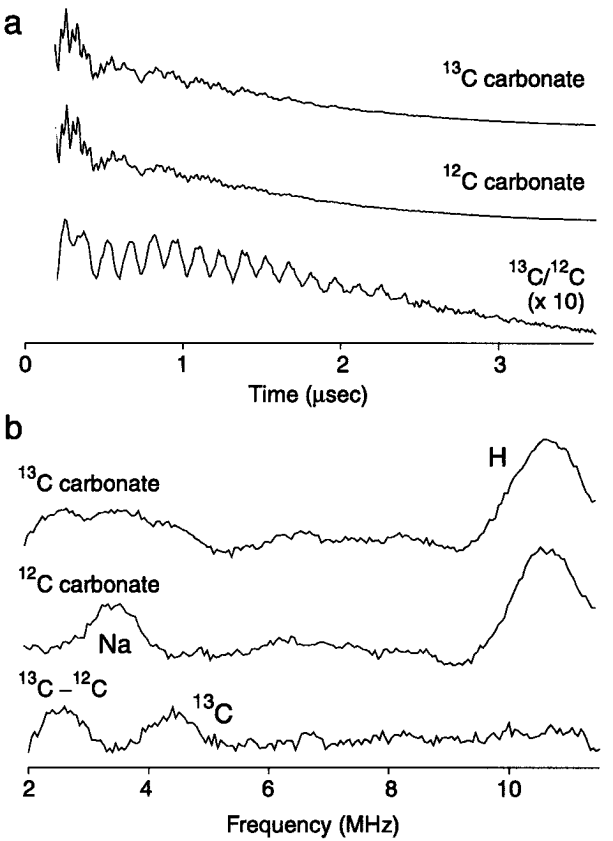

Fig. 5-5 Elimination of the sodium signal for two-pulse ESEEM (a) and Mims ENDOR (b) illustrated by the spectra of the pH 5.5 sample. All spectra are recorded at 14 K at the $g_\perp$-field position. (a) ESEEM time traces of a ^{13}C carbonate and ^{12}C carbonate (natural isotope ratio) sample together with the division of the two traces. (b) ENDOR spectra of the same samples ($\tau = 0.22$ μs). The ^{13}C spectrum is obtained by subtraction of the two spectra.

traces (Figure 5-5a) obtained for the ^{12}C carbonate (natural abundance) and ^{13}C carbonate samples a modulation corresponding mainly to the ^{13}C combination frequency is left (the corresponding spectrum is shown in Figure 5-6b). Subtraction of the corresponding ENDOR spectra (Figure 5-5b) yields an analogous result.

pH 5.5. Two-pulse ESEEM and Mims ENDOR spectra were recorded at different field positions in the range from $g_{\|}$ to $g_{\perp}$. In Figure 5-6a and b ESEEM and ENDOR spectra for the observer position $g_{\|}$ (256 mT) and $g_{\perp}$ (314 mT) are shown, respectively. The prominent features in the ESEEM spectra are the ^{13}C sum combination lines at 5.65 MHz ($g_{\|}$) and 6.9 MHz ($g_{\perp}$). They are shifted by about 0.2 MHz from twice the nuclear Zeeman frequency $2\nu_C$, calculated from the B_0 field values and indicated by dashed lines

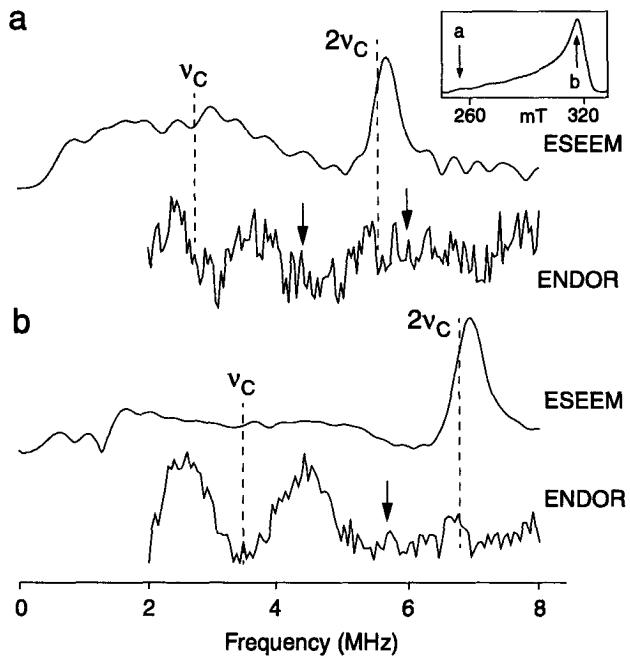

Fig. 5-6 Two-pulse ESEEM and Mims ENDOR spectra of the pH 5.5 sample recorded at the observer field position $g_{\|}$ (a) and $g_{\perp}$ (b), indicated by arrows in the echo-detected EPR spectrum (inset). The nuclear Zeeman frequency ν_C of carbon and the sum combination frequency $2\nu_C$ are indicated by dashed lines. The τ values used for the ENDOR measurements are 0.28 μs (a) and 0.20 μs (b). The arrows indicate the blind spot positions. Other parameters: MW frequency ν_{MW} = 9.10 GHz (ESEEM), ν_{MW} = 9.27 GHz (ENDOR); temperature T = 14 K

in the figures. The basic frequencies ν_α and ν_β, observed as broad features in the range from 1 to 5 MHz, are considerably truncated by the spectrometer deadtime. They are, however, clearly revealed in the ENDOR spectra recorded in the $g_\perp$ region. The arrows indicate the blind spot positions as calculated from Eq. (3.4). That the spectral features in Figure 5-6 are not truncated by the blind spots was confirmed by measurements recorded with different τ values. The spectra show two broad peaks with maxima at 2.5 and 4.5 MHz and linewidths of about 1 MHz, centered round the ^{13}C nuclear Zeeman frequency ν_C = 3.44 MHz. At lower observer fields the S/N ratio is very poor and the ν_α peak is truncated due to the limited frequency range of the ENDOR amplifier (2-30 MHz). ESEEM and ENDOR spectra, recorded at field positions between $g_\parallel$ to $g_\perp$ do not reveal additional information.

pH 6.5/pH 8. The two-pulse ESEEM and Mims ENDOR spectra of the pH 6.5 and pH 8 samples recorded at different field positions are very similar as illustrated by Figure 5-7 and Figure 5-8c. The results obtained from these measurements are therefore treated and discussed together. In Figure 5-7. ESEEM and ENDOR spectra of the pH 8 sample measured at the $g_\perp$ field position are compared. The prominent features in the

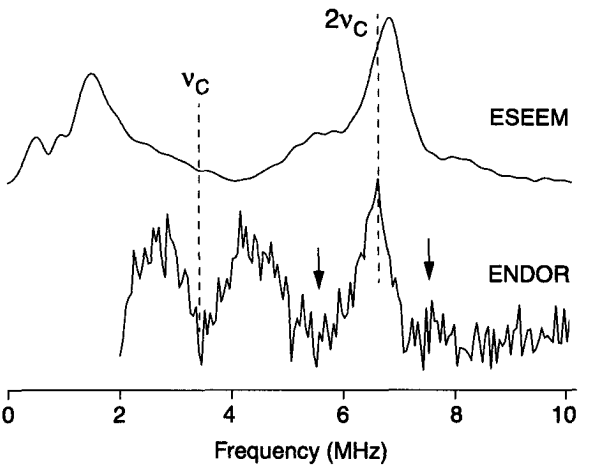

Fig. 5-7 Two-pulse ESEEM and Mims ENDOR spectrum of the pH 8 sample recorded at the $g_\perp$-field position. The dashed lines indicate the nuclear Zeeman frequency ν_C of carbon and the sum combination frequency $2\nu_C$. The arrows indicate the blind spot positions. Parameters: τ value for the ENDOR spectrum: 0.23 µs, T = 14 K, ν_{MW} = 9.12 GHz (ESEEM), ν_{MW} = 9.34 GHz (ENDOR).

ESEEM spectrum are the peaks at 1.5 and 6.8 MHz, the latter one being close to twice the nuclear Zeeman frequency $2\nu_C = 6.76$ MHz. The ENDOR spectrum shows two peaks at 2.7 and 4.2 MHz of width 1.2 MHz, centered round $\nu_C = 3.38$ MHz, similar to the ENDOR features observed for the pH 5.5 sample (Figure 5-6b). An additional ENDOR peak at 6.6 MHz is observed at higher pH. If we assign this peak to a ν_β feature, the ν_α peak is expected to occur in the spectral range 0 to 1 MHz and can not be observed in the ENDOR spectrum. However, the 6.6 MHz line can be associated with the 1.5 MHz peak found in the ESEEM spectrum. Both the ESEEM and ENDOR spectra thus reveal the presence of at least two different ^{13}C nuclei in the complexes formed at pH 6.5 and 8. Besides a weakly coupled ^{13}C already observed at pH 5.5, a stronger coupled ^{13}C is found with a hyperfine coupling close to $2\nu_C$. Numerical values for $2\nu_C$ range from 5.6 MHz at $g_\parallel$ to 6.9 MHz at $g_\perp$.

Consequently the matching condition is fulfilled (cf section 2.2.4). The effect is illustrated in Figure 5-8, where two-pulse ESEEM spectra of the pH 6.5 sample, recorded at different B_0 field positions, are shown. The observer fields are indicated by arrows in the echo-detected EPR spectrum in Figure 5-8 (inset). At field position (b) (Figure 5-8b) the intensity of the ν_α peak at 1.6 MHz increases and the sum peak, clearly visible as narrow feature at 6.8 MHz in Figure 5-8c, appears as a dip in the broad ν_β peak. The features of the weakly coupled ^{13}C nucleus, hidden by the dominant features of the stronger coupled ^{13}C nucleus in the ESEEM spectra in Figure 5-8b and Figure 5-8c, can very nicely be observed at the $g_\parallel$ field position (Figure 5-8a). Here, only spin packets with B_0 approximately along the $g_\parallel$ axis contribute to the spectrum and narrow peaks are observed as a result of this orientation selectivity. The upper bar in Figure 5-8a indicates the basic frequencies, ν_α and ν_β, and the combination frequencies, ν_+ and ν_-, of the weakly coupled ^{13}C nuclei, the lower bar the corresponding frequencies of the strongly coupled ^{13}C nuclei. Hyperfine interactions $A^C(g_\parallel)$ of 0.8 MHz and 9 MHz are obtained from the spectrum for the weakly and strongly coupled nucleus, respectively. The latter fulfills the strong coupling condition ($2\nu_I << A^C$); the basic frequencies ν_α and ν_β are therefore centered round $A^C/2$ and split by $2\nu_C$. Simulations carried out with MAGRES (Figure 5-8) were performed with the parameters given inTable 5-3 and are discussed in section 5.4.3.

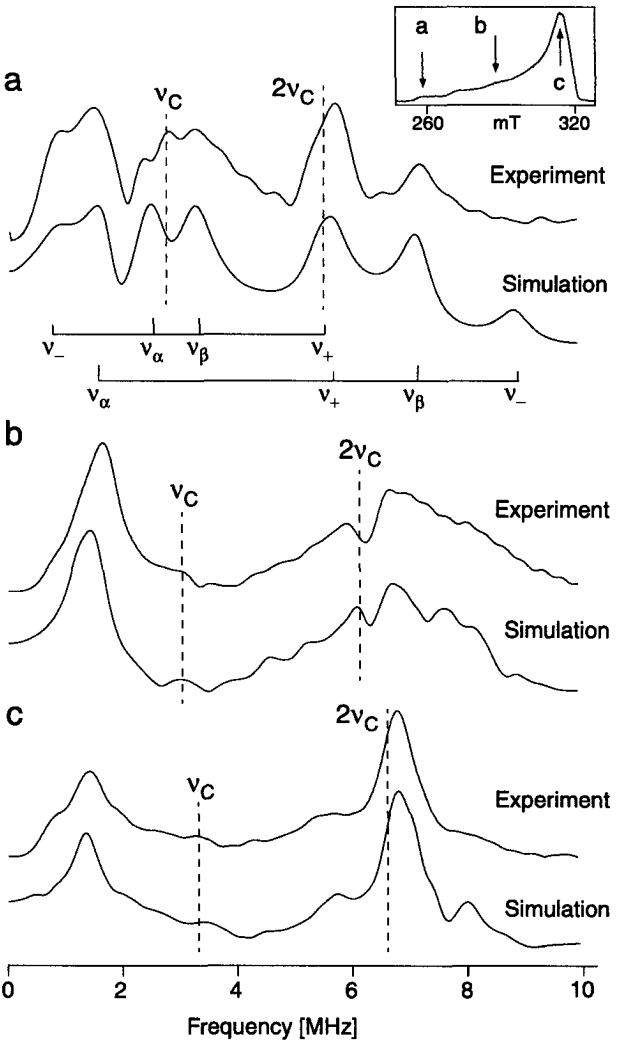

Fig. 5-8 Experimental and simulated two-pulse ESEEM spectra of the pH 6.5 sample, measured at field positions 258 mT (a), 288 mT (b) and 313 mT (c), indicated by arrows in the echo-detected EPR spectrum (inset). The nuclear Zeeman frequency ν_C of carbon and the sum combination frequency $2\nu_C$ are marked by dashed lines for each pair of spectra. The simulation parameters are given in Table 5-3. The upper bar in (a) indicates the basic frequencies, ν_α and ν_β, and the combination frequencies, ν_+ and ν_-, of the weakly coupled ^{13}C nuclei at the $g_\parallel$-position; the lower bar the corresponding frequencies of the strongly coupled ^{13}C nuclei. MW frequency $\nu_{MW} = 9.10$ GHz, temperature $T = 14$ K.

Table 5-3 Hyperfine matrices of the ^{13}C carbonate nuclei for mono- and bidentate coordination, obtained from the MAGRES simulations.

	monodentate coordination[a]	bidentate coordination[b]
$\lvert A_1^C \rvert$ (MHz)	0.1 ± 0.3	4.0 ± 0.1
$\lvert A_2^C \rvert$ (MHz)	0.1 ± 0.3	6.9 ± 0.1
$\lvert A_3^C \rvert$ (MHz)	3.5 ± 0.3	9.0 ± 0.1

a. The principal axis A_3^C is tilted by 75 ± 5 degrees with respect to the $g_{\|}$ axis.
b. A_1^C and A_2^C lie in the $g_\perp$ plane, A_3^C is coaxial to the $g_{\|}$ axis.

5.3.4 1D and 2D ESEEM of Protons

The separation of signals in the 1D four-pulse ESEEM or 'sum peak' spectra is based on the maximum shift Δ_{max} of the peaks from $2\nu_I$ (cf. section 2.2.5), which is proportional to the square of the dipolar coupling constant T. Sum peaks are observed both in two- and four-pulse ESEEM spectra. A better resolution is however obtained in the 1D four-pulse ESEEM experiments due to the T_1-decay of the stimulated echo.

In Figure 5-9 four-pulse ESEEM spectra of the copper-hexaaquo complex, recorded et different field positions (indicated by arrows in the echo-detected EPR spectrum) are shown. The spectra consist of two or three peaks, which show additional shoulders depending on the B_0 field position. The feature close to $2\nu_H$ arises from weakly coupled protons of the solvent molecules. The broad line with the largest shift from $2\nu_H$ can be unambiguously assigned to protons of water molecules coordinated in the equatorial plane since these protons show the largest hyperfine couplings [92]. Δ_{max} values range from 1.2 MHz (d) to 1.5 MHz (b). At lower magnetic fields an additional peak shifted by ~ 0.5 MHz from $2\nu_H$ is observed, which arises mainly from the protons of water coordinated in axial positions. This assignment is however not unambiguous as equatorial protons may also be contribute to the lineshape in this frequency region (see below).

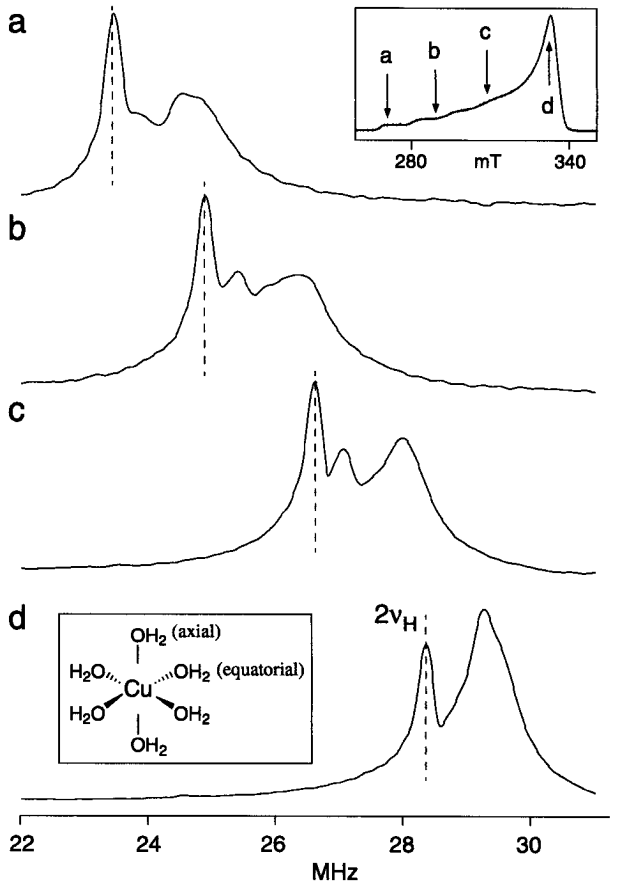

Fig. 5-9 Four-pulse ESEEM spectra of the Cu^{2+} hexaaquo complex (lower inset), measured at field positions 272 mT (a), 290 mT (b), 310 mT (c) and 330 mT (d), indicated by arrows in the echo-detected EPR spectrum (upper inset). The spectra represent the sum of 30 signal traces, measured with τ values between 96 and 576 ns (16 ns steps). The dashed lines indicates twice the proton Zeeman frequency $2\nu_H$. Other parameters: MW frequency ν_{MW} = 9.709 GHz, temperature T = 14 K.

The distinction of equatorial and axial proton signals in the four-pulse ESEEM spectra can be used to determine the number of water molecules coordinated to the central Cu^{2+} at different pH. Four-pulse sum peak spectra of the copper-hexaaquo complex and the three copper-carbonate samples are compared in Figure 5-10. The spectra were recorded at 14 K and at the observer field position 310 mT, indicated by an arrow in the

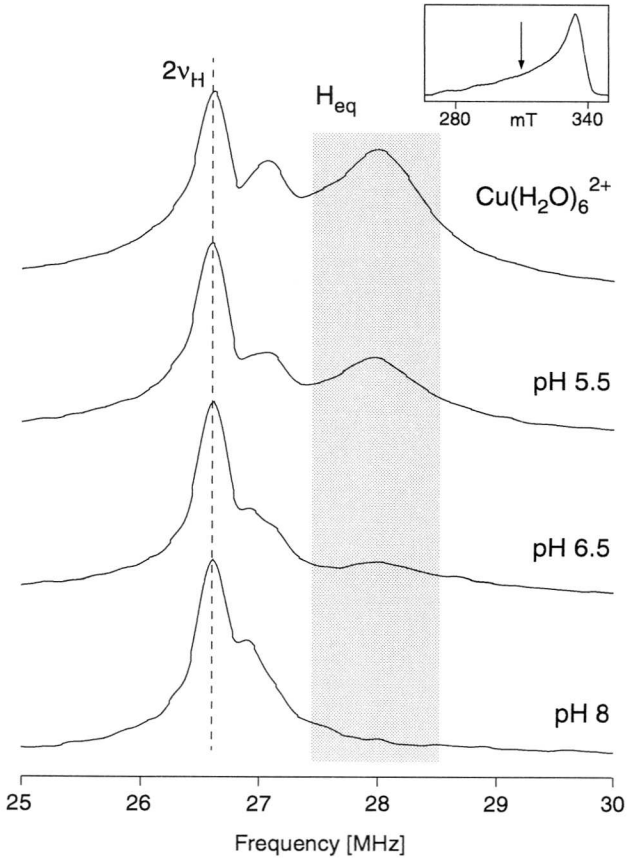

Fig. 5-10 Four-pulse proton ESEEM spectra of the copper-hexaaquo and the copper-carbonate samples at different pH, recorded at the magnetic field position 310 mT, indicated by an arrow in the echo-detected EPR spectrum (inset) of the pH 5.5 sample (ν_{MW} = 9.72 GHz, T = 14 K). The spectra represent the sum of 30 signal traces, measured with τ values between 96 and 576 ns (16 ns steps). The dashed line indicates twice the proton Zeeman frequency $2\nu_H$. The shaded area marks the signals which can be unambiguously assigned to protons of equatorial water molecules.

echo-detected EPR spectrum of the pH 5.5 sample (inset). This observer field corresponds to the position (c) in Figure 5-9, where the different contributions are well separated. In the presence of carbonate ligands, the signal intensity of the equatorial protons decreases with pH (cf. shaded area in Figure 5-10), assuming that the intensity of the

matrix line at $2\nu_H$ is the same for all samples. Simultaneously, position and shape of the proton peak next to the matrix line change. At pH 8 the equatorial proton peak has completely vanished and a new signal shifted by 0.3 MHz from the matrix line is observed.

As already mentioned, contributions from the equatorial protons to the peak shifted by 0.5 MHz from the matrix line can not be excluded. Unambiguous assignments for the axial protons are obtained by spreading the spectra into a second dimension. Therefore HYSCORE spectra of the copper-hexaaquo and copper-carbonate samples were recorded at the observer field 310 mT. Two different representations of the copper-hexaaquo spectrum are shown in Figure 5-11a and b (only one quadrant). Cross-peaks of weakly coupled nuclei are observed along the diagonal, close to the nuclear Zeeman frequency ($\nu_1 = \nu_2 = 13.2$ MHz, matrix line protons). Stronger hyperfine couplings shift the cross-peaks away from the diagonal. In the HYSCORE spectra in Figure 5-11a and b the contributions of axial and equatorial protons appear as well separated ridges to both sides of the matrix peak. The ridges are shifted by 0.35 MHz and 0.85 MHz from the anti-diagonal ($\nu_1 = -\nu_2 + 2\nu_H$), respectively. The peak at (15.6, 15.6) MHz is a spectrometer artifact.

The spectrum of the copper-hexaaquo complex can now be compared to the HYSCORE spectra of the pH 5.5 and pH 8 samples, shown as contour plots in Figure 5-12a and b, respectively. The same contour plot levels were chosen as in Figure 5-11b, scaled by the matrix line intensity. At pH 5.5 the intensity of both the axial and the equatorial proton ridges has decreased. Close to the matrix peak the shape of the signal is altered, indicating a change in the hyperfine coupling of the axial protons. At pH 8, the matrix line is broadened by two shoulders with a maximum shift of approximately 0.2 MHz from the anti-diagonal, as is illustrated in Figure 5-12b. All ridges from equatorial and axial protons have disappeared.

Better resolution of the pH 8 spectrum is obtained at S-band frequencies (2-4 GHz). From Eq. (3.3) it can be seen that the maximum shift Δ_{max} increases if the nuclear Zeeman frequency ν_I is lowered for a given dipolar coupling T. In Figure 5-13b a HYSCORE spectrum recorded at a magnetic field of 136.5 mT (indicated by an arrow in the echo-detected EPR spectrum in Figure 5-13a) and a frequency of 3.713 GHz is shown. A ν_I value of 5.81 MHz is calculated for this field value. The spectrum reveals two main fea-

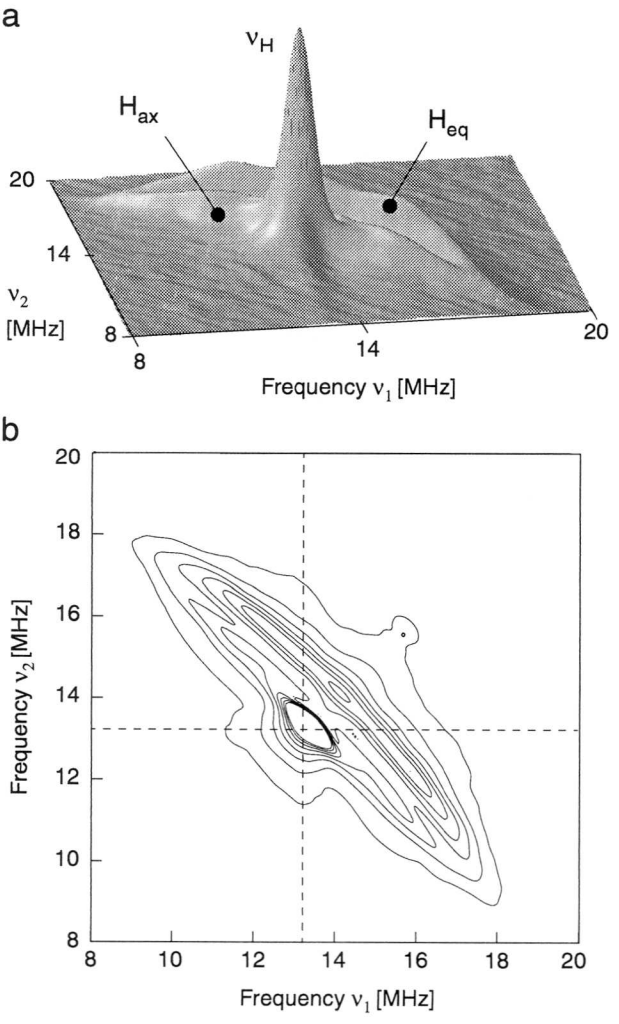

Fig. 5-11 HYSCORE spectra of the copper-hexaquo complex. The two-dimensional plots represent the sum of 16 spectra, recorded at the field position 310 mT with τ values between 96 and 352 ns (16 ns steps), (ν_{MW} = 9.72 GHz, T = 14 K). (a) Surface plot with the assignment of the spectral features to matrix protons (ν_H) and axial (H_{ax}) and equatorial (H_{eq}) water molecules; (b) corresponding contour plot. The dashed lines indicate the proton Zeeman frequency.

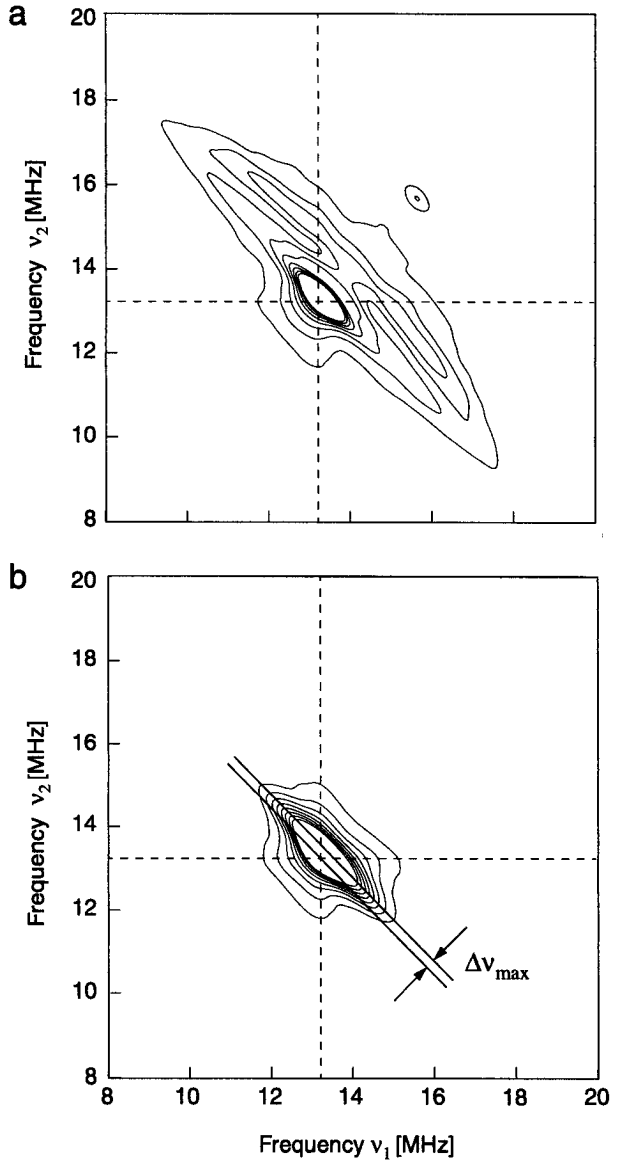

Fig. 5-12 HYSCORE spectra of the pH 5.5 (a) and the pH 8 (b) sample with the same contour plot levels as in Figure 5-11b. For the pH 8 spectrum, the maximum shift $\Delta\nu_{max}$ of the shoulders from the antidiagonal is indicated by the two solid lines. All parameters are the same as in Figure 5-11.

tures, a broad asymmetric peak at the nuclear Zeeman frequency and a ridge shifted by $\Delta\nu_{max}$ ~ 0.35 MHz from the anti-diagonal. The ridge can be related to the shoulders observed in the X-band spectrum whereas the shoulders found close to the matrix line here arise from protons in the second an third coordination sphere (> 4 Å away from the Cu^{2+} ion).

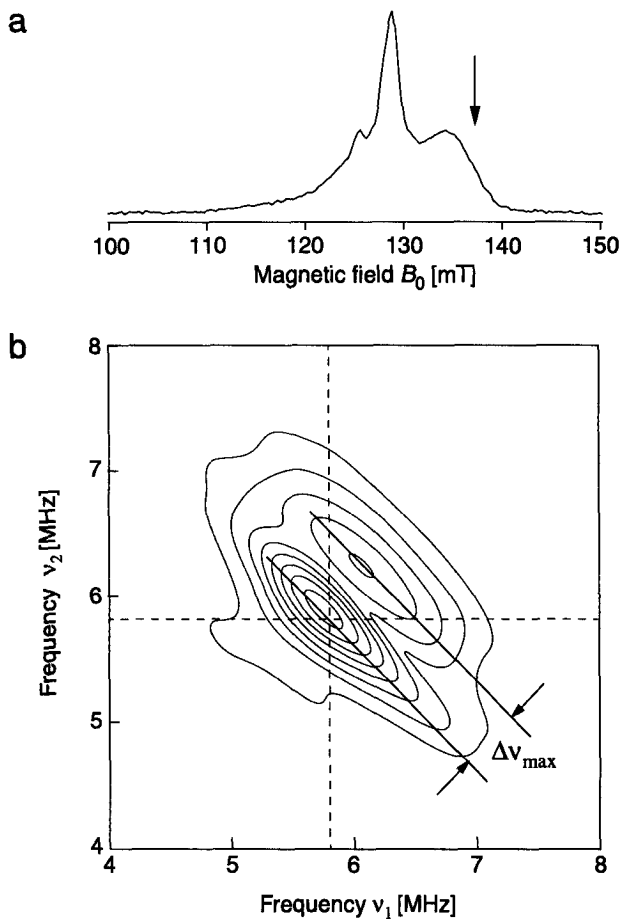

Fig. 5-13 S-band spectra of the pH 8 sample. (a) Echo-detected EPR spectrum recorded with a 20/40 ns two-pulse sequence (ν_{MW} = 3.713 GHz, T = 14 K). (b) The HYSCORE spectrum represents the sum of 4 spectra, recorded at the field position 136.5 mT (indicated by an arrow in (a)) with τ values 385, 445, 505 and 565 ns. The dashed lines indicate the proton Zeeman frequency, the solid lines the shift $\Delta\nu_{max}$.

5.4 Discussion

The experimental results presented in the preceding section confirm the formation of different copper-carbonate complexes as a function of pH. In the following we combine the results and propose structures for the complexes in agreement with the coordination chemistry of copper [24] and carbonates [12,13].

5.4.1 Optical Spectra

The coordination of carbonate to the Cu^{2+} ions leads to an increase of the splitting energies ν_2/ν_3, manifested by a hypsochromic shift (to higher frequencies) in the optical spectra (Table 5-1). Since carboxylic acids induce weaker ligand fields than water or hydroxyl ions [21] a bathochromic shift is expected as a result of the complexation. The increase in energy can, however, be explained by a stronger tetragonal elongation of the Jahn-Teller distorted octahedral copper complexes [11]. An elongation of the axial bond primarily affects the ν_1 transition (cf. Figure 2-2 on page 8). The broad band of the unresolved ν_2/ν_3 transitions will however also be shifted to the blue because of the raise in energy of the $d_{x^2-y^2}$ level and the stabilization of the d_{xz},d_{yz} orbitals. Similar electronic spectra with λ_{max} = 675 nm (~14800 cm^{-1}) are observed, for example, for $Cu(oxalate)_2$ complexes [100].

The increase in intensity of the absorption bands at higher pH indicates a partial breakdown of the Laporte rule stating the forbidden character of d-d transitions. For non-centrosymmetric complexes this breakdown is related to the mixing of d- and p- orbitals induced by covalent bonding with the ligand orbitals [101].

Different coordination schemes are conceivable for chelating ligands like carbonate or oxalate: 1) monodentate complexation at equatorial and axial positions, 2) bidentate complexation in the equatorial plane and 3) bidentate complexation at an equatorial and an axial position in addition to scheme 2, which defines the equatorial plane. The last possibility is highly improbable as it requires a considerable restriction of the axial elongation (cf. $[Cu(en)_x(H_20)_{6-2x}]^{2+}$example in section 4.1.1). The optical spectra do however not allow to distinguish between mono- or bidentate complexation in the equatorial plane.

5.4.2 EPR Spectra

Further evidence for complex formation is given by the CW EPR spectra recorded at room temperature. Various relaxation mechanisms govern the EPR linewidth of copper complexes in solution like spin rotation and modulation of the **g** and hyperfine anisotropies through tumbling of the molecules or interconversion of the Jahn-Teller distortion axis [102-104]. For the $Cu(H_2O)_6^{2+}$ ion, fast relaxation leads to one broad resonance without resolved copper hyperfine interaction. Complexation of carbonate ions hinders the hopping of the distortion axis and decreases the rotational mobility of the complexes. As a result four hyperfine lines with m_I^{Cu}-dependent widths are observed since the **g** and hyperfine anisotropies are not equally well averaged out for the four m_I^{Cu}-states. The g values obtained at pH 5.5 and 6.5 are very similar, the resolution of the m_I^{Cu}-pattern is however higher at pH 6.5. The slightly lower g-value and the smaller linewidth at pH 8 indicates a further slow-down of the tumbling rate. These findings are in good agreement with the calculated speciation (section 4.3.5). The spectra at pH 5.5 and 6.5 can be explained by the formation of the $Cu(CO_3)^0$ complex with considerable contribution of the broad $Cu(H_2O)_6^{2+}$ resonance at pH 5.5. The changes at pH 8 are then due to the coordination of a second carbonate molecule.

At 130 K the molecular motion of the copper complexes is frozen. The g and copper hyperfine parameters given in Table 5-2 show the similarity of the pH 6.5 and pH 8 species, confirmed by the pulse EPR measurements. This result as well as the occurrence of a further well defined species at pH 5.5 are in contradiction to the predictions of the speciation calculations. The freezing procedure therefore seems to influence the complexation equilibria; this issue is addressed in section 5.4.6. The pH 5.5 spectrum also clearly illustrates the simultaneous occurrence of different complexes at this pH. Smaller variations of the geometry might be reflected by the increasing strain effects at higher pH and the small orthorhombicity of the **g** matrix.

The variations of the g- and A^{Cu}- parameters can be related to an increase of the covalency of the σ and π bonding between the carbonate ions and the Cu^{2+} ion. This trend is reflected in the bonding parameters α^2, β_1^2 and β^2 calculated for the pH 8 sample. Although these values are only rough estimates they seem to indicate considerable covalent in- and out-of plane π-bonding between the metal and ligand orbitals. The high cov-

alent bonding character may be explained by the formation of bidentate carbonate complexes at high pH, allowing for the delocalization of electron density from the Cu^{2+} ion through the π system of the carbonate.

5.4.3 ESEEM and ENDOR of ^{13}C

The presence of mono- and bidentate coordination at different pH is clearly revealed by the results of the pulse EPR measurements with ^{13}C-labeled carbonate ligands. At pH 5.5 only a small ^{13}C hyperfine coupling is observed. Using Eq. (2.23) and assuming isotropic **g** and axial hyperfine matrices, an isotropic coupling a_{iso}^{C} = 1.2 MHz and a dipolar coupling T^{C} = 1.1 MHz is estimated from the ENDOR spectra and the shift Δ_{max} = 0.2 MHz in the ESEEM spectra (see also Table 5-3). We assign this coupling to a ^{13}C nucleus of a single carbonate/bicarbonate ion coordinated in the equatorial plane of a monodentate copper-carbonate complex. A tilt of 15 ± 5 degrees of the principal axis of the coupling matrix out of the complex plane is obtained from the simulations of the pH 6.5 sample data. A similar tilt of the monodentate carbonate ligand was found e.g. in the $[Co(CO_3)_2(H_2O)_4]^{2-}$ complex [105]; it can be explained either by intramolecular hydrogen-bonding between carbonate and water molecules in the first coordination sphere or by sterical constraint considerations: the carbonate ligand can only substitute for a smaller water ligand if the planar carbonate π system is twisted out of the equatorial plane. The Cu-C distance of 2.6 Å, obtained from T^{C} (Eq. (2.18)), is smaller than the distance of 2.85 Å, estimated from geometrical models ($r_{Cu\text{-}O}$ = 2 Å, $r_{C\text{-}O}$ = 1.3 Å, angle (Cu-O-C) = 120°, assuming sp^2 hybridization of the O atom). The small ^{13}C coupling can be compared to the orthorhombic hyperfine coupling of the equatorial water protons of $Cu(H_2O)_6^{2+}$, which show the same connectivity (M-O-H) as the carbonate C-atoms[15]. The larger isotropic component observed for the ^{13}C coupling suggests that the delocalization of spin density to the carbonate ligand is higher than to the water ligand and that the ^{13}C HFI is expected to be orthorhombic rather than axial. The broad lines observed in our orientationally disordered systems do not allow for a more detailed interpretation.

Bidentate coordination of carbonate ligands to the Cu^{2+} ion takes place at pH 6.5 and 8 and is reflected by the observation of large ^{13}C hyperfine couplings. Such couplings have been observed by Eaton et al. [106] in their investigation of the interaction between

^{13}C-labeled carbonate and copper(II)-transferrin and lactoferrin and have been assigned to direct complexation of the carbonate to the metal ion; however a detailed analysis is not given in this work. Our parameters for the large hyperfine coupling given in Table 5-3 are based on simulations of the ESEEM spectra (see Figure 5-8). For a detailed analysis of the spectra the orientation selectivity of the MW excitation, the large **g** anisotropy and contributions of up to four m_I^{Cu}-states have to be taken into account. The analysis reveals that the observed spectral features can only be reproduced if the largest principal value of the hyperfine matrix is taken along the $g_{||}$ axis. Further refinement of the spectra is obtained by including in the simulations the contribution of a monodentate carbonate ligand in the equatorial plane. The geometrical arrangement used for these simulations is illustrated in Figure 5-14, together with the orientation of the PAS's of the two ^{13}C hyperfine matrices as described in Table 5-3.

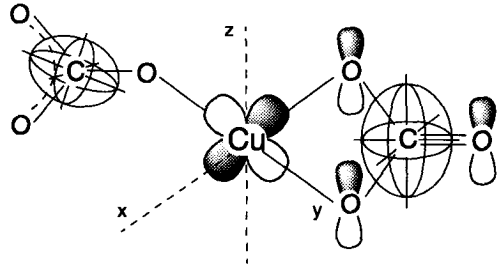

Fig. 5-14 Illustration of the mono- and bidentate coordination of carbonate to the Cu^{2+} ion. The ^{13}C coupling matrices for the two cases are indicated by ellipsoids (not scaled). The copper d_{xz}/ d_{yz} and the oxygen and carbon $2p_z$ orbitals constitute the π system (shown by lobes) which allows for the delocalization of spin density to the ^{13}C.

Three different mechanisms may contribute to the covalent bonding of the carbonate ligands to the metal ion; each of them involves different ligand and metal orbitals [98]. If we assume sp^2 hybridization for the oxygen atoms, coordination can take place via (a) σ-bonding between the $3d_{x^2-y^2}$ and the sp^2 oxygen orbital. Stabilization of the coordination is obtained through (b) in-plane π bonding between the $3d_{xy}$ and the second sp^2 oxygen orbital, not involved in the C-O bond. Overlap between the $3d_{xz}$ and $3d_{yz}$ metal orbitals and the $2p_z$ oxygen orbital leads to (c) out-of-plane π bonding. Via the $2p_z$ oxygen orbital electron density from the Cu^{2+} ion can be delocalized through the carbonate π system. The π system of *monodentate* carbonate ligands is tilted with respect to the 3d orbitals of

the metal due to intramolecular hydrogen-bonding and steric hindrance in the *xy*-plane, making orbital overlap and π bonding more difficult. Polarization of the electron density at the ^{13}C nucleus by the spin density in the carbon $2p_z$ orbital yields explanations for the higher isotropic coupling in the case of *bidentate* complexation and for the orthorhombicity of the large ^{13}C coupling. From the copper-hexaaquo complex it is known that about 5% of the spin density is found on each of the four equatorial water oxygens [92]. A rough model based on point-dipole interactions, with 80% of spin density on the Cu^{2+} ion (at 2.3 Å), 5% spin density on each of the four oxygens (at 1.3 Å) and a spin density of about 0.3% in the $2p_z$ orbital of the C atom (at 0.3 Å, point of maximum electron density [21]) allows one to reproduce the anisotropic part of the large orthorhombic hyperfine matrix with the largest coupling along z. Other mechanisms such as a $Cu(3d_{x^2-y^2})$ - C(2s) "transannular overlap" mechanism [107] or a configuration-interaction (CI) mechanism [28] have been proposed to explain the spin density at the ^{13}C nucleus in similar ring systems, leading to large isotropic ^{13}C couplings. Kirmse et al. [108], for example, have favored the CI mechanism for the explanation of an isotropic ^{13}C coupling of approximately 8 MHz, observed for symmetric $Cu/Ni(et_2dtc)_2$ complexes ($(et_2dtc)_2$ = bis-(diethyl-dithiocarbamate)). Without detailed MO calculations it is difficult to attribute the isotropic coupling to the different mechanisms. Spin density delocalization, however, yields a convincing explanation for the anisotropic part of the large ^{13}C coupling.

5.4.4 1D and 2D ESEEM of Protons

The ^{13}C couplings reveal monodentate coordination of carbonate at pH 5.5, 6.5 and 8 and an additional bidentate carbonate coordination at pH 6.5 and pH 8. Since the complexation of carbonate ligands in the first coordination sphere of the Cu^{2+} ions leads to the removal of water molecules, the measurement of the proton couplings may yield additional information about the coordination shell. Besides the substitution by carbonates two other mechanisms can contribute to changes of the proton couplings, (a) deprotonation of coordinated water molecules at higher pH, leading to the formation of copper-hydroxo complexes, and (b) geometrical rearrangements. At a copper concentration of $5 \cdot 10^{-4}$ M, hydroxo complexes are not expected to form below pH 6 [89] (cf. section 4.3). Above this pH the formation of binuclear $Cu_2(OH)_2^{2+}$ complexes leads to a

decrease of the EPR intensity in the absence of other ligands.

We assign the decrease of the *equatorial* proton signal intensity observed in the four-pulse combination peak and HYSCORE spectra to the substitution of water molecules by carbonate ions. The spectral changes observed for the *axial* protons are mainly due to a change in the coordination. For the equatorial protons an unambiguous assignment is possible at pH 8 where all equatorial coordination positions are occupied by carbonate oxygens whereas at pH 6.5 contributions of at maximum one H_2O/OH^- are still visible. Hydrolysis of the complexes can not be ruled out in this case. The proton spectra are in agreement with the ^{13}C results since mono- and bidentate coordination of two carbonate ions in the equatorial plane involves at least three coordination positions. At pH 5.5 the strong equatorial proton signal suggests that at the most two water molecules have been replaced by carbonate ions. In the combination peak spectra of $Cu(H_2O)_6^{2+}$ and the pH 8 sample Δ_{max} shifts of 0.5 and 0.3 MHz were observed for the axial proton couplings, respectively, and corresponding shifts $\Delta\nu_{max}$ of 0.35 and 0.2 MHz were obtained from the X-band HYSCORE spectra. The better resolved S-band HYSCORE spectrum yields a $\Delta\nu_{max}$ value of 0.35 MHz for the pH 8 sample. From these results distances of 2.8 Å and 3.2 Å can be calculated. The first distance is in good agreement with 2.7 Å, obtained from the data of Atherton et al. [92] for the copper-hexaaquo complex (r_{Cu-O} = 2.2 Å, r_{O-H} = 1 Å, angle (Cu-O-H) = 109°, sp^3 hybridization). From the Cu-H distance of 3.2 Å we then estimate an axial Cu-O distance of about 2.5 Å for the pH 8 sample, which corresponds to an elongation of 0.3 Å of the axial Cu-O bond. The idea of an axial bond elongation due to coordination of carbonate ions in the equatorial plane, suggested by this rough estimation, is supported by the optical spectra. The view is further corroborated by the change in the length of the axial Cu-O bond, observed in compounds like $Na_2Cu(CO_3)_2 \cdot 3\ H_2O$ (r_{Cu-O} = 2.36 Å) or $Cu(OH)_6^{4-}$ (r_{Cu-O} = 2.81 Å) with carbonate and hydroxyl ligands in the equatorial plane [24]. Coordination of carbonate ions at axial positions is not considered since it is thermodynamically unfavorable: for copper-amino complexes, for example, the substitution of four water molecules of the $Cu(H_2O)_6^{2+}$ complex by NH_3 ligands is straightforward, whereas the complexation constant K_5 for an axial ligand is 400 times smaller and K_6 has not been reported [90].

5.4.5 Structure Proposals

In Figure 5-15 structure proposals for the copper-carbonate complexes, present at pH 5.5, 6.5 and 8 in frozen aqueous solution, are given. As discussed before, mixtures of species are to be expected rather than a single species. This is taken into account by atoms drawn in parentheses in Figure 5-15, indicating that unambiguous assignments are not possible from the EPR data and that equilibria may allow for the presence of both structures. The arguments supporting our proposals can be summarized as follows:

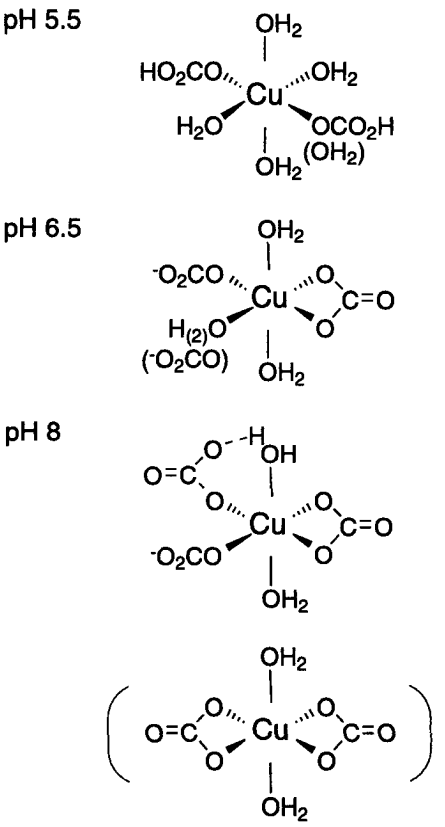

Fig. 5-15 Structure proposals for copper-carbonate complexes in frozen aqueous solution at different pH, as deduced from the experimental results. Features given in parentheses indicate equilibria with possible contributions of both species to the spectra. At pH 8 the presence of complexes with two bidentate rings can not be excluded.

- At pH 5.5 only a small ^{13}C coupling, assigned to monodentate coordination of carbonate in the equatorial plane, and strong hyperfine couplings of two or three equatorial water protons are observed. Internal hydrogen-bonding between non-bound carbonate oxygens and coordinated water as well as steric hindrance favor the trans-coordination of carbonates, as is observed for $[Co(CO_3)_2(H_2O)_4]^{2-}$ and $[Co(NH_3)_4CO_3H_2O]$ complexes ([59],[105]). Species with two carbonates may already show elongation of the Cu-O bond at the axial position. Distinction between species with one or two coordinated carbonates based on the ESE modulation depth [109] is difficult because there is no proper reference system available and the sample contains a mixture of species.

- At pH 6.5 the observation of both small and large ^{13}C couplings gives evidence for simultaneous mono- and bidentate complexation of carbonate ions at the central Cu^{2+} ion. The larger covalency of the equatorial bonds leads to an elongation of the axial Cu-O bond. Contributions from strongly coupled protons point to the coordination of one remaining water or hydroxyl ligand in the equatorial plane.

-At pH 8 all the equatorial positions are occupied by mono- and bidentate carbonate ligands. Internal H-bridging with axial water molecules can stabilize monodentate coordination of carbonate ions. The presence of species with two bidentate carbonate ligands can not be excluded. Elongated axial Cu-O bonds are observed. The coordination of carbonate at axial positions as well as the formation of four-membered rings between equatorial and axial positions is unlikely, due to the Jahn-Teller stabilization.

For the pH 6.5 and pH 8 samples simultaneous mono- and bidentate complexation of carbonate ions at the Cu^{2+} ion is postulated. One could argue that similar spectra are obtained from mixtures of purely monodentate and bidentate species. At pH 8 this would require the presence of approximately equal amounts of bidentate $Cu(CO_3)_2^{2-}$ and monodentate $Cu(CO_3)_4^{6-}$ complexes. The simultaneous formation of these complexes is unlikely, even under non-equilibrium conditions. Furthermore we expect them to show different CW EPR spectra due to the pronounced difference in bonding covalency.

5.4.6 Freezing Effects

The structure proposals deduced from the low temperature EPR results stress the importance of the monodentate coordination at all pH and suggest higher coordination

numbers than the ones expected from commonly accepted complexation constants for copper-carbonate complexes. One could argue that the detailed structures given by the pulse EPR investigations are more reliable than those calculated from the macroscopic complexation constants. On the other hand the CW EPR spectra recorded at room temperature are in better agreement with the predictions from the speciation calculations. It is therefore important to keep in mind that the pulse EPR measurements are performed in frozen aqueous solutions. The temperature dependence of the ion product of water [1] and of the copper-carbonate complexation may be responsible for considerable equilibrium shifts between room temperature and the freezing point of the solution which is lowered due to the cryoscopic effect of the inert salt. Soli et al. [110] showed however that the formation constant of $CuCO_3^0$ decreases at lower temperatures. The same effect has been observed for the formation constants of $CaHCO_3^+$ and $CaCO_3^0$ complexes [111]. The high coordination numbers observed in the frozen aqueous solutions can thus not be explained by the temperature dependence of the complexation constants. Several authors have called attention to the changes in complexation and solution composition that can occur upon freezing [112,113]. Orii et al. [113] have observed local drops in pH of up to 3 units for sodium carbonate-sodium bicarbonate buffers which are due to inhomogeneities of solute concentrations during crystallization. A drop in pH can lead to an acid-catalyzed ring opening [13], thereby increasing the number of monodentate carbonate ligands. Carbonate concentration gradients in the freezing sample on the other hand could account for the formation of $Cu(HCO_3)_x^{2-x}$ and $Cu(CO_3)_x^{2-2x}$ complexes with $x \geq 2$. In 1 M $KHCO_3$ solutions $Cu(HCO_3)_4^{2-}$ complexes have been reported [12]. These reports suggest that the number of coordinated ligands may have been increased by the freezing procedure.

On the other hand there is no direct evidence that freezing induces changes in the complexation mechanism of monodentate and bidentate carbonate ligands to the Cu^{2+} ion. Therefore it seems safe to conclude that our complexation model is also valid for the $Cu(HCO_3)^+$ and $Cu(CO_3)^0$ complexes in aqueous solution. From the view point of aquatic chemistry we notice that bidentate coordination of carbonate to the Cu^{2+} ion is the dominant complexation form whereas monodentate coordination should become important only at low pH or at high carbonate concentrations.

5.5 Conclusions

The combination of different spectroscopic methods has provided detailed information about the geometrical and electronic structures of mono- and bidentate copper-carbonate complexes at different pH. The weakness of the monodentate bonding is reflected by the small interaction observed between the unpaired electron of the Cu^{2+} ion and the ^{13}C nucleus of the carbonate. Although we describe the hyperfine coupling by an axial dipolar interaction matrix, an isotropic coupling $a_{iso}^{C} > 1$ MHz and the comparison with the hyperfine coupling of equatorial protons suggest that the coupling matrix is orthorhombic rather than axial. Bidentate coordination in the equatorial plane leads to a much larger coupling between the unpaired electron and the ^{13}C carbon which can be explained by a higher covalency of the bonding and a delocalization of spin density through the π system of the carbonate ion. A detailed analysis of the large HFI is made possible by the narrow features observed in the ESEEM spectra that are typical for conditions close to exact cancellation. Complexation in the equatorial plane leads to an increase of the bond length for water ligands coordinated at axial positions. The observation of monodentate carbonate coordination at all pH values that have been investigated is in contradiction to the predictions of speciation calculations based on published equilibrium constants. This result as well as the discrepancies between the CW EPR measurements at room temperature and in frozen solution indicate that pH and concentration changes due to non-ideal glass formation might be responsible for equilibrium shifts during freezing. At pH 5.5 and low temperature only monodentate coordination of bicarbonate to the Cu^{2+} ion is found whereas at higher pH both mono- and bidentate carbonate ligands are coordinated in the equatorial plane. The basic mechanisms of mono- and bidentate complexation observed in the frozen samples should also be valid in aqueous solution at ambient temperature. Bidentate coordination is expected to be the dominant coordination form at ambient temperature.

CHAPTER 6

Interactions of Cu^{2+} with Solid Calcium Carbonates

6.1 Introduction

In this chapter the interaction of Cu^{2+} with solid calcium carbonates is investigated by CW and pulse EPR. The interpretation of the spectra is based on the results obtained in chapter 5 for the copper-carbonate complexes in solution. The following questions are addressed in this chapter: How do copper complexes adsorb to the mineral surface? Which complexes are formed at the surface? and How are the metal ions integrated into the crystal lattice?

The majority of the experiments performed to answer these questions are based on the calcium carbonate mineral *vaterite*. Although of minor importance in the natural environment, this mineral has a significant property which simplifies the spectroscopic investigations considerably: its high specific surface area up to 30 m^2/g (specific surface areas of calcite are typically a few m^2/g). Vaterite thus allows for a much higher concentration of surface bound Cu^{2+} ions leading to an improved sensitivity which is especially important in pulse EPR experiments. All pulse EPR measurements involving ^{13}C-labeled carbonate ions have been performed with vaterite. Two approaches are used to introduce ^{13}C-labeled carbonate ions into the system. In a first experiment (1) a copper solution with ^{13}C-labeled carbonate ions is added to unlabeled solid vaterite. In a second experi-

ment (2) a copper solution is added to a suspension of fully ^{13}C-labeled vaterite. With these two experiments all possible ^{13}C couplings to carbonate ligands in solution and at the surface are considered. The fate of the Cu^{2+} ions is then followed during the transformation of vaterite to calcite in water, which is completed within 24 hours or less. According to the different preparation procedures experiments (1) and (2) are labeled $^{13}CO_2$:$Ca^{12}CO_3(vat)$ and $Ca^{13}CO_3(vat)$ throughout this chapter, respectively.

The structure and other properties of vaterite as well as similarities and differences between vaterite and calcite have been discussed in section 4.2. The question, whether the results obtained with vaterite also apply to *calcite* is addressed in a third experiment (3), labeled $CaCO_3(calc)$, where Cu^{2+} ions are adsorbed on calcite powder. The conditions in this experiment are chosen to compensate for the low copper concentrations.

The ^{13}C and proton interactions in the different experiments are observed with 1D and 2D-ESEEM techniques. Two-pulse ESEEM spectra are used to follow the time evolution of the copper-vaterite interaction while detailed ^{13}C coupling parameters are extracted from simulations of the HYSCORE spectra. Specific information about the proton signals of the equatorial and axial water molecules is obtained with the 1D four-pulse ESEEM method.

6.2 Experimental Section

6.2.1 Sample Preparation

(A) Preparation of vaterite: For the preparation of vaterite analytical reagent grade chemicals and double distilled N_2-saturated water was used. Unlabeled vaterite was prepared by pouring 100 mL of a 0.4 M $CaCl_2$ solution into the same volume of a 0.4 M Na_2CO_3 solution at room temperature. The pH of the stirred Na_2CO_3 solution dropped from 11.5 to 10 and a white gel-like precipitate, probably hydrated amorphous $CaCO_3$ [114], was formed during the addition of the $CaCl_2$ solution. The solution was aged by stirring for five minutes and the precipitate was collected on a Buchner filter (porosity 10-16 μm), washed with 30 mL of double distilled water and dried at room temperature under high vacuum for 24 hours[1]. The XRD analysis of the fine white powder obtained by this procedure showed that the precipitate consists mainly of vaterite. REM and TEM

pictures showed spherulitic particles with a mean diameter of approximately 5 µm (cf Figure 4-2 on page 52). These particles are aggregates of a large number of small crystals (< 50 nm, [63]), which explains the high surface areas of up to 30 m^2/g, observed by Nassrallah-Aboukaïs et al. [66,67]. ^{13}C-labeled vaterite was obtained according to the same procedure by addition of 30 mL of 0.2 M $CaCl_2$ solution to the same volume of 0.2 M $K_2{}^{13}CO_3$ solution prepared as described in section 5.2.1.

Attempts were also made to prepare fine grained calcite with specific surface areas high enough to allow for pulse EPR studies with adsorbed copper. Due to the industrial importance of calcite several studies have dealt with the control of crystal size during calcite precipitation [115-117]. Specific surface areas higher than a few m^2/g (crystal sizes 0.5-1 µm) are, however, rarely achieved. Which calcium carbonate polymorph is formed upon the mixing of two Ca^{2+} and CO_3^{2-} solutions depends on various conditions like supersaturation, temperature, pH, etc. [118,119]. Precipitation from highly supersaturated solutions is necessary to obtain a large number of small calcium carbonate crystals. At room temperature this procedure results in the formation of vaterite, whereas at 70 °C pure aragonite is obtained. We were, however, not able to reproduce the results of Wray et al. [118] who found pure calcite at temperatures around 40 °C. Slow mixing of the solutions or aging leads to the formation of large calcite crystals with specific surface areas < 1 m^2/g, too small for our experiments. An alternative procedure for the preparation of fine grained calcite from coarse material is mechanical grinding. Abrasion from the mill and the high pressures during the grinding process may however considerably alter the surface.

(B) Adsorption experiment $^{13}CO_2$:$Ca^{12}CO_3$(vat): In a first experiment a ^{13}C-labeled carbonate solution with a total carbonate concentration of $c_T = 0.05 \pm 0.01$ M was obtained by dilution of the stock solution, prepared as described in section 5.2.1, with N_2-saturated double distilled water. An aliquot of 29 mL of this solution was transferred to a closed vessel connected to a balloon, filled with N_2(g). The pH was adjusted to 7 with 1 M HNO_3 and 1.5 ml of a 10^{-3} M $Cu(NO_3)_2$ solution were added, resulting in a total Cu^{2+} concentration $Cu_T \cong 5 \cdot 10^{-5}$ M. The pH was raised to 9 with 1 M KOH and the

1. Other drying methods like heating the vaterite up to 100 °C were found to diminish the adsorption efficiency of the mineral.

solution stirred for five minutes. The solution was then added under stirring to 0.8 g of a *vaterite* slurry in a second vessel, obtained by addition of several drops of water to the vaterite in order to obtain a homogeneous suspension. This resulting suspension was also kept under an N_2 atmosphere. Samples of 2 mL were taken at different time intervals with a syringe and passed through cellulose nitrate filters of porosity 0.1 µm. The filtrate was washed with 1 mL of double distilled water and the rolled moist filters were introduced into an EPR tube and frozen in liquid nitrogen. Samples were taken immediately after the addition of the carbonate solution, after 10, 30, 60 minutes and 2, 3, 6 and 24 hours. Bare filters treated with an aqueous 10^{-3} M $Cu(NO_3)_2$ solution did not show any affinity for the Cu^{2+} ions.

(C) Adsorption experiment $Ca^{13}CO_3$(vat): In a second experiment 0.25 g of ^{13}C-labeled *vaterite* was added in a closed vessel to 20 mL of N_2-saturated double distilled water, kept under a N_2 atmosphere. The resulting pH of 10 was lowered to 8.5 with 1 M HNO_3 and 0.5 mL of a 10^{-3} M $Cu(NO_3)_2$ solution were added under stirring, resulting in a total Cu^{2+} concentration $Cu_T \cong 2.5 \cdot 10^{-5}$ M. Samples of 3 mL were taken immediately after the addition of the copper solution and after 5, 15 and 60 minutes as well as after 24 hours, according to the procedure described above.

(D) Adsorption experiment $CaCO_3$(calc): In the third experiment 10 g of highly crystalline *calcite* (Merck, suprapur) were washed with acetone (puriss) and dried under high-vacuum for twelve hours. All other commercial calcites of lower crystallinity and possibly higher specific surface areas tested in this study were found to exhibit strong Mn^{2+} EPR signals. The washed calcite was added to 220 mL of N_2-saturated double distilled water in a closed vessel, kept under an N_2 atmosphere. The pH of the resulting suspension was lowered from 9.8 to 8.5 with 1 M HNO_3 and 3 mL of a 10^{-4} M $Cu(NO_3)_2$ solution were added under stirring, resulting in a total Cu^{2+} concentration $Cu_T \cong 1.4 \cdot 10^{-6}$ M. Samples of 25 mL were taken immediately after the addition of the copper solution and after 30 and 90 and 150 minutes. The solid carbonate was collected on a Buchner filter (porosity 10-16 µm), washed with double distilled water and stored in liquid nitrogen in form of compressed blocks of cylindrical shape.

(E) AAS measurements: The amount of copper in solution was determined as a function of time by atomic adsorption spectroscopy. The measurements were performed

on filtrates obtained from a $^{13}CO_2$:$Ca^{12}CO_3$(vat) adsorption experiment. The copper amount on the filter was determined by treating the filters with a known amount of HNO_3(conc) solution to dissolve the calcium carbonate collected on the filter. The experimental error of these measurements was 10%.

6.2.2 Equipment

CW and pulse EPR spectra were recorded as described in section 5.2.3, except for the two-pulse ESEEM spectra which were recorded on the Bruker ESP 380E spectrometer. The length of the $\pi/2$ and π pulses were 8 and 16 ns, respectively and the inter-pulse delay τ was incremented in steps of 8 ns. The ^{13}C HYSCORE spectra shown in the result section were recorded with a single τ value. Control experiments with different τ values were, however, performed to assure that the lines were not accidently truncated by blind spots. For the CW EPR measurement at room temperature the filter was cut in stripes and fixed to a quartz flat cell. The temperature series for the sample taken after 24 hours was recorded using a liquid helium cryostat from APD cryogenics. The 16 K spectrum of this series was measured with a modulation amplitude of 0.03 mT. For the CW EPR measurements performed on samples of the $CaCO_3$(calc) experiment the frozen cylinders were introduced directly into a finger dewar and measured at 77 K. With this procedure the amount of sample that could be measured exceeded 1 g, leading to more intense EPR signals. For the pulse EPR spectra a maximum of sample was packed into a standard EPR tube.

The XRD analysis was performed on a Scintag XDS 2000 with CuK_α irradiation. The AAS data were obtained with a graphite tube AAS 2100/HGA 700 from Perkin Elmer. Merck Titrisol 9987 standard copper solutions (0 - 40 µg/L) were used for calibration of the instrument. Samples with higher copper concentrations were diluted by a factor 100 prior to measuring.

6.2.3 Data Manipulation

Data processing was done in analogy to the procedures given in section 5.2.4. As the samples were prepared without the glass forming agent $NaNO_3$, no background signals from ^{23}Na or ^{14}N had to be eliminated. The AAS data were drawn using the program

MICROCAL ORIGIN 3.5.

6.2.4 EPR and HYSCORE Simulations

The g- and A^{Cu}- values obtained from the experimental CW EPR spectra at 130 K were refined by simulations performed with MATLAB 4.2c routines, based on second order perturbation formulae [120]. For the simulations the **g** and $\mathbf{A}^{Cu}$ matrices were assumed to be axially symmetric with coinciding principal axes.

HYSCORE spectra were simulated with a home-written C++ program. The output of the program, a four-pulse ESEEM time-domain signal, was calculated using the formula published in [37,47] (Appendix B.3). The HF couplings were treated in the point-dipole approach as discussed in section 2.2.2. For the computation of the nuclear frequencies the effects of an axial **g** matrix were taken into account [42]. Input parameters of the program were thus a_{iso}^{C}, T/g_e and the angle θ_I between the z-axis ($g_{\|}$ direction) and the vector connecting electron and nuclear spin. Orientation-dependent contributions of the different m_I^{Cu}-states were taken into account for the simulations.

6.3 Results

6.3.1 AAS Measurements

The solution copper concentrations measured by AAS as a function of time are drawn on a logarithmic scale in Figure 6-1. The initial copper concentration at time $t = 0$ is in agreement with the theoretical concentration calculated from the experimental preparation (3100 µg/L) and is indicated by the dashed line in Figure 6-1. Five minutes after the addition to the vaterite, more than 95% of the copper is removed from solution. After this rapid initial uptake the copper concentration in solution decreases more slowly. After six hours the signal is close to the blank signal (5 µg/L). The control experiment after 24 hours shows that 90% of the copper is found on the filter, associated with the vaterite.

6.3.2 EPR Spectra

In Figure 6-2 the EPR spectra of vaterite samples prepared according to the experimental procedure $^{13}CO_2{:}Ca^{12}CO_3(vat)$ are shown. These spectra are very similar to

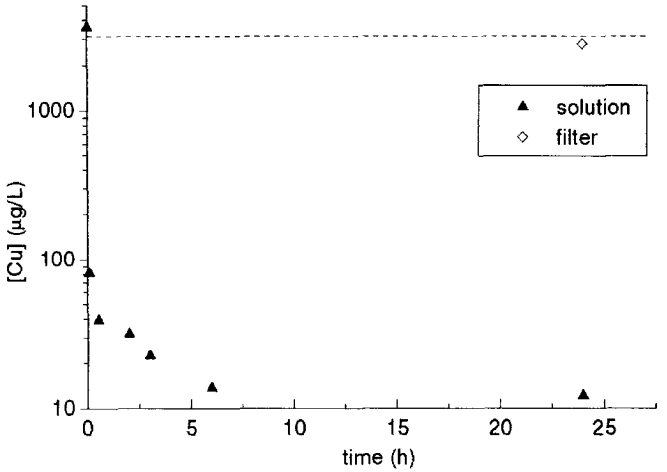

Fig. 6-1 Copper concentrations in the filtrates and filter solutions as determined by AAS. The dashed line indicates the calculated total copper concentration.

those obtained from samples from the $Ca^{13}CO_3(vat)$ experiment which are therefore not shown. The time scale for the two experiments is, however, different: the spectral changes illustrated in Figure 6-2 take place more rapidly in the $Ca^{13}CO_3(vat)$ experiment, approximately by a factor of five.

The enlarged views of the $g_{||}$ region indicate the presence of two copper species associated with the vaterite surface, marked by *(A)* and *(B)* in Figure 6-2. The bars indicate the $A_{||}$ hyperfine splitting. No major spectral changes are observed during the first 30 minutes after the addition of the copper solution to vaterite. The initial spectrum is dominated by the *(A)* species. The principal values of the axial **g** and $\mathbf{A}^{Cu}$ matrices obtained from the simulations of the EPR spectra (see below) are given in Table 6-1. These values are typical for axially-distorted octahedral complexes with six oxygen ligands [98], the parallel direction being defined by the distortion axis. Washing of the filtrates has only marginal effects on this signal. After two hours the spectrum of a second species *(B)*, hidden by the intense signal *(A)* in the initial spectrum shows up clearly. The intensity of the signal *(A)* has decreased. Two additional spectral features are marked in the spectrum obtained from the sample taken after six hours: an isotropic spectrum with a *g*-value of 2.247 and a linewidth of ~5 mT, labeled *(C)* in Figure 6-2, and weak narrow peaks at the

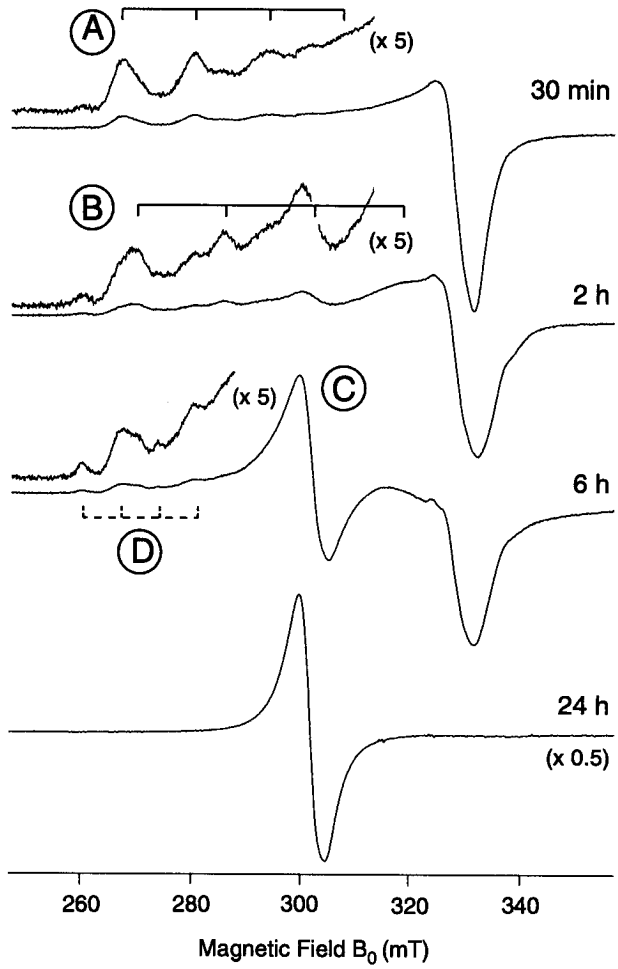

Fig. 6-2 CW EPR spectra of vaterite filter samples taken at different time intervals and measured at 130 K. The samples were obtained from an $^{13}CO_2$:$Ca^{12}CO_3$(*vat*) experiment. The insets show enlarged views of the $g_{\|}$ region to illustrate the presence of several species, identified by the four-line pattern in the low-field region and labeled by A, B, and D.

lower end of the spectrum, tentatively assigned to a species *(D)*. The intensity of both features grows continuously in the first 6 hours. After 24 hours, however, the isotropic spectrum *(C)* is the only remaining spectral feature.

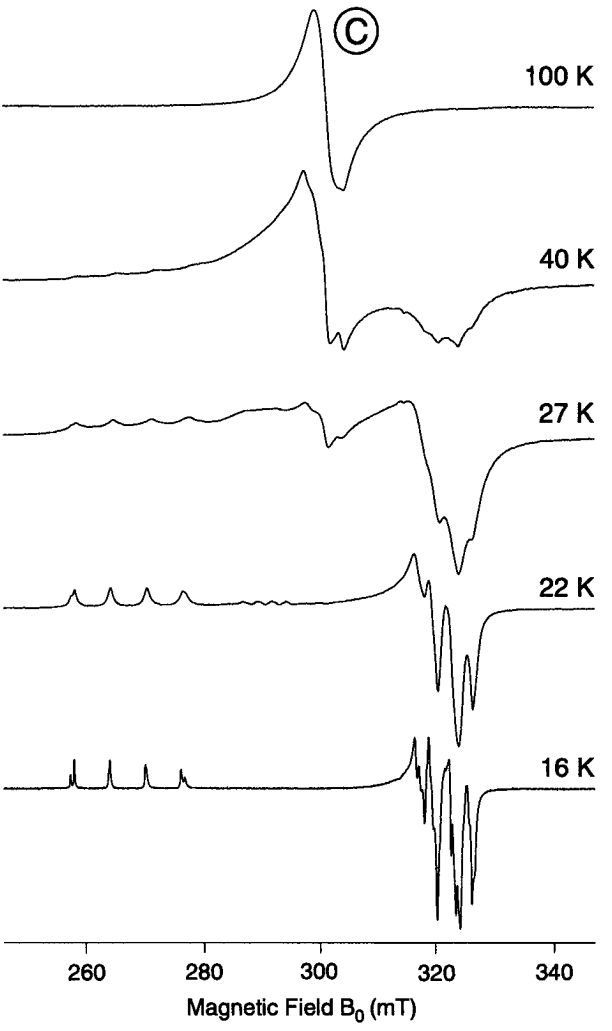

Fig. 6-3 Temperature dependence of the EPR signal of the sample taken after 24 hours in a $^{13}CO_2$:$Ca^{12}CO_3$(*vat*) experiment. The scaling of the spectra is arbitrary. The 16 K spectrum was recorded with a modulation amplitude of 0.3 G.

If the sample taken after 24 hours is cooled down below 100 K a drastic change is observed for signal *(C)*, as illustrated in Figure 6-3. At 40 K the isotropic line converts to an anisotropic copper spectrum. Further lowering of the temperature leads to a line narrowing of the anisotropic spectrum and the complete disappearance of the isotropic spec-

Table 6-1 EPR parameters of the different copper species observed in Figure 6-2 and Figure 6-3 and refined by simulations (Figure 6-4).

	$g_{\parallel}$ (± 0.001)	$g_{\perp}$ (± 0.001)	$\lvert A_{\parallel}^{Cu}\rvert$ (MHz ± 10)	$\lvert A_{\perp}^{Cu}\rvert$ (MHz ± 10)
Species A	2.358	2.066	440	20
Species B	2.305	2.065	510	20
Species C (T>100 K)	g_{iso} = 2.247	-	A_{iso} [a]	-
Species C (T<20 K)	2.530	~ 2.106	215 (^{63}Cu)	~ 90 (^{63}Cu)
			230 (^{65}Cu)	~ 90 (^{65}Cu)
Species D	~ 2.51	-	~ 240	-

a. the coupling to the nuclear spin of copper is not resolved.

trum. At 16 K a copper spectrum with very narrow lines is observed, which allows for the distinction of the two copper isotopes ^{63}Cu and ^{65}Cu in the $g_{\parallel}$ region. The additional splittings in the $g_{\perp}$ region are due to second order effects of the copper NQI. The $g_{\parallel}$ and $A_{\parallel}^{Cu}$ values given in Table 6-1 for the low temperature spectrum of species *(C)* are taken from simulations whereas the perpendicular values are only estimates, able to reproduce the main features of the spectrum.

In Figure 6-4 the spectral simulations are shown by which the *g*- and *A*-values in Table 6-1 were determined. In Figure 6-4a the simulated spectra of the individual species *(A)*, *(B)* and *(C)* (isotropic) are drawn. Figure 6-4b compares the experimental spectra to best fits, obtained by a weighted addition of the individual spectra. The weighting factors for the species *(A)* and *(B)* are given in the figure. The weighting factor of the isotropic spectrum *(C)* has no physical meaning due to the peculiar mechanisms leading to this line (see discussion section) which are not accounted for in the simulation procedure. In the simulations strain effects leading to m_I^{Cu}-dependent line widths are neglected. The $g_{\parallel}$ and $A_{\parallel}^{Cu}$ values for species *(D)* in Table 6-1 are estimates from the EPR spectrum.

In Figure 6-5 the second (2 h) EPR spectrum from Figure 6-2, recorded at 130 K, is compared to the corresponding spectrum observed at room temperature for a sample taken after three hours. The S/N ratio of the RT spectrum is poor. The main difference between the spectra is an additional feature in the RT spectrum with a *g*-value of 2.16 and a line width of ~ 6 mT, marked by an asterisk in Figure 6-5.

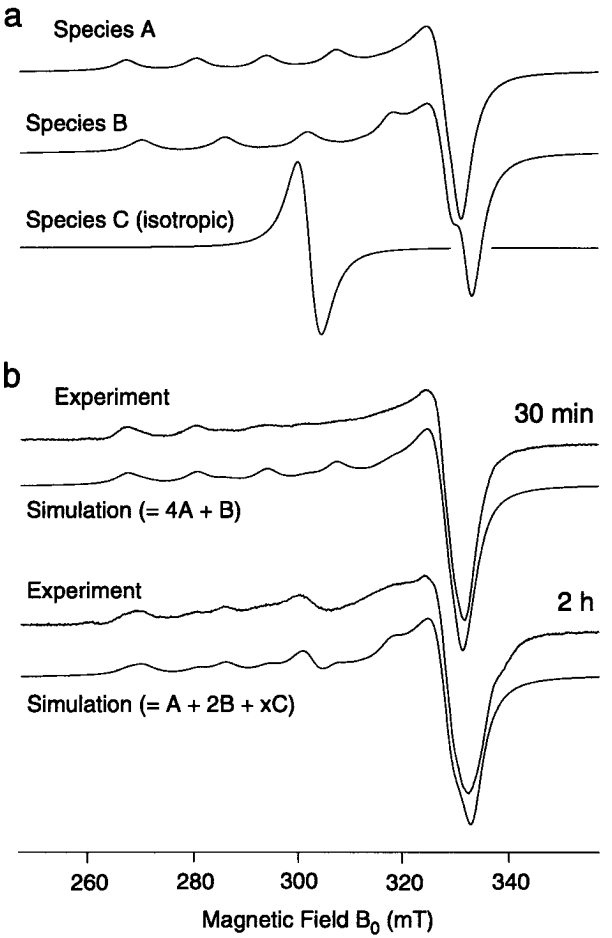

Fig. 6-4 (a) Simulations of the individual spectra of the three species *(A)*, *(B)* and *(C)* with the parameters given in Table 6-1. (b) Simulations of the experimental spectra shown in Figure 6-2 by combination of the individual spectra. The weighting factors for the *(A)* and *(B)* spectra are given in the figure. The weighting factor of spectrum *(C)* has no physical meaning (see text).

So far we have only shown EPR spectra of *vaterite* samples obtained from $^{13}CO_2$:$Ca^{12}CO_3$*(vat)* experiments and noted that the $Ca^{13}CO_3$*(vat)* spectra are very similar. In Figure 6-6 two examples of spectra obtained from *calcite* samples of a $CaCO_3$*(calc)* experiment are drawn. The features observed in these spectra are similar to those found for the vaterite samples. The dominant species after 10 minutes labeled by

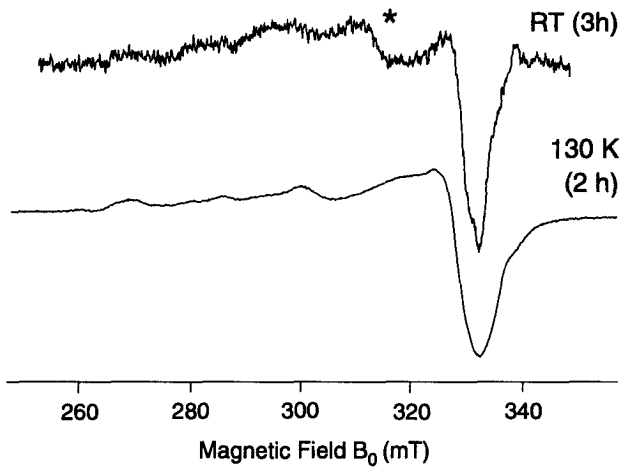

Fig. 6-5 Comparison of the EPR spectra of samples from a $^{13}CO_2$:$Ca^{12}CO_3$*(vat)* experiment, measured at room temperature and at 130 K and taken after similar time intervals. The B_0-offset between the two spectra due to the different MW frequencies has been corrected in this plot. The line marked by an asterisk in the RT spectrum is discussed in the text.

(A') exhibits EPR parameters close the ones of species *(A)* in Figure 6-2 ($g_{||} = 2.37$, $\left|A_{||}^{Cu}\right| = 430$ MHz, $g_{\perp} = 2.07$). The linewidth of the isotropic spectrum *(C)* observed after 90 minutes is broader than the corresponding vaterite spectrum since the spectra are

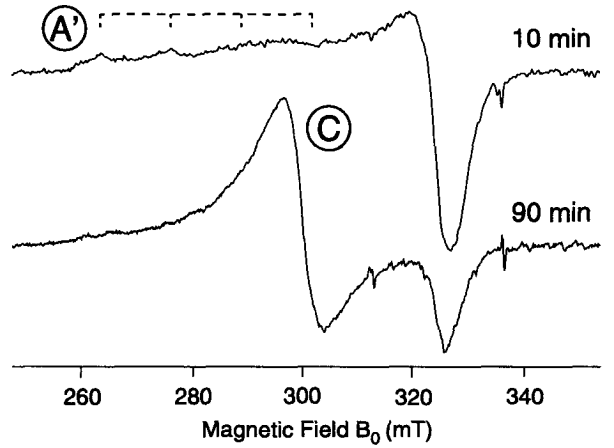

Fig. 6-6 CW EPR spectra of calcite samples, obtained from a *$CaCO_3$(calc)* experiment and taken at different time intervals. Temperature T = 77 K.

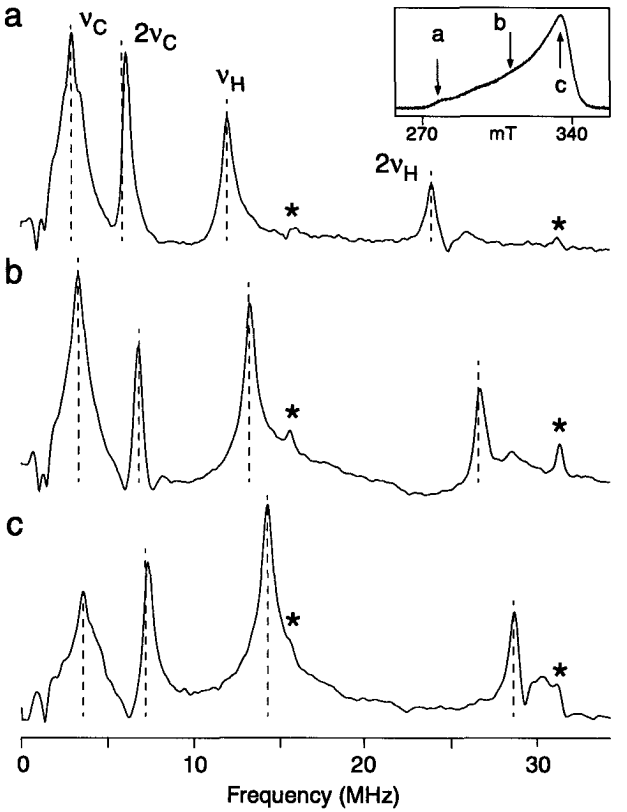

Fig. 6-7 Two-pulse ESEEM absolute-value spectra of the sample taken after 2 hours in a $^{13}CO_2$:$Ca^{12}CO_3$(*vat*) experiment, measured at field positions 281 mT (a), 312 mT (b), and 336 mT (c), indicated by arrows in the echo-detected EPR spectrum (inset). The nuclear Zeeman frequency ν_C of carbon and ν_H of protons as well as the sum combination frequencies $2\nu_C$ and $2\nu_H$ are marked by dashed lines for each spectrum. The peaks at 15.6 and 31.25 MHz, marked by asterisks, are spectrometer artifacts. MW frequency ν_{mw} = 9.709 GHz, temperature T = 16 K.

recorded at lower temperatures. The transformation shows a similar time evolution as in the $Ca^{13}CO_3$(*vat*) experiment. The S/N ratio is poor as compared to the vaterite spectra due to the lower copper concentration.

6.3.3 Two-Pulse ESEEM

The two-pulse ESEEM spectra of the samples obtained from $^{13}CO_2$:$Ca^{12}CO_3$(*vat*) and $Ca^{13}CO_3$(*vat*) experiments exhibit both intense ^{13}C and proton signals. This is illus-

trated in Figure 6-7 for a sample taken in a $^{13}CO_2$:$Ca^{12}CO_3$(vat) experiment after 2 hours. The three spectra were recorded at different field positions, indicated by arrows in the echo-detected EPR spectrum in the inset. The main features of the spectra are four peaks approximately at the nuclear Zeeman frequencies of carbon ν_C and hydrogen ν_H and at the corresponding sum-combination frequencies $2\nu_C$ and $2\nu_H$, indicated by dashed lines for each spectrum. The basic carbon peak is broadened by shoulders and its intensity decreases in going from $g_{\|}$ to $g_{\perp}$. The carbon sum combination peak is narrow with a frequency close to $2\nu_C$. The proton sum combination line consists mainly of the matrix signal while the signals arising from the strongly coupled equatorial protons shifted

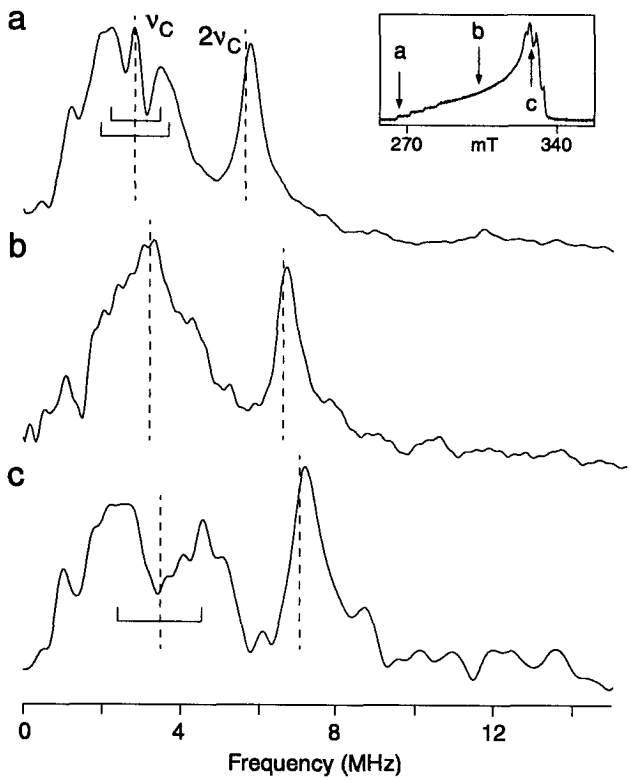

Fig. 6-8 Two-pulse ESEEM spectra of the sample taken after 24 hours in a $^{13}CO_2$:$Ca^{12}CO_3$(vat) experiment, measured at field positions 267 mT (a), 307 mT (b) and 330 mT (c), indicated by arrows in the echo-detected EPR spectrum (inset). The nuclear Zeeman frequency ν_C of carbon and the sum combination frequency $2\nu_C$ are marked by dashed lines. MW frequency ν_{mw} = 9.706 GHz, temperature T = 16 K.

away from $2\nu_H$ to higher frequencies (cf Figure 5-9 on page 85) appear as small humps.The peaks at 15.6 and 31.25 MHz, marked by asterisks in Figure 6-7, are spectrometer artifacts. The two-pulse ESEEM spectra shown above can be attributed to species *(A)* and/or *(B)* since these species give the main contribution to the corresponding EPR spectrum.

Figure 6-8 shows two-pulse ESEEM spectra for the 24 hours sample (species *(C)*) obtained from a $^{13}CO_2$:$Ca^{12}CO_3$*(vat)* recorded at three different field positions, indicated by arrows in the echo-detected EPR spectrum in the inset. Only ^{13}C peaks contribute to these spectra; proton signals are missing completely. At $g_{\|}$ two lines centered about the carbon nuclear Zeeman frequency are observed split by approximately 1.2 MHz with shoulders split by 1.5 MHz. Both splittings are indicated in Figure 6-8a. With increasing field a broadening of these lines is observed and at $g_{\perp}$ the splitting has increased to 2.1 MHz (Figure 6-8c). The intensity of the narrow ν_C peak decreases when going from $g_{\|}$ to $g_{\perp}$. The sum combination peaks are shifted by approximately 0.15 MHz

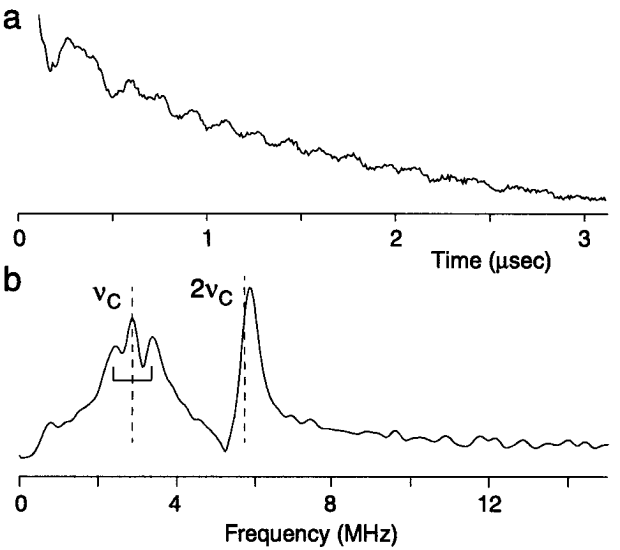

Fig. 6-9 (a) Two-pulse ESEEM time trace of the sample taken after 2 hours in a $^{13}CO_2$:$Ca^{12}CO_3$*(vat)* experiment, recorded at the lower end of the EPR spectrum (observer field 270 mT / species *(D)*). (b) Corresponding ESEEM spectrum. The nuclear Zeeman frequency ν_C of carbon and the sum combination frequency $2\nu_C$ are marked by dashed lines. MW frequency ν_{mw} = 9.712 GHz, temperature T = 16 K.

from the $2\nu_C$ position. At $g_\perp$ the ^{13}C modulation is shallow resulting in a poor S/N ratio.

In Figure 6-9a and b a two-pulse ESEEM time trace and the corresponding spectrum of the sample taken after two hours in a $^{13}CO_2$:$Ca^{12}CO_3$(vat) experiment are shown. The spectrum was recorded at the low observer field 270 mT and can be related to species *(D)* in Figure 6-2. The time trace is drawn to illustrate the deep modulations observed for the ^{13}C signal. A splitting of ~ 1 MHz about the carbon nuclear Zeeman frequency similar to the one found for the 24 hours sample at $g_\parallel$ in Figure 6-8a is observed. Proton signals are again missing in this spectrum.

Figure 6-10 shows the time evolution of the two-pulse ESEEM spectra for samples of a $^{13}CO_2$:$Ca^{12}CO_3$(vat) experiment taken after 5 minutes, 30 minutes and 3 hours. The time series were recorded at the field position 280 mT (a), 312 mT (b) and 336 mT (c). The most important changes are observed in the $g_\parallel$ region and affect the relative intensity of the carbon and proton signals (Figure 6-10a). In the $g_\perp$ region the spectra remain practically unaltered (Figure 6-10c). At B_0 = 312 mT extra features are observed for the spectrum taken after 5 minutes, indicated by arrows in Figure 6-10b. The intensity of these features decreases rapidly. The asterisks again mark spectrometer artifacts.

In this section no $Ca^{13}CO_3$(vat) experiment spectra are shown because they are very similar to the spectra observed for $^{13}CO_2$:$Ca^{12}CO_3$(vat) experiment samples, except for the somewhat broader line widths, leading to a lower resolution. This broadening is due to T_2' relaxation processes, indicating a higher density of Cu^{2+} ions at the vaterite surface.

6.3.4 HYSCORE of ^{13}C

In the HYSCORE experiment the broad ^{13}C lines observed as truncated features in the two-pulse ESEEM spectra are clearly revealed. Simulations of the spectra allow for the determination of the coupling parameters, summarized for species *(A)*, *(B)* and *(C)* (low temperature) in Table 6-2.

In Figure 6-11 experimental HYSCORE spectra of the sample taken after 2 hours in a $^{13}CO_2$:$Ca^{12}CO_3$(vat) experiment are shown. The measurements were recorded at the $g_\parallel$ and $g_\perp$ field positions, indicated by (a) and (c) in the echo-detected spectrum in

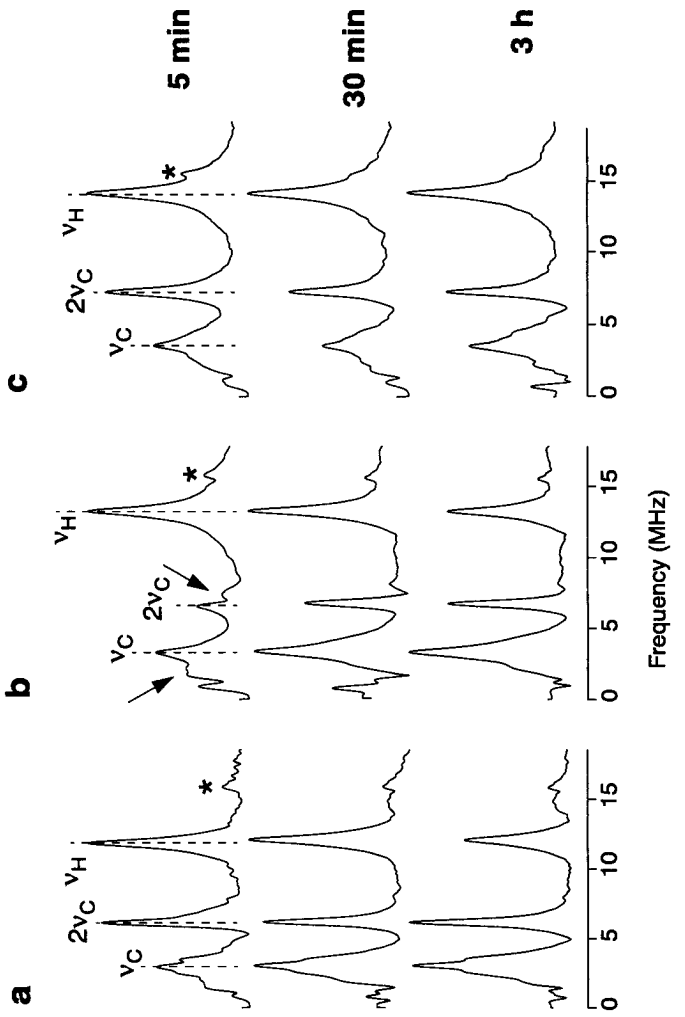

Fig. 6-10 Two-pulse ESEEM spectra of samples obtained from a $^{13}CO_2$:$Ca^{12}CO_3$(*vat*) experiment taken after time intervals 5 min, 30 min and 3 hours, and measured at the at the field positions 280 mT (a), 312 mT(b), and 336 mT(c). The nuclear Zeeman frequency ν_C of carbon and ν_H of protons as well as the sum combination frequencies $2\nu_C$ are marked by dashed lines for each time series. Mw frequency ν_{mw} = 9.705 GHz, temperature T = 16 K. The features marked with arrows are discussed in the text. The asterisks indicate spectrometer artifacts.

Figure 6-7 (inset). The spectrum at $g_\perp$ consists of one broad peak, shifted by approximately 0.08 MHz from the anti-diagonal ($\nu_1 = -\nu_2 + 2\nu_C$). At $g_\parallel$ the peak is narrower and

Table 6-2 Hyperfine coupling parameters of the ^{13}C nuclei for the different species, obtained from simulations of the HYSCORE spectra.

	a_{iso}^{C} (MHz ± 0.05)	T^{C}/g_e (MHz ± 0.05)	θ_I (± 5°)
Species (A)/(B)	0.2	0.5	75°
Species (C) (axial coord.)	0	0.3	20°
Species (C) (equat. coord.)	0.7	0.45	80°

the shift has decreased to ~ 0.06 MHz. No splitting of the two ridges expected for the $I = 1/2$ nucleus of ^{13}C is observed, indicating a small isotropic coupling. On the right hand side of Figure 6-11 simulations of the spectra are shown performed as described in

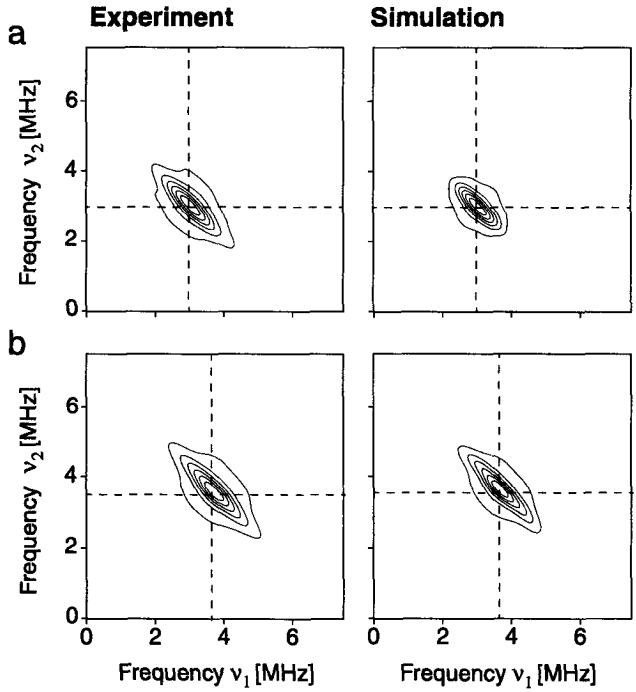

Fig. 6-11 Left side: experimental HYSCORE spectra of the sample taken after 2 hours in a $^{13}CO_2$:$Ca^{12}CO_3$(*vat*) experiment, recorded at the field positions 279 mT (a) and 336 mT (b) (field positions (a) and (c) in Figure 6-7) with τ values of 144 ns and 160 ns, respectively (ν_{mw} = 9.706 GHz, T = 16 K). The dashed lines indicate the proton Zeeman frequency. Right side: corresponding simulations, performed as described in the text with the coupling parameters given in Table 6-2.

the experimental section by using the parameters given in Table 6-2. For the $g_\perp$ simulation the contributions of three m_I^{Cu}-states are taken into account, including the extra-absorption peak at the high-field end of the EPR spectrum. In both simulation contributions from the ^{13}C matrix line are added. The HYSCORE spectra shown in Figure 6-11 are identical to those obtained from samples taken at earlier time intervals. From this observation we conclude that species *(A)* and *(B)* which give the main contributions to the EPR spectra of these samples exhibit very similar ^{13}C spectra.

In Figure 6-12 experimental HYSCORE spectra of the sample taken after 24 hours in a $^{13}CO_2$:$Ca^{12}CO_3$*(vat)* experiment are shown and compared to simulations performed with the parameters given in Table 6-2. The spectra were measured at the $g_\parallel$ and $g_\perp$ posi-

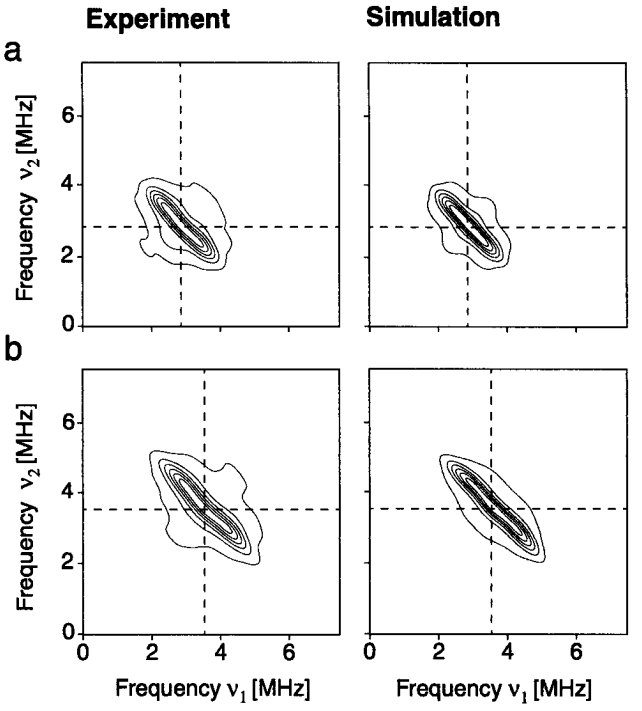

Fig. 6-12 Left side: experimental HYSCORE spectra of the sample taken after 24 hours in a $^{13}CO_2$:$Ca^{12}CO_3$*(vat)* experiment, recorded at the field positions 268 mT(a) and 330 mT (b) (field positions (a) and (c) in Figure 6-8) with a τ value of 160 ns (ν_{mw} = 9.706 GHz, T = 16 K). The dashed lines indicate the proton Zeeman frequency. Right side: corresponding simulations, performed as described in the text with the coupling parameters given in Table 6-2.

tions indicated by (a) and (c) in the echo-detected spectrum in Figure 6-8 (inset). Unlike in the ESEEM spectra strong signals are observed for both field positions. The experimental spectra consist of two overlapping, curved ridges, shifted from the nuclear Zeeman frequency by the dipolar coupling. The separation of the ridges indicates non-zero isotropic coupling and is larger at $g_\perp$ than at $g_\parallel$. The simulations of the spectra shown on the right side include contributions of equatorial and axial ^{13}C carbonate nuclei. The θ_I-values were estimated from geometrical models. Contributions from nuclei constituting the matrix line are not considered. Since pulse EPR spectra are measured at 16 K these spectra can be attributed to the low temperature modification of species *(C)*.

The presence of bidentate carbonate ligands in the early stages of the experiment, indicated by weak features in the two-pulse ESEEM spectra (arrows in Figure 6-10b, see discussion), is clearly demonstrated by the HYSCORE spectra shown in Figure 6-13, obtained from the sample taken immediately after the addition of the solution in a $^{13}CO_2$:$Ca^{12}CO_3$*(vat)* experiment. The three spectra were recorded at field positions close to $g_\parallel$ (285 mT(a)) and close to $g_\perp$ (327 mT (b) and 336 mT (c)). To emphasize the weak features from the strong ^{13}C coupling in measurements (b) and (c) the nuclear Zeeman frequencies were suppressed by an appropriate choice of the τ values. At the highest field (Figure 6-13c) the bidentate coupling manifests itself by two curved ridges at the outer ends of the central straight ridges. The separation of approximately 6 MHz is indicated by an arrow. At lower fields the ridges are detached from the main lines and the strong anisotropy is reflected in the triangular shape of the peaks (Figure 6-13b). Close to $g_\parallel$ the strong coupling case applies and the peaks are observed in the (-+) quadrant (Figure 6-13c) where the ridges are now parallel to the diagonal. They are separated by ~5.8 MHz and centered around ~4 MHz. The spectral features of the strongly coupled ^{13}C nuclei (bidentate coordination) are now completely separated from the contributions of the weakly coupled nuclei (monodentate coordination) in the (++) quadrant, unlike in the two-pulse ESEEM spectra in Figure 5-8 on page 83, where the spectra overlap.

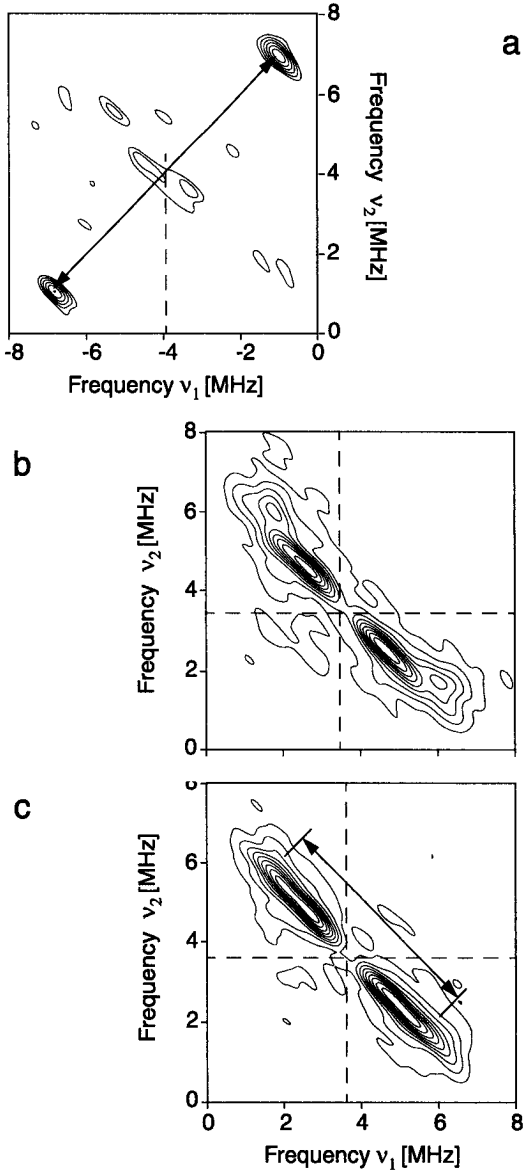

Fig. 6-13 HYSCORE spectra of the sample taken immediately in a $^{13}CO_2$:$Ca^{12}CO_3$(*vat*) experiment, recorded at the field positions 285 mT (a), 327 mT (b), 336 mT (c) with τ values of 248 ns (a) and 288 ns (b,c). In (b) and (c) the ^{13}C nuclear Zeeman frequencies, indicated by dashed lines, are suppressed by a blind spot (ν_{mw} = 9.701 GHz, T = 16 K).

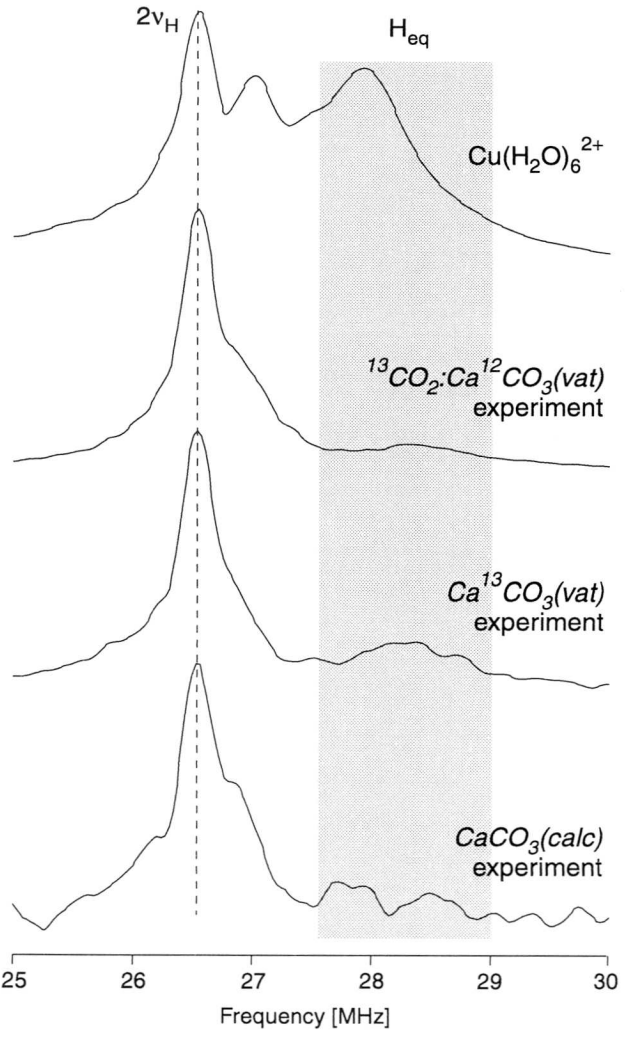

Fig. 6-14 Comparison of the four-pulse proton ESEEM spectra of the copper-hexaaquo complex, the copper vaterite samples obtained from $^{13}CO_2$:$Ca^{12}CO_3$(*vat*) and $Ca^{13}CO_3$(*vat*) experiments and the copper calcite sample from the $CaCO_3$(*calc*) experiment, taken immediately after the addition of the copper solution. The spectra were recorded at the magnetic field position 312 mT (ν_{mw} = 9.71 GHz, T = 16 K) and represent the sum of 30 signal traces, measured with τ values between 96 and 576 ns (16 ns steps). The dashed line indicates twice the proton Zeeman frequency $2\nu_H$. The shaded area marks the signals which can be assigned to protons of equatorial water or hydroxyl molecules.

6.3.5 1D Four-Pulse ESEEM of Protons.

In Figure 6-14 four-pulse sum combination frequency spectra are shown for *vaterite* and *calcite* samples from $^{13}CO_2$:$Ca^{12}CO_3$(*vat*), $Ca^{13}CO_3$(*vat*), and $CaCO_3$(*calc*) experiments, taken immediately after the mixing of the copper solutions and the solid calcium carbonate. The spectra can thus be assigned to species *(A)* and *(B)* at the mineral surface. They are compared to the sum combination spectrum of the copper-hexaaquo complex for the discussion of which we refer to section 5.3.4. The peak shifted by 1.5 MHz from twice the proton nuclear Larmor frequency in the copper hexaaquo spectrum has vanished for all copper surface complexes which exhibit very similar sum combination spectra in the three adsorption experiments. Instead of this peak a small hump shifted by approximately 1.8 MHz from $2\nu_H$ is observed. The intensity of the contributions from the axial water protons shifted by ~0.5 MHz from $2\nu_H$ is considerably reduced. The S/N ratio for the calcite sample is very poor due to the low copper concentration.

6.4 Discussion

The experimental results presented in the preceding section indicate that copper ions can interact with solid calcium carbonates in different ways. In the following these interactions are discussed and conclusions concerning the adsorption behavior of metal ions on calcium carbonates and the influence on the reactivity of the minerals are deduced. The results are further compared to the speciation calculations presented in section 4.3.

6.4.1 AAS Measurements

The AAS results indicate a high affinity of Cu^{2+} for the calcium carbonate surface under our experimental conditions. The rapid initial adsorption reaction is complete after five minutes and is followed by a slow removal of the remaining copper ions from solution. This two-step behavior has been observed for a number of transition metal ions. The slow step is explained by coprecipitation reactions [8,78,81]. We can conclude that most of the copper observed by EPR is associated with the carbonate mineral. Significant interactions between Cu^{2+} and the filter material are excluded based on EPR control measurements.

6.4.2 Structural Assignment of the Observed Copper Species

The various copper species observed in the CW and pulse EPR spectra can be related to different steps in the transformation of vaterite into calcite and/or the recrystallization of calcite in aqueous solution (cf. [66,67]). For a reliable interpretation of this dynamic effects it is, however, necessary to discuss the geometric and electronic structures of the individual species first.

Species *(A)* and *(B)*. The appearance of species *(A)* and *(B)* at the early stages of the adsorption experiment suggests that these species are associated with the vaterite or calcite surfaces. The clearly resolved EPR spectra are indicative for adsorption of monomeric Cu^{2+} species well distributed over the calcium carbonate surface rather than for the formation of polymeric hydroxyl or carbonate species. The presence of important amounts of free copper-carbonate species loosely bound to the mineral surface can be excluded based on the RT EPR spectrum in Figure 6-5 (see also section 6.4.3). Comparison of the spectral parameters in Table 6-1 with the results obtained for the copper-carbonate complexes in solution (Table 5-2 on page 77) allow us to give a first geometric interpretation. The g- and A-values found for the *(A)* species in Figure 6-2 formed immediately after addition of the copper solution to vaterite are close to the values found for the copper-carbonate complexes at pH 5.5. (cf. Table 5-2 on page 77). We thus conclude that this copper ions are coordinated in a monodentate fashion to one or several carbonate ions at the carbonate surface. Since a similar species *(A')* is also observed in the *$CaCO_3$(calc)* experiment both vaterite and calcite show the same initial behavior. The small differences between the EPR parameters of *(A)* and *(A')* are not unexpected since the different crystal structures of calcite and vaterite are expected to influence the geometry of coordination sites at the surface and to some extent also the structure of a thin surface layer [16]. The parameters of species *(B)* on the other hand deviate significantly from the values of the mono- and bidentate solution species. Spectra with similar parameters have been found for Cu^{2+} adsorbed on silica sols [121] and synthetic clay minerals [122]. They have been assigned to square-planar surface complexes with binding to four or two adjacent >SiOH or >AlOH surface sites, respectively. Clarke et al. [122] concluded that the binuclear coordination should occur at edges or 'defects' in the structure. Kucherov et al. [123] and Dedecek et al. [124] on the other hand proposed square-pyra-

midal structures for copper complexes in zeolite matrices, exhibiting the same EPR parameters. In analogy to these findings we assign the species *(B)* to a square-planar or square-pyramidal copper complex with coordination to several carbonate groups, possibly at kinks or steps of the vaterite crystals or the newly formed calcite nuclei. An octahedral coordination is difficult due to geometrical constraints at these sites.

If we compare the ^{13}C two-pulse ESEEM spectra shown in Figure 6-7 to the results obtained for the copper-carbonate complexes in solution (Figure 5-6 on page 80 and Figure 5-8 on page 83) the most striking differences are the peaks observed at the ^{13}C nuclear Zeeman frequency and the apparent missing of the features attributed to the bidentate coordination of the carbonate ligand[2]. The peak at ν_C indicates that the Cu^{2+} ions at the vaterite surface are surrounded by ^{13}C-labeled carbonate ions weakly coupled to the paramagnetic centers. This leads to a matrix signal similar to the one observed for the protons of the solvent water molecules. Carbonates with larger hyperfine couplings to the Cu^{2+} electron are revealed by the shoulders of the ^{13}C matrix peak at lower fields. These signals can be assigned to monodentate coordination of carbonate ligands in the equatorial plane (cf. section 5.4.3). The changes of the relative intensities of the carbon and proton peaks in Figure 6-7 can be explained if we assume a dipolar coupling matrix with its main axis pointing towards the Cu^{2+} ion (cf. Figure 5-14 on page 94). In the equatorial plane the distribution of the couplings leads to broad lines with fast decays of the time signals. The peaks observed at $g_\perp$ can thus be assigned mainly to matrix ^{13}C nuclei. Along $g_\parallel$ a single small coupling is expected resulting in small lines with intense contributions close to the matrix peak, as observed in Figure 6-7.

Numerical values for the ^{13}C couplings are obtained from the simulations of the HYSCORE spectra. As the simulations are based on the point-dipolar approximation the delocalization of the spin density to the ^{13}C nuclei must be small. No qualitative changes are observed for the ^{13}C spectra within the first three hours. The carbonate coordination to species *(A)* and *(B)* are therefore described by a single set of coupling parameters. From the dipolar coupling $T^C/g_e = 0.5$ MHz a Cu-C distance of 2.71 Å and a Cu-O distance of 1.9 Å is estimated, assuming a simple geometrical model with a C-O distance of

2. There *is* evidence for bidentate coordination in the spectra of the samples taken immediately after the addition of the copper solution. This observation is discussed together with the time evolution of the two-pulse ESEEM spectra (section 6.4.3).

1.3 Å and an angle (Cu-O-C) = 120° (sp^2 hybridization of the O atom). The value of 1.9 Å is typical for equatorial Cu-O bondlengths [24]. The isotropic coupling of 0.2 MHz is much smaller than the value of 1.2 MHz found for monodentate copper-carbonate complexes in solution (chapter 5). The proton spectra for species *(A)* and *(B)* indicate that the copper ion at the mineral surface is coordinated to four carbonate ligands in the equatorial plane (see below). We expect the steric hindrance to tilt the carbonate ions out of the equatorial copper plane, yielding poor in-plane and out-of-plane π bonding between metal and ligand orbitals. A tilt or a twist of the carbonate π system leads to a disturbed delocalization of spin density to the ^{13}C nuclei of the carbonate ions and is a plausible explanation for the small isotropic coupling. A more detailed discussion of the bonding mechanisms is given in chapter 5.

The proton lines observed in Figure 6-7 reveal that the number of water molecules in the first coordination sphere of the Cu^{2+} ions at the vaterite surface is considerably reduced. The proton matrix line is narrow and the signal arising from the equatorial water molecules is weak. A better resolution of the proton signals is however obtained in the four-pulse combination peak spectra in Figure 6-14. From these experiments it can be concluded that the dominant ligands in the equatorial plane of the surface complexes are carbonate ions both for vaterite and calcite and for different c_T. We assign the weak, broad lines shifted by 1.8 MHz from $2\nu_H$ to a small number of coordinated hydroxyl ions. The larger coupling of these protons as compared to the protons of the water molecules is in line with the high bonding covalency found for $Cu(OH)_4^{2-}$ complexes [125]. The spectra of the surface species can be compared to the results obtained for the copper-carbonate complexes in solution at pH 8 shown in Figure 5-10 on page 86. The elongation of the axial bond found for the solution species as a result of the carbonate coordination in the equatorial plane is not observed for the surface complexes. This points to weaker complexation of the carbonate ligands, reflected in the small a_{iso}^{C} value found for species *(A)* and *(B)*. The intensity of the axial proton line is considerably reduced but the coupling is not changed. As a square-planar or distorted square-pyramidal structure, obtained by the removal of one or two axial water ligands, is unlikely for species *(A)* based on the EPR parameters the intensity reduction of the axial proton line may be explained by an axial coordination to hydroxyl ligands. The presence of these ligands at the mineral surface is predicted by the speciation calculations (section 4.3.6).

The well defined EPR parameters as well as the absence of directly coordinated water/hydroxyl ligands in the equatorial plane indicate that the Cu^{2+} ions are bound in a structured layer of carbonate ions at the mineral surface formed by rapid initial dissolution of the vaterite in both types of experiments and/or the carbonate ions present in the copper solution in the $^{13}CO_2$:$Ca^{12}CO_3$(vat) experiment. Large ^{13}C couplings as found for bidentate coordination of the carbonate ligands are only observed at the initial stage of the experiments. From their weak intensity it can be concluded that the coordination of the Cu^{2+} ions both to the surface and to the other carbonates in the surface layer is predominantly monodentate. For this conclusion especially the results of the $Ca^{13}CO_3$(vat) experiment are important as a bidentate coordination to the vaterite surface cannot be excluded from a $^{13}CO_2$:$Ca^{12}CO_3$(vat) experiment where the carbonate lattice is unlabeled. Although no ^{13}C data are available for the $CaCO_3$(calc) experiment we estimate, based on the similarity of the EPR and proton spectra, that the calcite surface species show the same carbonate complexation than the one on vaterite.

The HYSCORE spectra in Figure 6-13 showing the bidentate copper-carbonate complexation confirm the EPR parameters obtained for the bidentate coupling from the simulation of the two-pulse ESEEM spectra in chapter 5. Simulation of the corresponding HYSCORE spectra is not possible with our program as the ^{13}C coupling is strongly orthorhombic. The orthorhombicity of the coupling is reflected in the shape of the HYSCORE ridges. Close to $g_{\|}$ the largest component of the coupling matrix shifts the spectrum into the (-+) quadrant where the peaks are expected to be separated by $2\nu_C = 6$ MHz and centered at $A^C/2 \sim 4.5$ MHz, based on the two-pulse ESEEM data (Table 5-3 on page 84). Experimentally we find a splitting of ~ 5.9 MHz and a $A^C/2$ value of ~ 4 MHz.

Species (C). The isotropic EPR spectrum *(C)* found after 24 hours at 130 K was already observed by Nassrallah-Aboukaïs et al. in their studies of the vaterite-calcite transformation [66,67]. They concluded that this signal arised either from small clusters of copper ions trapped in the bulk of the solid with strong dipolar coupling between the paramagnetic species or from structure-bound Cu^{2+} ions with inverted g-values ($g_{\|} < g_{\perp}$). Both interpretations have to be revised as can be inferred from the spectra shown in Figure 6-3. Lowering the temperature leads to the development of a very neat copper spectrum with an unusually high $g_{\|}$ value and a small $A_{\|}^{Cu}$ value, typical for copper com-

plexes in an octahedral environment with trigonal distortion [126]. The 20 K spectrum was observed by Rivaro et al. in their study of the interaction between trace metals and biogenic carbonates (marine mussel shells) and assigned to Cu^{2+} incorporated into the carbonate [127]. The crystal field of a Cu^{2+} ion substituted for a Ca^{2+} ion in the calcite lattice has nearly octahedral symmetry (cf section 4.2.1) which leaves the two e_g orbitals degenerate. This degeneracy is not removed by the small trigonal distortion along the *c*-axis. Only coupling to lattice vibrations leading to tetragonal or rhombic distortions of the crystal field can remove the degeneracy (Jahn-Teller distortion [20]). For a small resulting deformation of the complex, the distortion axis may jump between the three equivalent octahedral axes (Figure 4-1 on page 51) at higher temperatures yielding an isotropic signal with $g_{iso} = (g_{\parallel} + 2g_{\perp})/3$ for sufficiently rapid interconversion. Coffman [128] forwarded the tunneling among equivalent distorted Jahn-Teller configurations as another explanation for the appearance of an isotropic spectrum for Cu^{2+} in MgO above 50 K. At 1.2 K a highly anisotropic behavior is observed for this system.

It is obvious that the behavior of the spectra in Figure 6-3 can be explained by interconversion between equivalent Jahn-Teller configurations, either by hopping of the distortion axis or by tunneling. The $g_{iso} = 2.247$ value found for the isotropic species above 100 K is equal to the value calculated from the $g_{\parallel}$ and $g_{\perp}$ parameters of the low temperature spectrum. Species *(C)* can thus be unambiguously assigned to Cu^{2+} ions incorporated in the calcite lattice during the vaterite calcite transformation or by recrystallization of calcite, forming a dilute solid solution, since the very narrow lines exclude significant dipolar broadening.

This assignment is further supported by the two-pulse ESEEM and HYSCORE spectra of species *(C)* which show only ^{13}C signals. The electron spins of Cu^{2+} ions in the mineral lattice can not interact with the protons in solution. The ^{13}C spectra are better resolved than those of the surface species and can be explained by a mainly dipolar coupling matrix in the equatorial plane, in analogy to the analysis given for species *(A)* and *(B)*. The intensity of the ^{13}C matrix line is reduced due to the isotopic dilution in the newly formed calcite[3]. For a correct interpretation we must, however, keep in mind that for the copper ions in the calcite lattice we expect ^{13}C couplings both to carbonate

3. The ^{12}C:^{13}C ratio in the $^{13}CO_2$:$Ca^{12}CO_3$*(vat)* experiment for the whole system is approximately 5:1.

ligands in the equatorial plane and at the axial coordination positions. For the axial carbonate ions the largest splitting is expected along $g_{||}$ in the point-dipolar approximation so that the shoulders observed at $g_{||}$ can be explained by overlapping contributions from equatorial and axial ^{13}C carbonate nuclei.

This qualitative interpretation of the ^{13}C spectra of species *(C)* is confirmed by the HYSCORE simulations. The HYSCORE spectra obtained for the copper ions incorporated into the calcite lattice can only be reproduced if we include the contributions of both axial and equatorial carbonate ligands. The isotropic coupling of the axial ligand is assumed to be very small as the unpaired electron is expected to be localized in the metal $d_{x^2-y^2}$ orbital, based on the EPR data. The dipolar coupling of 0.3 MHz yields an axial Cu-O distance of ~2.3 Å, which is slightly smaller than the Ca-O distance of 2.38 Å observed in calcite (section 4.2.1). In the equatorial plane we find a value close to 2 Å for the Cu-O distance (from $r_{Cu\text{-}C} = 2.8$ Å) which corresponds to a reduction of 15% as compared to the Ca-O distance. The isotropic coupling is larger than the one found for the surface complexes but still smaller than the value obtained for the copper-carbonate complexes in solution.

From the observations of a single, clearly resolved EPR spectrum for species *(C)* at low temperatures it can be concluded that the coordination sphere of the Cu^{2+} ions substituted for Ca^{2+} ions in the calcite lattice is highly symmetric. The foreign ions are thus located at the centers of the Ca^{2+} coordination octahedra. The geometric data obtained from the ^{13}C spectra at 16 K indicate further that the small Cu^{2+} ion considerably distorts the crystal lattice in its vicinity due to the Jahn-Teller effect. At high temperatures the hopping of the distortion axis probably leads to lattice vibrations close to the Cu^{2+} ion.

Species *(D)*. EPR parameters for the weak signals of species *(D)* can only be determined in the low-field region due to the strong overlapping EPR spectra from species *(A)* and *(B)*. The parameters listed in Table 6-1 are very similar to those found for the low-temperature spectrum of species *(C)*. Species *(D)* shows, however, a static Jahn-Teller distortion already at 130 K which means that the distortion axis of the complex is fixed, possibly due to the coordination of one or two weaker ligands at the axial positions. Two explanations are possible for this behavior. (1) Either the signal arises from copper ions incorporated into defect lattice sites where one or two carbonate ligands are missing. (2)

Or the copper ion is on the point of being incorporated into the calcite lattice which means that it is located at a kink growth site where three or four ligands are lattice carbonate ions.

The two-pulse ESEEM results allow to distinguish between these two possibilities. The spectrum recorded at the observer field 270 mT for the sample taken after two hours in the $^{13}CO_2$:$Ca^{12}CO_3$(vat) experiment, shown in Figure 6-9, is again very similar to the low-field ESEEM spectrum of the Cu^{2+} ions incorporated in the calcite lattice (species(*C*)). The complete missing of proton signals makes a coordination at a surface kink site improbable. Furthermore only one ^{13}C hyperfine splitting is observed at $g_{\|}$. We tentatively assign species *(D)* to a complex in the calcite lattice with one or two missing axial ligands.

6.4.3 Mechanistic Interpretation

In the preceding paragraphs we have related the CW and pulse EPR spectra to surface and bulk Cu^{2+} species associated with the solid calcium carbonate minerals. For the discussion of the mechanism which lead to the formation of the different species we go back to the first step of the adsorption experiment: the transition of the copper ions from solution to the mineral surface.

Species in solution. The AAS data showed that the adsorption is practically complete at the time the first sample is taken. For a $^{13}CO_2$:$Ca^{12}CO_3$(vat) experiment with the large c_T the speciation calculations in section 4.3 predict that the dominant copper species in solution prior to the addition to the carbonate mineral is $Cu(^{13}CO_3)_2^{2+}$ whereas in the $Ca^{13}CO_3$(vat) experiment $Cu(^{13}CO_3)^0$ is expected to form in solution at pH 8.5 upon addition of the copper to the vaterite suspension. In both cases the bidentate coordination of carbonate ligands is expected to give rise to a large ^{13}C coupling in the cancellation range. The EPR results show that the coordination of the Cu^{2+} ions to the carbonate ions at the mineral surface is predominantly monodentate. Remnants of the bidentate ^{13}C coupling are, however, observed in the initial stage of both vaterite adsorption experiments. The intensity of these features decreases rapidly. The large ^{13}C coupling can either be explained by adsorption of bidentate copper-carbonate species at the surface or by remaining solution species in equilibrium with the adsorbed copper complexes. We favor

the second explanation as it is supported by the AAS measurement which show a slow decrease of the copper concentration in solution after the initial rapid adsorption process. Furthermore, the bidentate coupling can be related to the tumbling copper complex observed in the room temperature EPR spectrum in Figure 6-5, although no copper hyperfine coupling is observed (cf section 5.4.2). The similarity of the room temperature and low temperature spectrum in Figure 6-5 also clearly demonstrates that in the present study freezing effects which led to equilibrium and pH shifts in the investigation of the copper-carbonate complexes in solution are not relevant as aggregation of solute is not possible in the $CaCO_3$-water suspension. We estimate that the tumbling species are present in pores of the vaterite spherulites.

Species *(A)* and *(B)*. Species *(A)* is the first complex to be formed immediately after the addition of the copper solution to the solid mineral and can be associated unambiguously with the vaterite or calcite surface. During the transformation of vaterite to calcite in aqueous solution ($^{13}CO_2$:$Ca^{12}CO_3$*(vat)* and $Ca^{13}CO_3$*(vat)* experiments) the more soluble vaterite dissolves and less soluble calcite crystals nucleate and grow as the solubility product for calcite is exceeded by the Ca^{2+} and CO_3^{2-} concentrations in solution. In the *$CaCO_3$(calc)* experiment calcite undergoes ripening, a process during which large crystals grow at the expense of smaller ones [2]. The increase in amount of species *(B)* at the expense of species *(A)* revealed by the EPR spectra during the first few hours of the *vaterite* experiments can be explained either by the formation of species *(B)* at the surface of the newly precipitated calcite or by a transformation from *(A)* to *(B)* at the vaterite surface. An unambiguous distinction between the different processes which may also take place simultaneously is not possible with our data. It is well known that Cu^{2+} inhibits calcite growth and dissolution [80]. A probable explanation for the increase of species *(B)* is then the accumulation at steps and kinks of the dissolving vaterite crystals where dissolution is blocked due to the different structure of the square-planar copper complexes and/or a formation at similar structures of the calcite surface where the square-planar or square-pyramidal complexes inhibit crystal growth. Species *(B)* is not observed in the *$CaCO_3$(calc)* experiment probably due to the small copper concentration. We found that also in experiments with vaterite the formation of *(B)* depends on the ratio copper concentration vs. amount of solid calcium carbonate. If the number of growth and dissolution sites at the mineral surface largely exceeds the number of Cu^{2+} ions capable

of blocking the growth sites the dissolution and precipitation proceeds rapidly and the copper ions are buried in the crystal lattice before large amounts of *(B)* can accumulate. The transformation or recrystallization is then also expected to take place more rapidly which is in line with our experimental observations. A delay of the vaterite-calcite transformation with increasing copper concentrations was observed by Nassrallah-Aboukaïs et al. [66,67].

Information about ligand exchange processes in the first coordination sphere of the Cu^{2+} ions during the formation of species *(A)* from solution copper complexes is obtained from the ^{13}C two-pulse ESEEM spectra. The bidentate carbonate rings are opened and the free equatorial coordination sites are occupied by carbonate ligands at the vaterite surface. Driving forces for this ring opening are possibly the chelate effect of several monodentate surface ions, the nucleophilic nature of the surface hydroxyl ions and the cumbersome geometry of the bidentate coordination. In experiments with low c_T in solution ($Ca^{13}CO_3(vat)$ and $CaCO_3(calc)$) the adsorption reaction also involves substitution of water ligands by surface carbonate groups.

In the $^{13}CO_2$:$Ca^{12}CO_3(vat)$ experiment the ^{13}C signal observed in the early stage of the experiment is weak (cf. Figure 6-10), especially in the $g_{||}$ region where we expect the larger influence of directly coordinated ^{13}C carbonate ligands on the spectra. This can only be explained by the presence of unlabeled carbonate ligands in the first coordination sphere of species *(A)* copper ions which have replaced the bidentate carbonate ligands upon adsorption from solution. The question whether in the $^{13}CO_2$:$Ca^{12}CO_3(vat)$ experiment the initial ^{13}C-labeled carbonate ligands of the solution complexes are completely substituted by unlabeled carbonate ions can not be answered unambiguously as a rapid exchange between labeled and unlabeled carbonates at the surface is expected to take place simultaneously with the adsorption reaction. The increase in intensity of the ^{13}C-peaks observed after 30 minutes indicates an exchange of the unlabeled carbonate ligands by ^{13}C-labeled ligands from a surrounding surface layer or out of solution. Such an exchange is not unexpected as the carbonate ions at the surface and the solution are mainly labeled species in this initial stage of the experiment prior to the dissolution of important amounts of the unlabeled vaterite. This assumption is supported by the ^{13}C spectra in the $g_{\perp}$ region which arise mainly from matrix carbonates and which do not

change considerably within the first three hours. In the $Ca^{13}CO_3(vat)$ experiment intense ^{13}C signals arising from monodentate carbonate complexation are observed from the beginning on as only labeled carbonate ligands are present in the system.

The following reaction step namely the shift from species *(A)* to species *(B)* is not reflected in the two-pulse ESEEM spectra except for a further increase in intensity of the ^{13}C spectra observed in the $g_{||}$ region, pointing to a continued ^{12}C - ^{13}C carbonate ligand exchange in a $^{13}CO_2{:}Ca^{12}CO_3(vat)$ experiment. The ^{13}C couplings for the two species, however, seem to be identical. The increase of the ^{13}C signal is a hint to the association of species *(B)* with newly formed calcite as in the early stages of the experiment calcite is expected to grow mainly on the excess of $^{13}CO_3^{2-}$ in solution.

Species *(C)* and *(D)*. Upon formation or recrystallization of the calcite the Cu^{2+} ions are detached from the dissolving carbonate mineral and incorporated into the calcite bulk which leads to the formation of species *(C)*. From the EPR spectra it can be inferred that species *(D)* is formed as an intermediate step in the vaterite-calcite transformation. The appearance of species *(D)* is related to structural disorder in the freshly precipitated calcite nuclei which disappears upon recrystallization of the mineral phase. The strain introduced into the lattice by these defect centers may be responsible for the accumulation of *(D)* during the first hours of the experiments in analogy to the blocking of growth and dissolution sites by species *(B)*. The ^{13}C pulse EPR spectra do not reveal other intermediate complexes in addition to *(D)* when going from the surface species *(A)* and *(B)* to the bulk species *(C)*.

6.4.4 Summary of the Experimental Results

In this paragraph the results of the preceding section are summarized. The mechanistic model for the adsorption process is compared to the predictions for the surface complexes given in section 4.3.6.

In the $^{13}CO_2{:}Ca^{12}CO_3(vat)$ experiment the dominant species in solution and at the vaterite surface at pH 9 as predicted by the speciation calculations are Ca^{2+}, HCO_3^-, $Cu(CO_3)_2^{2-}$, $>CaCO_3^-$ and $>CO_3^-$. This situation is illustrated in Figure 6-15a. Adsorption of $Cu(CO_3)_2^{2-}$ solution complexes into the surface layer leads to the formation of the species *(A)* with opening of the bidentate coordination and partial ligand exchange. The

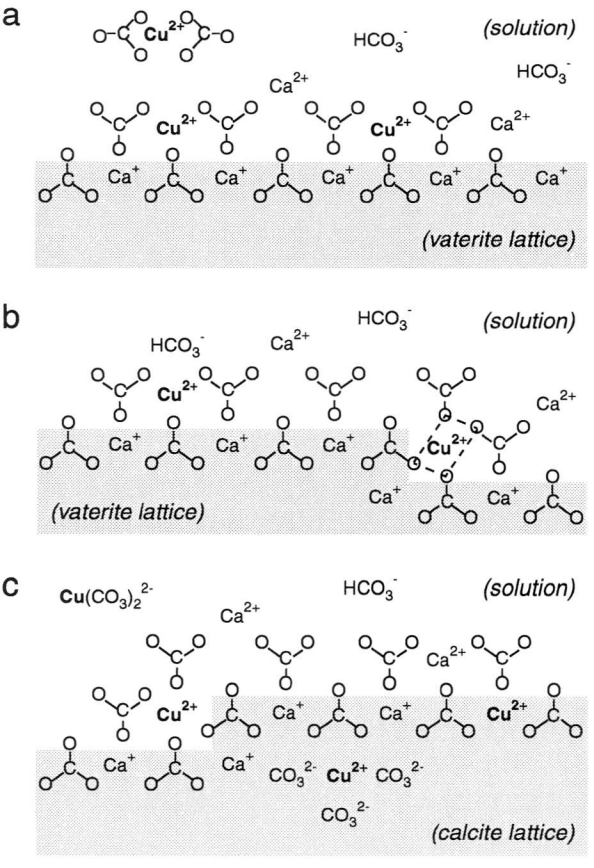

Fig. 6-15 Illustration of the interactions between Cu^{2+} and carbonate ions in solution and at the calcium carbonate surface for the different stages of the experiment. (a) Formation of the surface species *(A)* by adsorption of $Cu(CO_3)_2^{2-}$ complexes into the surface layer. (b) Dissolution of vaterite leads to the formation of square-planar species *(B)* at kink and step sites. (c) Nucleation and crystal growth of calcite with incorporation of Cu^{2+} into the crystal lattice. The formation of species *(B)* at the calcite surface is included in the drawing.

adsorption process is fast and leads to a nearly complete removal of the copper from solution. The ligand sphere of the isolated surface copper ions consists mainly of monodentate carbonate ions. The small isotropic ^{13}C coupling constants suggest weaker bonding of the surface carbonates as compared to the bonding in solution, probably due to sterical constraints in the equatorial complex plane. The shift from species *(A)* to *(B)* is

explained by an accumulation of the square-planar or square-pyramidal copper complexes at exposed surface sites where the dissolution of vaterite and the simultaneous precipitation of calcite is blocked (Figure 6-15b and c). As the vaterite-calcite transformation goes on the copper ions are incorporated as isolated species into the calcite lattice and a $Cu_xCa_{(1-x)}CO_3(s)$ solid solution is formed. The geometric distances calculated from the ^{13}C hyperfine parameters suggest that the Jahn-Teller elongated copper ions distort the calcite lattice locally. The results for the *$^{13}CO_2$:Ca$^{12}CO_3$(vat)* experiment are in good agreement with the predictions of the speciation calculations, except for the concentration of the copper surface complexes, calculated with the complexation constant given in Appendix C. This constant is derived from a single monodentate carbonate coordination in solution, an analogy which does obviously not apply to the present situation. In section 4.3.6 we have therefore derived a composite complexation constant for the surface complex that reflects the high coordination number and reproduces the experimental data more accurately.

In *Ca$^{13}CO_3$(vat)* and *$CaCO_3$(calc)* experiments the dominant species in solution at pH 8.5 are expected to be Ca^{2+}, HCO_3^- and $Cu(CO_3)^0$. At the surface there is a excess of $>CaOH_2^+$ and $>CO_3^-$ species, counterbalanced however by $>CaCO_3^-$ and $>CO_3Ca^+$. For these conditions we would expect at least one or two equatorial coordination sites of the copper ions to be occupied by water or hydroxyl ligands which is not the case. In this experiment the results are thus in bad agreement with the speciation calculations which are based on the assumption of an ordered, cystalline surface. The presence of protons in the second and third coordination spheres of the surface copper ions is, however, revealed by the strong $2\nu_H$ peak in the four-pulse ESEEM spectra in Figure 6-14.

Our results support thus the concept of a thin surface layer of carbonate and hydroxyl ions for the $CaCO_3$ surface into which the Cu^{2+} ions are strongly adsorbed [78,81] and where they are predominantly bound by carbonate ions. A one or two monolayers thick surface layer is expected to be structured to some extent by the mineral surface [16,83]. The uniformity of the metal binding sites explains the well defined EPR parameters of the two surface species *(A)* and *(B)*. However, one should not forget that pulse EPR probes only the close environment of the copper ions. The extrapolation from the copper coordination sphere to a surface layer is based on chemical considerations.

6.4.5 Application to other Metal Ions

In this study we have used Cu^{2+} as probe to investigate the interaction between transition metal ions and solid calcium carbonates. To derive general conclusions from our results we must estimate in how far the results are influenced by the specific properties of our probe. In section 4.2 we have already noted the influence of the ionic metal radii on the structures of the solid $MeCO_3(s)$ carbonates. Solid solutions $Me_xCa_{(1-x)}CO_3(s)$ with high miscibility between Me^{2+} and Ca^{2+} are formed if the differences in ionic radii between the two cations are small [64]. $CaCO_3$ and $CdCO_3$, e.g., show complete miscibility as the properties of the two crystal lattices are similar. The same is true to a lesser extent for Mn^{2+}. Other important factors in a general discussion are the affinities of the metal ions for carbonate ligands, reflected in the complexation constants for HCO_3^- and CO_3^{2-} [6]. Zachara et al. explained the reluctance of ions like Co^{2+}, Ni^{2+} and Zn^{2+} to an integration into the calcite lattice by the high hydration energies of the ions [81]. In Table 6-3 these values are summarized for a number of metal ions.

Table 6-3 Ionic radii, bicarbonate and carbonate complexation constants and hydration enthalpies for a selection of Me^{2+} ions.

Metal ion	r(pm)[a]	logK (HCO_3^-)[b]	logK (CO_3^{2-})[b]	ΔH (kJ/mol)[c]
Ca^{2+}	100	1.1	3.2	-1577
Mg^{2+}	72	1.0	3	-1921
Mn^{2+}	83	1.95	4.10	-1841
Fe^{2+}	78	2.17	4.73	-1946
Co^{2+}	74.5	2.2	4.41	-1996
Ni^{2+}	69	2.22	4.83	-2105
Cu^{2+}	73	2.2	6.73	-2100
Zn^{2+}	74	2.2	4.8	-2046
Cd^{2+}	95	2	4.35	-1807

a. given for high-spin configuration and 6-fold octahedral coordination [21,129].
b. taken from [5] and [60].
c. from [130].

Our results show that the Cu^{2+} ions are rapidly dehydrated at the calcium carbonate surface although the hydration energy is among the highest together with Zn^{2+} and Ni^{2+}. The equilibrium constant for monodentate copper-carbonate coordination, the dominant complexation form at the mineral surface, is in line with the values of the other metal ions. Bidentate carbonate coordination for which Cu^{2+} shows the highest affinity is not observed. Although the Cu^{2+} ion is small as compared to Ca^{2+}, the metal is integrated into the calcite lattice resulting in the formation of a solid-solution. A similar behavior is observed for other ions like Co^{2+} or Zn^{2+} which are only slightly larger than Cu^{2+} [83,85]. Differentiation between the cations based on the properties in Table 6-3 is thus difficult.

So far we have not included the electronic configurations and the coordination properties of the metal ions in the discussion. For Cu^{2+} we have concluded that the reluctance for the integration into the calcite lattice has mainly geometrical reasons. The small Jahn-Teller distorted Cu^{2+} ions fit badly into the larger coordination octahedra of Ca^{2+} resulting in a distortion of the lattice and the formation of square planar or square-pyramidal complexes at kinks and steps of the mineral surface. This leads to the inhibition of calcium carbonate crystal growth and dissolution. Based on the spectroscopic evidence for Cu^{2+} we suggest that the formation of complexes with coordination geometries other than regular octahedral is a key factor in the control of foreign ion integration into the calcite lattice. The adsorption into the thin surface layer can proceed to some extent via structural rearrangement of the surface ligands and is favored by the coordinative bonding to several surface carbonates. Complexation at kinks and step sites with well defined structural configurations [85] is, however, expected to be influenced considerably by the coordination properties and geometries of the cations.

For several metal ions in Table 6-3 distortions from perfect geometries in octahedral high-spin configurations in analogy to Cu^{2+} are observed and coordination numbers < 6 are common. Zn^{2+} often shows tetrahedral coordination in compounds where Cd^{2+} assumes a coordination number of six and Co^{2+} generally prefers tetrahedral complexes with monodentate anionic ligands, including OH^- [130]. Rosenberg et al. [131] correlated the instability of transition metal dolomites $CaMe^{2+}(CO_3)_2$ with $Me^{2+} = Fe^{2+}$, Co^{2+}, Ni^{2+}, Cu^{2+} or Zn^{2+} to a trigonal distortion of the MeO_6 octahedra (see also [64] for a

comparison of the MeO_6 octahedra dimensions). In many minerals distortion of the FeO_6 octahedra, e.g., is the rule rather than the exception and is also attributed to the Jahn-Teller effect [129].

We suggest that not the physico-chemical properties in Table 6-3 but mainly structural distortions are responsible for the observed reluctance of Co^{2+}, Ni^{2+} and Zn^{2+} to an incorporation into the calcite lattice as compared to Mn^{2+} and Cd^{2+} [81]. Zachara et al. concluded that, although strongly adsorbed on calcite (Zn^{2+} is absorbed more strongly than Mn^{2+}, e.g.), these ions persist on the calcite surface as hydrated complexes until they are incorporated into the calcite lattice upon recrystallization. Based on the strong adsorption of Co^{2+}, Ni^{2+} and Zn^{2+} on calcite we propose that the cations are also bound in a carbonate surface layer at the mineral surface and that their desorbability is not due to high hydration energies, but the formation of distorted complexes at kinks and steps. In his investigation of the influence of impurities on the growth rate of calcite Meyer [132] set up the following series for the inhibition efficiency of the other metal ions: $Fe^{2+} >> Zn^{2+} > Co^{2+} > Ni^{2+}$. Our results support the conclusion of Meyer who explained the strong inhibition by blocking of the growth sites (kinks) by the cations. For a number of metal ions, including Mn^{2+} which shows a high miscibility with Ca^{2+}, varying affinities for coordination sites at different crystal faces have been observed, leading to an unequal distribution of the metal ions in the resulting solid solution [77,85]. These step-specific preferences were explained by the different sizes and geometries of the surface sites. Reeder found, however, that for Zn^{2+}, e.g., additional factors like specific ion-site interactions have to be considered, which are 'poorly known at present' [85]. Our results suggest that specific coordination properties and geometries of the metal ions may account for these factors in the control of trace-metal incorporation into calcite.

The differences between Cu^{2+} and Ca^{2+} for the properties listed in Table 6-3, finally, are quite large which makes it difficult to discuss the precipitation and dissolution kinetics of solid calcium carbonate minerals, based on our results. The observation of highly coordinated copper-carbonate complexes at the calcite surface suggest however that Ca^{2+} ions may also be bound in a carbonate surface layer supporting the theory of $CaCO_3^0$ surface species as 'precipitation agents' at high pH.

6.5 Conclusions

In a detailed CW and pulse EPR analysis the interactions between the transition metal ion Cu^{2+} and the solid calcium carbonates vaterite and calcite have been investigated. During the transformation of vaterite to calcite and the recrystallization of calcite various copper-carbonate complexes are observed which can be assigned to different steps in the transformation process: a) strong adsorption to the mineral surface with formation of highly coordinated monodentate complexes in a thin, structured calcium carbonate surface layer; b) accumulation of square-planar or square-pyramidal complexes at exposed lattice sites of vaterite and the newly formed calcite due to inhibition of crystal dissolution and growth processes; c) incorporation into the calcite lattice where the copper ions exhibit a temperature-dependent dynamic Jahn-Teller effect. These assignments are based on EPR parameters and hyperfine couplings to neighboring ^{13}C (enriched) and proton nuclei from carbonate and water/hydroxyl ligands. No evidence was found for bidentate coordination to carbonate ligands at the surface. The smaller isotropic ^{13}C coupling constant observed for the surface complexes as compared to monodentate copper-carbonate solution complexes are explained by sterical constraints. Simulations of the ^{13}C HYSCORE spectra allow for a detailed structural characterization of the complexes. Our results show that adsorption of copper ions at calcium carbonate surface sites and incorporation of Cu^{2+} into the crystal leads to considerable distortions of the crystal lattice in the immediate environment of the foreign ion. We conclude that these distortions are responsible for the inhibition of calcium carbonate crystal growth and dissolution in the presence of Cu^{2+}. Similar mechanisms based on geometrical considerations should also apply to explain the inhibition effects observed for other transition metal ions like Fe^{2+}, Co^{2+}, Ni^{2+} and Zn^{2+}.

APPENDIX A *Basic Theoretical Concepts*

In this chapter some mathematical concepts commonly used for the description of spin systems in pulse EPR and NMR are introduced [32,133,134] and the theoretical background of the different simulation procedures for CW and pulse EPR spectra in chapters 5 and 6 is described.

A.1 Spin Hamiltonian

The complete Hamiltonian $\mathcal{H}$ of a molecular system including space and spin coordinates of electrons and nuclei can be very complex. The quantum-mechanical description of magnetic resonance is considerably simplified by the introduction of the spin Hamiltonian $\mathcal{H}_{sp}$, obtained by averaging of the full Hamiltonian over the lattice coordinates and over the spin coordinates of the paired electrons.

The spin Hamiltonian is expressed in linear (e.g. interaction of the electron spin with the static field $\boldsymbol{B}_0$) or bilinear terms (e.g. coupling between electron and nuclear spins) of spin angular momentum operators and contains a few phenomenological constants which can be related to the properties of the spin system (e.g. nuclear g_n factors). The finite dimension of the Hilbert space for an electron spin S coupled to n nuclear spins I_1, I_2, ..., I_n is given by

$$d_{HS} = (2S+1)\prod_{k=1}^{n}(2I_k+1) \tag{A.1}$$

The spin quantum number S reflects either the true electron spin for systems where

the contributions of orbital angular momentum to the ground state are small (e.g. organic radicals) or an effective spin of a subsystem with $2S+1$ states (e.g. ground state of rare earth ions with large spin-orbit coupling; cf. chapter 2).

A.2 Density Operator Formalism

In the density operator formalism the actual state of an ensemble of spins is characterized by a density operator σ. The properties of this density operator facilitate the description of spin dynamics in pulse EPR and NMR considerably [133].

The density operator σ is a hermitian operator and can be represented by a matrix of dimension $d_{HS} \times d_{HS}$. In the eigenbasis of $\mathcal{H}_{sp}$ the diagonal elements of σ are the populations of the corresponding eigenstate of $\mathcal{H}_{sp}$ whereas off-diagonal elements are coherent superpositions of eigenstates which can be related to the transverse magnetization $M_x \pm iM_y$ (single-quantum coherence). The time evolution of the system is given by the Liouville-von-Neumann equation

$$\frac{d\sigma}{dt} = -i[\mathcal{H}_{sp}, \sigma(t)] . \tag{A.2}$$

For a time-independent Hamiltonian (e.g. undisturbed spin system in the absence of MW pulses), integration of the Liouville-von-Neumann equation yields the solution

$$\sigma(t) = e^{-it\mathcal{H}_{sp}} \sigma(0)\, e^{it\mathcal{H}_{sp}} . \tag{A.3}$$

With this equation the evolution of the spin system under different Hamiltonians and for different time intervals t can be calculated in subsequent steps which is very convenient for the theoretical description of complex pulse experiments.

The expectation value of an arbitrary observable operator P is found by evaluating the trace of the product of the observable operator P with the density operator σ

$$\langle P \rangle = \mathrm{Tr}\{P\sigma(t)\} . \tag{A.4}$$

The description of pulse EPR experiments can be highly formalized by expressing

the density operator and the Hamiltonian by products of the cartesian spin operators S_x, S_y, S_z and the unit operator. In this formalism equilibrium magnetization is written as S_z, e.g., while the operators S_x or S_y contribute to the observable magnetization in the *xy*-plane.

A.3 Calculation of CW and Pulse EPR Spectra

From the spin Hamiltonian the energy level scheme and thus the EPR spectrum is obtained by determination of the eigenvalues and transition probabilities. Mathematically this can be performed either by analytical or numerical *diagonalization* of the Hamiltonian matrix or by application of *perturbation theory* [18,19].

Analytical diagonalization leading to results which can be handled is only possible for small spin systems like the $S = 1/2$ case or the $S = 1/2$, $I = 1/2$ system discussed above. Numerical diagonalization is always possible but may be tedious for large spin systems. In that case it is important to consider the relative energies of the terms involved in the spin Hamiltonian since considerable simplifications can be obtained by treating interactions separately if they differ by at least two orders of magnitude. In most cases the quantization axis of the electron spin is determined mainly by the large EZI or the zero-field splitting. In this case it is useful to diagonalize the Hamiltonian with respect to these terms and treat the remaining interactions as small perturbations. All simulations of CW EPR spectra in this thesis are based on second order perturbation formulae [95,120].

The simulation of pulse EPR spectra is based on the analytical formulae for two-, and four-pulse ESEEM experiments, given in Appendix B. These formulae have been derived using the density operator formalism outlined in the preceding section [30,36].

APPENDIX B *Analytical ESEEM Formulae*

In this appendix the analytical two-pulse, three-pulse and four-pulse ESEEM formulae for the electron spin echo intensity as a function of the different time intervals are given for an $S = 1/2$, $I = 1/2$ system. The definitions of the parameters are found in Chapter 2.

B.1 Two-Pulse ESEEM Formula

$$E(\tau) = 1 - \frac{k}{4}\,[2 - 2\cos(2\pi\nu_\alpha\tau) - 2\cos(2\pi\nu_\beta\tau) \qquad \text{(B.1)}$$

$$+ \cos(2\pi\nu_+\tau) + \cos(2\pi\nu_-\tau)]\,,$$

with the modulation depth parameter

$$k = 4\sin^2\eta\cos^2\eta = \left(\frac{\nu_I B}{\nu_\alpha\nu_\beta}\right)^2. \qquad \text{(B.2)}$$

From these formulae it can be seen that the modulation depth given by k is zero for $\eta = 0°$ and thus no ESEEM effect is observed for isotropic coupling. In anisotropic systems zero modulation is further obtained at the canonical orientations ($\theta = 0/90°$ for an axial coupling). This leads to a considerable distortion of the powder line shapes for θ values close to 0 or 90°. Maximum modulation depth with $k = 1$ is obtained for $\eta = 45°$ at exact cancellation.

B.2 Three-Pulse ESEEM Formula

$$E(t_1,\tau) = \frac{1}{2} - \frac{k}{8}\Big[[1-\cos(2\pi\nu_\alpha\tau)]\,[1-\cos(2\pi\nu_\beta[\tau+t_1])] \\ +[1-\cos(2\pi\nu_\beta\tau)]\,[1-\cos(2\pi\nu_\alpha[\tau+t_1])]\Big]. \tag{B.3}$$

The modulation depth parameter k is defined as in Eq. (B.2). In three-pulse ESEEM only fundamental frequencies are observed. Due to the amplitude factors $[1-\cos(2\pi\nu_\alpha\tau)]$ and $[1-\cos(2\pi\nu_\beta\tau)]$ blind spots are observed for $\tau = \frac{n}{\nu_{\alpha/\beta}}$ with $n = 0, 1, 2,...$

B.3 Four-Pulse ESEEM Formula

$$E(\tau,t_1,t_2) = 1 - \frac{k}{4}\,(E_I + E_{IIa} + E_{IIb} + E_{IIIa} + E_{IIIb}), \tag{B.4}$$

with the contributions from five different coherence transfer pathways given by

$$E_I = C_0(\tau) = 3 - \cos(2\pi\nu_\alpha\tau) - \cos(2\pi\nu_\beta\tau) \\ -\sin^2\eta\cos(2\pi\nu_+\tau) - \cos^2\eta\cos(2\pi\nu_-\tau),$$

$$E_{IIa} = C_\alpha(\tau)\cos[2\pi\nu_\alpha(t_2+\tau/2)] + C_\beta(\tau)\cos[2\pi\nu_\beta(t_2+\tau/2)],$$

$$E_{IIb} = C_\alpha(\tau)\cos[2\pi\nu_\alpha(t_1+\tau/2)] + C_\beta(\tau)\cos[2\pi\nu_\beta(t_1+\tau/2)],$$

$$E_{IIIa} = C_c(\tau)\cos^2\eta(\cos[2\pi(\nu_\alpha t_1 + \nu_\beta t_2 + \nu_+\tau/2)] \\ +\cos[2\pi(\nu_\beta t_1 + \nu_\alpha t_2 + \nu_+\tau/2)]),$$

$$E_{IIIb} = -C_c(\tau)\sin^2\eta(\cos[2\pi(\nu_\alpha t_1 - \nu_\beta t_2 + \nu_-\tau/2)]$$

$$+\cos[2\pi(\nu_\beta t_1 - \nu_\alpha t_2 - \nu_+\tau/2)]),$$

with the coefficients

$$C_\alpha(\tau) = \cos^2\eta\ \cos\left[2\pi\left(\nu_\beta\tau - \frac{\nu_\alpha\tau}{2}\right)\right] \tag{B.5}$$

$$+\sin^2\eta\cos\left[2\pi\left(\nu_\beta\tau + \frac{\nu_\alpha\tau}{2}\right)\right] - \cos\left[2\pi\left(\frac{\nu_\alpha\tau}{2}\right)\right],$$

$$C_\beta(\tau) = \cos^2\eta\ \cos\left[2\pi\left(\nu_\alpha\tau - \frac{\nu_\beta\tau}{2}\right)\right]$$

$$+\sin^2\eta\cos\left[2\pi\left(\nu_\alpha\tau + \frac{\nu_\beta\tau}{2}\right)\right] - \cos\left[2\pi\left(\frac{\nu_\beta\tau}{2}\right)\right],$$

$$C_c(\tau) = -2\ \sin\left[2\pi\left(\frac{\nu_\alpha\tau}{2}\right)\right]\ \sin\left[2\pi\left(\frac{\nu_\beta\tau}{2}\right)\right].$$

The general formula is simplified for the sum-peak experiment by setting $t_1 = t_2$. It is important to notice that in this formulae the angle η is defined as $0° \le \eta \le 90°$. As a consequence the labelling of the allowed and forbidden transitions changes when going from the weak to the strong coupling case with exact cancellation at $\eta = 45°$. With the convention given in chapter 2 the intensity of the allowed transition is always given by $\cos^2\eta$.

APPENDIX C *Equilibrium Calculations*

C.1 Equilibrium Constants

In Tables C1 and C2 of this appendix the complexation constants for the speciation calculations in aqueous solution presented in chapter 4 are given. The values are taken from Smith et al. [60] and Palmer et al. [13] and are tabulated for ionic strengths $I = 0$ M and $I = 1$ M and 25 °C. The K-values are numbered according to the index in the last column. For $I < 0.5$ M, the activities for a given ionic strength are calculated using the Davies formula [1].

The equilibria in solution are formulated as formation of species using the components Cu^{2+}, HCO_3^- or CO_3^{2-}, and H^+. The equations used to set up the EXCEL matrices for the program ChemEQL [25] in Appendix C.2 are written in bold. As an example we explicitly write down the formation constant K_3 of $H_2CO_3^{*(1)}$ which is obtained by combination of K_4 and K_5:

$$K_3 = \frac{[H_2CO_3^*]}{[CO_3^{2-}][H^+]^2} = \frac{[H_2CO_3^*]}{[HCO_3^-][H^+]} \cdot \frac{[HCO_3^-]}{[CO_3^{2-}][H^+]} = K_4 \cdot K_5 = 10^{16.68}$$

In Table C3 complexation constants for calcium complexes in solution as well as intrinsic complexation constants for surface equilibria are given for $I = 0$ M. The equilibria are formulated using the components $CaCO_3$(s), $>CaOH^0$, and $>CO_3H^0$ which represent the solid phase (vaterite) and the neutral surface complexes, respectively. The intrinsic complexation constants are taken from Van Cappellen et al. [6].

1. with $H_2CO_3^* = CO_2(aq) + H_2CO_3$, H_2CO_3 being the true carbonic acid with an acidity constant logK = 3.8. At 25 °C only 0.3% of the dissolved CO_2 is present as H_2CO_3.

		log K (at 25 °C)		*Index*
		I = 0 M	*I = 1 M*	

Table C1: *The CO_2/H_2O system.*

H_2O	$= OH^- + H^+$	-14	-13.79	*1*
$CO_2(g) + H_2O$	$= H_2CO_3^*$	-1.47	-1.53	*2*
$CO_3^{2-} + 2H^+$	$= H_2CO_3^*$	16.68	15.59	*3*
$HCO_3^- + H^+$	$= H_2CO_3^*$	6.35	6	*4*
$CO_3^{2-} + H^+$	$= HCO_3^-$	10.33	9.57	*5*

Table C2: *The $Cu^{2+}/CO_2/H_2O$ system.*

$Cu^{2+} + H_2O$	$= CuOH^+ + H^+$	-7.7	-8.2	*6*
$Cu^{2+} + 2H_2O$	$= Cu(OH)_2^0 + 2H^+$	-16.2	-15.2	*7*
$Cu^{2+} + 3H_2O$	$= Cu(OH)_3^- + 3H^+$	(-27.5)	-27.5	*8*
$Cu^{2+} + 4H_2O$	$= Cu(OH)_4^{2-} + 4H^+$	-39.6	-40.4	*9*
$2Cu^{2+} + 2H_2O$	$= Cu_2(OH)_2^{2+} + 2H^+$	-10.6	-11	*10*
$Cu^{2+} + CO_3^{2-} + H^+$	$= CuHCO_3^+$	12.13	10.57	*11*
$Cu^{2+} + HCO_3^-$	$= CuHCO_3^+$	1.8	1	*12*
$Cu^{2+} + CO_3^{2-}$	$= CuCO_3^0$	6.77	5.73	*13*
$Cu^{2+} + 2CO_3^{2-}$	$= Cu(CO_3)_2^{2-}$	10.2	9.32	*14*
$Cu^{2+} + 2H^+$	$= CuO(s) + H_2O$	-7.65	-	*15*
$2Cu^{2+} + CO_3^{2-} + 2H_2O$	$= Cu_2CO_3(OH)_2(s) + 2H^+$	5.8	-	*16*

Table C3: *The $CaCO_3(s)/Cu^{2+}/H_2O$ system.*

$CaCO_3(s)$	$= Ca^{2+} + CO_3^{2-}$	-7.9	-	17
$CaCO_3(s) + H_2O$	$= CaOH^+ + CO_3^{2-} + H^+$	-20.6	-	*18*
$Ca^{2+} + H_2O$	$= CaOH^+ + H^+$	-12.7	-	*19*
$CaCO_3(s) + H^+$	$= CaHCO_3^+$	3.53	-	*20*

		log K (at 25 °C)		*Index*
		I = 0 M	*I = 1 M*	
$Ca^{2+} + HCO_3^-$	$= CaHCO_3^+$	1.1	-	*21*
$CaCO_3(s)$	$= \mathbf{CaCO_3^0}$	-4.68	-	*22*
$Ca^{2+} + CO_3^{2-}$	$= CaCO_3^0$	3.22	-	*23*
$>CaOH^0$	$= \mathbf{>CaO^-} + H^+$	-17	-	*24*
$>CaOH^0 + H^+$	$= \mathbf{>CaOH_2^+}$	12.2	-	*25*
$>CaOH^0 + CO_3^{2-} + 2H^+$	$= \mathbf{>CaHCO_3^0} + H_2O$	24	-	*26*
$>CaOH^0 + CO_3^{2-} + H^+$	$= \mathbf{>CaCO_3^-} + H_2O$	16	-	*27*
$>CO_3H^0$	$= \mathbf{>CO_3^-} + H^+$	-4.9	-	*28*
$>CO_3H^0 + CaCO_3(s)$	$= \mathbf{>CO_3Ca^+} + CO_3^{2-} + H^+$	-10.7	-	*29*
$>CO_3H^0 + Cu^{2+}$	$= \mathbf{>CO_3Cu^+} + H^+$	-2	-	*30*

Table C3: *(continued)*

For the calcite system the complexation constants of equations *18, 20, 22* and *29* are replaced by $K_{18}^{calc} = -21.2$, $K_{20}^{calc} = 3$, $K_{22}^{calc} = -5.26$, and $K_{23}^{calc} = -11.3$, obtained with the solubility product of calcite $K_{17}^{calc} = -8.48$.

C.2 EXCEL Input Matrices for ChemEQL

In Tables C4 to C7 the EXCEL input matrices for the program ChemEQL are given. The corresponding calculations are shown in section 4.3.

Table C4: *The CO_2/H_2O system.*

	CO3--	H+	{logK}
	total	free	
H2CO3	1	2	16.68
HCO3-	1	1	10.33
CO3--	1	0	0
OH-	0	-1	-14
H+	0	1	0
	5.00E-02	1.00E-07	

Table C5: *The Cu^{2+}/H_2O system.*

	Cu++	H+	{logK}
	total	free	
Cu++	1	0	0
CuOH+	1	-1	-7.7
Cu(OH)20	1	-2	-16.2
Cu(OH)3-	1	-3	-27.5
Cu(OH)4--	1	-4	-39.6
Cu2(OH)2+	2	-2	-10.6
OH-	0	-1	-14
H+	0	1	0
	5.00E-04	1.00E-07	

Table C6: *The $Cu^{2+}/CO_2/H_2O$ system (I = 1M).*

	Cu++	CO3--	H+	{logK}
	total	total	free	
Cu++	1	0	0	0
CuOH+	1	0	-1	-8.2
Cu(OH)20	1	0	-2	-15.2
Cu(OH)3-	1	0	-3	-27.5
Cu(OH)4--	1	0	-4	-40.4
Cu2(OH)2++	2	0	-2	-11
CuHCO3+	1	1	1	10.57
CuCO30	1	1	0	5.73
Cu(CO3)2--	1	2	0	9.32
H2CO3	0	1	2	15.59
HCO3-	0	1	1	9.57
CO3--	0	1	0	0
OH-	0	0	-1	-13.79
H+	0	0	1	0
	5.00E-04	5.00E-02	1.00E-07	

Table C7: *The $CaCO_3(s)/Cu^{2+}/H_2O$ system.*

	sCO3H0	exp(-FY/RT)	sCaOH0	exp(-FY/RT)	CaCO3(s)	CO3--	Cu++	H+	[logK]
	adsorbent1	charge1.1	adsorbent2	charge2.1	solidPhase	total	total	free	
Cu++	0	0	0	0	0	0	1	0	0
CuOH+	0	0	0	0	0	0	1	-1	-7.7
Cu(OH)2O	0	0	0	0	0	0	1	-2	-16.2
Cu2(OH)2++	0	0	0	0	0	0	2	-2	-10.6
CuHCO3+	0	0	0	0	0	1	1	1	12.13
CuCO3O	0	0	0	0	0	1	1	0	6.77
Cu(CO3)2--	0	0	0	0	0	2	1	0	10.2
Ca++	0	0	0	0	0	1	-1	0	-7.9
CaOH+	0	0	0	0	0	1	-1	-1	-20.6
CaCO3O	0	0	0	0	0	1	0	0	-4.68
CaHCO3+	0	0	0	0	0	1	0	1	3.53
CO3--	0	0	0	0	0	0	1	0	0
HCO3-	0	0	0	0	0	0	1	1	10.33
H2CO3*	0	0	0	0	0	0	1	0	16.68
sCO3-	1	-1	0	0	0	0	0	0	-4.9
sCO3Ca+	1	1	0	0	0	1	-1	0	-10.7
sCO3Cu+	1	1	0	0	0	0	1	-1	-2
sCO3H0	1	0	0	0	0	0	0	0	0
sCaO-	0	0	1	-1	0	0	0	-1	-17
sCaOH0	0	0	1	0	0	0	0	0	0
sCaOH2+	0	0	1	1	0	0	0	1	12.2
sCaHCO3O	0	0	1	0	0	1	0	2	24
sCaCO3-	0	0	1	-1	0	1	0	1	16
OH-	0	0	0	0	0	0	0	-1	-14
H+	0	0	0	0	0	0	0	1	0
	0.00E+00	0	0.00E+00	0	1	5.00E-02	5.00E-05	1.00E-07	
ConstantCap									
30	30 {surface aera in m^2/g}								
2.50E-04	2.50E-04 {density of surface sites in mol/g}								
26	26 {conc. of solid in g/l}								
0.05	0.05 {ionic strength in M }								
37	37 {capacitance F/m^2}								

References

[1] W. Stumm, and J.J. Morgan, *Aquatic Chemistry (Third Edition)*, Wiley Interscience: New York, 1996.

[2] W. Stumm, *Chemistry of the Solid-Water Interface*, Wiley Interscience: New York, 1992.

[3] J.W. Morse and F.T. Mackenzie, *Geochemistry of Sedimentary Carbonates*, Elsevier: Amsterdam, 1990.

[4] E.A. Boyle, *Geochim. Cosmochim. Acta* **50**, 265 (1986).

[5] C. Fouillac and A. Criaud, *Geochem. J.* **18**, 297 (1984).

[6] P. Van Cappellen, L. Charlet, W. Stumm, and P. Wersin, *Geochim. Cosmochim. Acta* **57**, 3505 (1993).

[7] J.W. Morse, *Mar. Chem.* **20**, 91 (1986).

[8] M.B. McBride, *Soil Sci. Soc. Am. J.* **43**, 693 (1979).

[9] J. Bruno, P. Wersin, and W. Stumm, *Geochim. Cosmochim. Acta* **56**, 1149 (1992).

[10] M.L. Franklin and J.W. Morse, *Ocean Sci. Engn.* **7**, 147 (1982).

[11] A.B.P. Lever, *Studies in Physical and Theoretical Chemistry 33: Inorganic Electronic Spectroscopy (Second Edition)*, Elsevier: Amsterdam, 1984.

[12] K.V. Krishnamurty, G.M. Harris, and V.S. Sastri, *Chem. Rev.* **70**, 273 (1970).

[13] D.A. Palmer and R. van Eldik, *Chem. Rev.* **83**, 651 (1983).

[14] S.J. Hug, A. Johnson, G. Friedl, T. Lichtensteiger, H. Belevi, and M. Sturm, *Chimia* **51**, 884 (1997).

[15] S.L. Stipp, C.M. Eggleston, and B.S. Nielsen, *Geochim. Cosmochim. Acta* **58**, 3023 (1994).

[16] S.L. Stipp and M.F. Hochella Jr., *Geochim. Cosmochim. Acta* **55**, 1723 (1991).

[17] S.L. Stipp, M.F. Jr. Hochella, G.A. Parks, and J.O. Leckie, *Geochim. Cosmochim. Acta* **56**, 1941 (1992).

[18] A. Abragam and B. Bleaney, *Electron Paramagnetic Resonance of Transition Ions*, Clarendon Press: Oxford, 1970.

[19] J.R. Pilbrow, *Transition Ion Electron Paramagnetic Resonance,* Clarendon Press, Oxford, 1990.

[20] J.A. Weil, J.R. Bolton, and J.E. Wertz, *Electron Paramagnetic Resonance*, Wiley Interscience: New York, 1994.

[21] J.E. Huheey, E.A. Keiter, and R.L. Keiter, *Inorganic Chemistry (Fourth Edition)*, HarperCollins: New York, 1993.

[22] A.Z. Mason and K.D. Jenkins, In *Metal Speciation and Bioavailability in Aquatic Systems*, A. Tessier, D.R. Turner; Eds.; John Wiley & Sons: Chichester, 1995.

[23] E. Kiefer, L. Sigg, and P. Schosseler, *Environ. Sci Technol.* **31**, 759 (1997).

[24] A. F. Wells, *Structural Inorganic Chemistry (Fifth Edition)*, Clarendon Press: Oxford, 1984.

[25] B. Müller, *ChemEQL V2.0, A Program to Calculate Chemical Speciation Equilibria;* Internal Report, Limnological Research Center, EAWAG, 1996.

[26] P.W. Schindler and W. Stumm, In *Aquatic Surface Chemistry*; W. Stumm; Ed.; Wiley Interscience: New York, 1987.

[27] R. Kirmse and J. Stach, *ESR-Spektroskopie, Anwendungen in der Chemie*, Akademie-Verlag: Berlin, 1985.

[28] G. Krishnamoorthy and B.S. Prabhananda, *J. Magn. Res.* **30**, 273 (1978).

[29] R.G. Larsen, C.J. Halkides, and D.J. Singel, *J. Chem Phys.* **98**, 6704 (1993).

[30] W.B. Mims, *Phys. Rev. B* **5**, 2409 (1972).

[31] A. Schweiger, In *Modern Pulsed and Continuous Wave Electron Spin Resonance*; Kevan, L.; Bowman, M. K.; Eds.; Wiley Interscience: New York, 1990.

[32] G. Jeschke, 'New Concepts in Solid-State Pulse Electron Spin Resonance', *Ph.D. Thesis ETH Zürich* **No. 11873** (1996).

[33] M. Willer, 'Low-Frequency Pulse Electron Spin Resonance Spectroscopy', *Ph.D. Thesis ETH Zürich* **No. 12201** (1997).

[34] A. Lai, H.L. Flanagan, and D.J. Singel, *J. Chem. Phys.* **89**, 7161 (1988).

[35] E.J. Reijerse and S.A. Dikanov, *J. Chem. Phys.* **95**, 836 (1991).

[36] C. Gemperle, 'Neue Elektronenspinecho-Experimente', *Ph.D. Thesis ETH Zürich* **No. 9192** (1990).

[37] A.M. Tyryshkin, S.A. Dikanov, and D. Goldfarb, *J. Magn. Reson. A* **105**, 271 (1993).

[38] H.-I. Lee and J. McCracken, *J. Phys. Chem.* **98**, 12861 (1994).

[39] L.G. Rowan, E.L. Hahn, and W.B. Mims, *Phys. Rev.* **137**, A61 (1965).

[40] V. Kofman, J.J Shane, S.A. Dikanov, M.K. Bowman, J. Libman, A. Shanzer, and D. Goldfarb, *J. Am. Chem. Soc.* **117**, 12771 (1995).

[41] G.C. Hurst, T.A. Henderson, and R.W. Kreilick, *J. Am. Chem. Soc.* **107**, 7294 (1985).

[42] A. Pöppl and L. Kevan, *J. Phys. Chem.* **100**, 3387 (1996).

[43] J. R. Poole, *Electron Spin Resonance, a Comprehensive Treatment of Experimental Techniques,* Clarendon Press: Oxford, 1990.

[44] A. Schweiger, *Angew. Chem., Int. Ed. Engl.* **30**, 265 (1991).

[45] S.A. Dikanov, and Y.D. Tsvetkov, *Electron Spin Echo Envelope Modulation (ESEEM) Spectroscopy,* CRC Press: Boca Raton, Florida, 1992.

[46] P.M. Schosseler, Th. Wacker, and A. Schweiger, *Chem. Phys. Lett.* **224**, 319 (1994).

[47] C. Gemperle, G. Aebli, A. Schweiger, and R.R. Ernst, *J. Magn. Reson.* **88**, 241 (1990).

[48] A. Ponti and A. Schweiger, *J. Chem. Phys.* **102**, 5207 (1995).

[49] P. Höfer, A. Grupp, H. Nebenführ, and M. Mehring, *Chem. Phys. Lett.* **132**, 279 (1986).

[50] J.J. Shane, P. Höfer, E.J. Reijerse, and E. de Boer, *J. Magn. Reson.* **99**, 596 (1992).

[51] E.J. Reijerse and S.A. Dikanov, *Pure & Appl. Chem.*. **64**, 789 (1992).

[52] S.A. Dikanov, L. Xun, A.B. Karpiel, A.M. Tyryshkin, and M.K. Bowman, *J. Am. Chem. Soc.* **118**, 8408 (1996).

[53] A.M. Tyryshkin, S.A. Dikanov, R.G. Evelo, and A.J. Hoff, *J. Chem. Phys.* **97**, 42 (1992).

[54] C. Gemperle and A. Schweiger, *Chem. Rev.* **91**, 1481 (1991).

[55] W.B. Mims, *Proc. Roy. Soc.* **283**, 452 (1965).

[56] E.R. Davies, *Phys. Lett.* **47A**, 1 (1974).

[57] G. Jeschke and A. Schweiger, *J. Chem. Phys.* **103**, 8329 (1995).

[58] P. Sharrock and M. Melnik, *Can. J. Chem.* **63**, 52 (1985).

[59] C.R. Piriz Mac-Coll, *Coordin. Chem. Rev.* **4**, 147 (1969).

[60] R.M. Smith and A.E. Martell, *Critical Stability constants 4-6*, Plenum Press: New York, 1976.

[61] N.N Greenwood and A. Earnshaw, *Chemistry of the Elements*, Pergamon Press: Oxford, 1984.

[62] D.L.G. Rowlands and R.K. Webster, *Nature Phys. Sci.* **229**, 158 (1971).

[63] D. Kralj, L. Brecevic, and J. Kontrec, *J. Crystal Growth* **177**, 248 (1997).

[64] R.J. Reeder, In *Carbonates: Mineralogy and Chemistry* (ed. R.J. Reeder); *Rev. Mineral.* **11**, 1 (1983).

[65] F. Lippmann, *Sedimentary Carbonate Minerals*, Springer-Verlag: Berlin, 1973.

[66] N. Nassrallah-Aboukaïs, A. Boughriet, J.C. Fischer, M. Wartel, H.R. Langelin, and A. Aboukaïs, *J. Chem. Soc., Faraday Trans.* **92**, 3211 (1996).

[67] N. Nassrallah-Aboukaïs, A. Boughriet, J. Laureyns, A. Aboukaïs, J.C. Fischer, H.R. Langelin, and M. Wartel, *Chem. Mater.* **10**, 238 (1998).

[68] L.N. Plummer, T.M.L. Wigley, and D.L. Parkhurst, *Am. J. Sci.* **278**, 179 (1978).

[69] W.P. Inskeep and P.R. Bloom, *Geochim. Cosmochim. Acta* **49**, 2165 (1985).

[70] L. Chou, R.M. Garrels, and R. Wollast, *Chem. Geol.* **78**, 269 (1989).

[71] C.A. Brown, R.G. Compton, and C.A. Narramore, *J. Colloid Interface Sci.* **160**, 372 (1993).

[72] P-P. Chiang and M.D. Donohue, *J. Colloid Interface Sci.* **122**, 230 (1988).

[73] T. Arakaki and A. Mucci, *Aquatic Geochemistry* **1**, 105 (1995).

[74] D. Kralj and L. Brecevic, *J. Crystal Growth* **104**, 793 (1990).

[75] D. Kralj, L. Brecevic, and A.E. Nielsen, *J. Crystal Growth* **143**, 269 (1994).

[76] P. M. Dove and M.F. Hochella Jr., *Geochim. Cosmochim. Acta* **57**, 705 (1993).

[77] J. Paquette and R.J. Reeder, *Geochim. Cosmochim. Acta* **59**, 735 (1995).

[78] J.A. Davis, C.C. Fuller, and A.D. Cook, *Geochim. Cosmochim. Acta* **51**, 1477 (1987).

[79] R.N.J. Comans and J.J. Middelburg, *Geochim. Cosmochim. Acta* **51**, 2587 (1987).

[80] R.G. Compton and K.L. Pritchard, *J. Chem. Soc., Faraday Trans.* **86**, 129 (1990).

[81] J.M. Zachara, C.E. Cowan, and C.T. Resch, *Geochim. Cosmochim. Acta* **55**, 1549 (1991).

[82] N.E. Pingitore, Jr., F.W. Lytle, B.M. Davies, M.P. Eastman, P.G. Eller, and E.M. Larson, *Geochim. Cosmochim. Acta* **56**, 1531 (1992).

[83] N. Xu, M.F. Hochella, Jr., G.E. Brown, Jr., and G.A. Parks, *Geochim. Cosmochim. Acta.* **60**, 2801 (1996).

[84] N.C. Sturchio, R.P. Chiarello, L. Cheng, P.F. Lyman, M.J. Bedzyk, Y. Qian, H. You, D. Yee, P. Geissbuhler, L.B. Sorensen, Y. Liang, and D.R. Baer, *Geochim. Cosmochim. Acta.* **61**, 251 (1997).

[85] R.J. Reeder, *Geochim. Cosmochim. Acta* **60**, 1543 (1996).

[86] P. Papadopoulos and D.L. Rowell, *J. Soil Sci.* **40**, 39 (1989).

[87] H.J. Meyer, *J. Crystal Growth* **66**, 639 (1984).

[88] J. Westall, In *Particulates in Water, Advances in Chemistry Series* **189**, M. C. Kavanaugh and J. O. Leckie; Eds.; ACS: Washington D.C., 1980.

[89] C.F. Baes and R.E. Mesmer, *The Hydrolysis of Cations*, Krieger: Malabar, Florida, 1986.

[90] B.J. Hathaway and A.A.G. Tomlinson, *Coordin. Chem. Rev.* **5**, 1 (1970).

[91] P.M. Schosseler, B. Wehrli, and A. Schweiger, *Inorg. Chem.* **36**, 4490 (1997).

[92] N.M. Atherton and A.J. Horsewill, *Mol. Phys.* **37**, 1349 (1979).

[93] R.T. Ross, *J. Chem. Phys.* **42**, 3919 (1965).

[94] T. Wacker, 'FID-detektiertes spektrales Lochbrennen in the Elektronen-Spin-Resonanz', *Ph.D. Thesis ETH Zürich* **No. 9913** (1992).

[95] COMPAR, software program ERS300, ZWG-Berlin, Adlershof (1986).

[96] C.P. Keijzers, E.J. Reijerse, P. Stam, M.F. Dumont, and M.C.M Gribnau, *J. Chem. Soc., Faraday Trans.* **83**, 3493 (1987).

[97] B. Roos, *Acta. Chem. Scand.* **20**, 1673 (1966).

[98] D. Kivelson and R. Neiman, *J. Chem. Phys.* **35**, 149 (1961).

[99] A.H. Maki and B.R. McGarvey, *J. Chem. Phys.* **29**, 31 (1958).

[100] R.S. Eachus and W.G. Mc Dugle, *Inorg. Chem.* **12**, 1561 (1973).

[101] B.J. Hathaway and D.E. Billing, *Coordin. Chem. Rev.* **5**, 143 (1970)

[102] R. Wilson and D. Kivelson, *J. Chem. Phys.* **44**, 154 (1966).

[103] P.W. Atkins and D. Kivelson, *J. Chem. Phys.* **44**, 169 (1966).

[104] R. Wilson and D. Kivelson, *J. Chem. Phys.* **44**, 4445 (1966).

[105] R.L. Harlow and S.H. Simonsen, *Acta Cristallog.* **B32**, 466 (1976).

[106] S.S. Eaton, J. Dubach, G.R. Eaton, G. Thurman, and D.R. Ambruso, *J. Biol. Chem.* **265**, 7138 (1990).

[107] L.K. White and R.L. Belford, *J. Am. Chem. Soc.* **98**, 4428 (1976).

[108] R. Kirmse, U. Abram, and R. Böttcher, *Chem. Phys. Lett.* **90**, 9 (1982).

[109] L. Kevan, In *Modern Pulsed and Continuous Wave Electron Spin Resonance*; L. Kevan and M.K. Bowman; Eds.; Wiley: New York, 1990.

[110] A.L. Soli and R.H. Byrne, *Limnol. Oceanogr.* **34**, 239 (1989).

[111] L.N. Plummer and E. Busenberg, *Geochim. Cosmochim. Acta* **46**, 1011 (1982).

[112] R. Basosi, *J. Phys. Chem.* **92**, 992 (1988).

[113] Y. Orii and M. Morita, *J. Biochem.* **81**, 163 (1977).

[114] L.Bercevic and A.E. Nielsen, *J. Crystal Growth* **98**, 504 (1989).

[115] S. Wachi S. and A.G. Jones, *Chem. Engn. Science* **46**, 3289 (1991).

[116] A. López-Macipe, J. Gómez-Morales, and R. Rodríguez-Clemente, *J. Crystal Growth* **166**, 1015 (1996).

[117] R.J. Davey and T. Hirai, *J. Crystal Growth* **171**, 318 (1997).

[118] J.L. Wray and F. Daniels, *J. Am. Chem. Soc.* **79**, 2031 (1957).

[119] H. Roques and A. Girou, *Water Research.* **8**, 907 (1974).

[120] G.A. Sierra, 'Two Dimensional Pulse Electron Spin Resonance Methods for Spectral Resolution Enhancement in Solids', *Ph.D. Thesis ETH Zürich* **No. 12241** (1997).

[121] H. Motschi, *Colloïds and Surfaces* **9**, 333 (1984).

[122] C.J. Clarke and M.B. McBride, *Clays and Clay Minerals* **32**, 300 (1984).

[123] A.V. Kucherov, A.A. Slinkin, D.A. Kondratev, T.N. Bondarenko, A.M. Rubinstein, and Kh.M. Minachev, *Zeolites* **5**, 320 (1985).

[124] J. Dedecek, Z. Soblík,Z. Tvaruzkova, D. Kaucky, and B. Wichterlova, *J. Phys. Chem.* **99**, 16327 (1995).

[125] M. F. Ottaviani and G. Martini, *J. Phys. Chem.* **84**, 2310 (1980).

[126] M.D. Joesten, R.C. Kock, T.W. Martin and J.H. Venable, *J. Am. Chem. Soc.* **93**, 1138 (1971).

[127] P. Rivaro, R. Frache, A. Mazzucotelli, F. Cariati, and A. Pozzi, *Analyst* **119**, 2485 (1994).

[128] R.E. Coffman, *J. Chem. Phys.* **48**, 609 (1968).

[129] R.G. Burns, *Mineralogical Applications of Crystal Field Theory (Second Edition)*, Cambridge University Press, 1993.

[130] F.A. Cotton, and G. Wilkinson, *Advanced Inorganic Chemistry (Fourth Edition)*, John Wiley & Sons: New York, 1995.

[131] P.E. Rosenberg and F.F. Foit Jr., *Geochim. Cosmochim. Acta* **43**, 951 (1979).

[132] H.J. Meyer, *J. Crystal Growth* **66**, 639 (1984).

[133] R.R. Ernst, G. Bodenhausen, and A. Wokaun, *Principles of Nuclear Magnetic Resonance in One or Two Dimensions,* Clarendon Press: Oxford, 1987.

[134] J.J. Shane and A. Schweiger, *Principles of Pulse Electron Paramagnetic Resonance,* to be published.

Symbols and Abbreviations

Symbols

$\mathbf{1}$	unity matrix
$\mathbf{A}$	hyperfine interaction matrix
A	secular part of the hyperfine coupling
A_i	principal axis element of the HFI matrix
A_{ij}	element of the HFI matrix in the laboratory frame
a_{iso}	isotropic hyperfine coupling constant
$A_{\parallel}$	hyperfine coupling constant parallel to the radius vector for an axial HFI matrix
$A_{\perp}$	hyperfine coupling constant perpendicular to the radius vector for an axial HFI matrix
B	pseudo-secular part of the hyperfine coupling
$\boldsymbol{B}_0$	static magnetic field vector
c_{T}	total carbonate concentration
Cu_{T}	total copper concentration
$\mathbf{D}$	fine structure/zero-field splitting tensor
$\mathbf{g}$	**g** interaction matrix
g_e	free electron g-value, 2.0023
g_n	nuclear g-factor
$g_{\perp}$	g-value in the xy-plane for an axial **g** matrix
$g_{\parallel}$	g-value along the z-axis for an axial **g** matrix
h	Planck constant, 6.6260755×10^{-34} Js
$\mathcal{H}$	Hamilton operator
$\boldsymbol{I}$	nuclear spin operator

I	nuclear spin quantum number
$I_{x,y,z}$	x,y,z-component of the nuclear spin operator
I_a	intensity of an allowed EPR transition
I_f	intensity of a forbidden EPR transition
k	modulation depth parameter
k_i	chemical reaction rate
K_i	chemical equilibrium constant
K_{so}	solubility product
$\mathbf{Q}$	quadrupole interaction tensor
$\boldsymbol{r}$	radius vector, connecting electron and nucleus
m_I	magnetic quantum number of the nuclear spin
m_S	magnetic quantum number of the electron spin
$\boldsymbol{M}$	macroscopic magnetization
$M_{x,y,z}$	magnetization in x,y,z-direction
$\boldsymbol{S}$	electron spin operator
S	electron spin quantum number
$S_{x,y,z}$	x,y,z-component of the electron spin operator
T	dipolar hyperfine coupling constant
T_1	longitudinal relaxation time
T_2	transverse relaxation time
T_M	phase memory time
t_p	pulse length
β_e	Bohr magneton, 9.2740154×10^{-24} JT^{-1}
β_n	nuclear magneton, 5.0507866×10^{-27} JT^{-1}
η	one half of the angle between the nuclear quantization axes in the two electron spin manifolds
θ	polar angle between $\boldsymbol{B}_0$ and the z-axis of the **g/A** matrix.
ν_I	nuclear Zeeman frequency
ν_{ij}	frequency of the transition $\langle i\vert \leftrightarrow \langle j\vert$
ν_{MW}	microwave frequency
σ	density operator of a spin system
τ_p, t_1, t_2	interpulse delays
Ω	resonance offset of the electron spins in the rotating frame

Abbreviations

1D	One-Dimensional
2D	Two-Dimensional
AAS	Atomic Absorption Spectroscopy
AFM	Atomic Force Microscopy
CF	Crystal-Field
CW	Continuous Wave
DEFENCE	Deadtime Free ESEEM by Nuclear Coherence-transfer Echoes
ENDOR	Electron Nuclear DOuble Resonance
EPR	Electron Paramagnetic Resonance
ESEEM	Electron Spin Echo Envelope Modulation
EZI	Electron Zeeman Interaction
FID	Free Induction Decay
FT	Fourier Transform
HFI	HyperFine Interaction
HYSCORE	HYperfine Sublevel Correlated ESEEM spectroscopy
IR	InfraRed
LEED	Low Energy Electron Diffraction
MW	MicroWave
NMR	Nuclear Magnetic Resonance
NQI	Nuclear Quadrupole Interaction
NZI	Nuclear Zeeman Interaction
PAS	Principal Axes System
RF	Radio Frequency
RT	Room Temperature
S-band	2-4 GHz
SEM	Scanning Electron Microscopy
SOC	Spin-Orbit Coupling
S/N	Signal-to-Noise ratio
TEM	Transmission Electron Microscopy
TM	Transition Metal
UV	UltraViolet
Vis	Visible
X-band	8-12 GHz
XAS	X-ray Absorption Spectroscopy
XPS	X-ray Photoelectron Spectroscopy
XSW	X-ray Standing Wave

Acknowledgement

This thesis could not have been written without the support and encouragement of many people. I would like to thank

- Prof. Dr. Arthur Schweiger and Prof. Dr. Bernhard Wehrli, who agreed to a joint project between physical and environmental chemistry and provided excellent research conditions. The friendly and open-minded atmosphere in their research groups allowed me to grow both on a scientific and a human level.

- Dr. Thomas Wacker, who supervised my first steps in the field of pulse EPR.

- my lab-mates, Dr. Gustavo Sierra and Dr. Michael Willer, for the warm-hearted working atmosphere and the numerous discussions about life, EPR and everything.

- Josef Granwehr, Dr. Gustavo Sierra, Dr. Beat H. Meier, Dr. Tilo Levante, Dr. Tobias Bremi, and Christoph Scheurer for their excellent computer system management.

- Jörg Forrer, whose vast experience allows him to solve any electronic problem and to keep up memories of the days when pulse EPR was still young.

- Joe Eisenegger, Willi Groth, René Gunzinger for the skillful design and building of the tiniest mechanical devices.

- Walter Lämmler, Christian Dinkel and Ruth Stierli for their advice and support in practical laboratory work.

- Erwin Pleisch, Andreas Hunkeler and Roland Schmidli for always providing the liquid

nitrogen and helium to keep my samples cool.

- Verena Baumann, Konrad Boss, Karl Burkhalter, Walter Jäggi, Doris Kaufmann, Bruno Lambillote, Dr. Erich Meister, Irene Müller, Marie-Therese Werder, Heinrich Willi for ensuring the excellent functioning of the LPC and supporting me in numerous ways.

- former and present members of the groups of Prof. Schweiger and Prof. Wehrli: Dr. Rainer Bachmann, Josef Granwehr, Dr. Michael Hubrich, Dr. Eric Hoffmann, Dr. Gunnar Jeschke, Lorenz Liesum, Dr. Alessandro Ponti, Dr. Rafail Rakhmatoulline, Axel Sammet, Dr. Jochen Sebbach, Dr. Matthias Schuler, Dr. Jaap Shane, Stefan Stoll, Dr. Sabine Van Doorslaer and Markus Bott, Dr. Gabriela Friedl, Dr. Martin Mengis, Dr. Regula Müller, Dr. Tobias Schaller, for their friendship, help and advice in all situations.

- PD Dr. Andreas Gehring, who taught me the art of social paper-writing and always reminded me of the fact that science should be fun.

- Dr. Peter Weidler for the XRD analysis and for sharing his vast geological knowledge.

- Dr. Beat Müller, the father of ChemEQl, for his competent proof-reading of chapter 4.

- Prof. Dr. R. Giovanoli for the fascinating REM and TEM images.

- Erwin Grieder for the AAS measurements.

- the Swiss National Science Foundation for their generous financial support.

Finally, I would like to thank my parents for their selfless support and affection during all these years.

Curriculum Vitae

Personal data

Name	Paul Michel Schosseler
Birth	April 3, 1969 in Ettelbrück, Luxembourg
Nationality	Luxembourg

Studies

1993 - 1998	Ph. D. studies in applied EPR spectroscopy at ETH Zürich under the supervision of Prof. Dr. A. Schweiger and Prof. Dr. B. Wehrli (EAWAG)
1992	Diploma thesis in physical chemistry in the research group of Prof. Dr. A. Schweiger
1988 - 1992	Studies of chemistry at ETH Zürich

Education

1981 - 1988	Lycée classique de Diekirch, Luxembourg
1975 - 1981	Primary school in Diekirch, Luxembourg